Davies, P. J., McKenzie, J. A., Palmer-Julson, A., et al., 1991
Proceedings of the Ocean Drilling Program, Initial Reports, Vol. 133

13. SITE 820[1]

Shipboard Scientific Party[2]

HOLE 820A

Date occupied: 12 September 1990

Date departed: 12 September 1990

Time on hole: 9 hr

Position: 16°38.221'S, 146°18.229'E

Bottom felt (rig floor; m, drill-pipe measurement): 289.3

Distance between rig floor and sea level (m): 11.32

Water depth (drill-pipe measurement from sea level, m): 278.0

Total depth (rig floor, m): 433.5

Penetration (m): 144.2

Number of cores (including cores with no recovery): 17

Total length of cored section (m): 144.3

Total core recovered (m): 146.1

Core recovery (%): 101.3

Oldest sediment recovered:
Depth (mbsf): 144.3
Nature: mixed sediment with clay and nannofossils
Age: Pleistocene

HOLE 820B

Date occupied: 12 September 1990

Date departed: 14 September 1990

Time on hole: 2 days, 7 hr, 40 min

Position: 16°38.219'S, 146°18.218'E

Bottom felt (rig floor; m, drill-pipe measurement): 290.3

Distance between rig floor and sea level (m): 11.32

Water depth (drill-pipe measurement from sea level, m): 279.0

Total depth (rig floor, m): 690.3

Penetration (m): 400.0

Number of cores (including cores with no recovery): 44

Total length of cored section (m): 400.0

Total core recovered (m): 324.9

Core recovery (%): 81.2

Oldest sediment recovered:
Depth (mbsf): 400.0
Nature: partially lithified packstone
Age: Pleistocene

Principal results: Site 820 is located in 278 m of water in Grafton Passage, on the upper continental slope east of Cairns. It is the central site in a transect of three holes aimed at defining the relationships between changes in sea level, sediment sequences, and seismic geometries, and in particular, the response of a slope sequence to rapid changes in global sea level. Hole 820A was APC/VPC cored to 144.3 mbsf with 101% recovery. Hole 820B was APC-cored to 160.2 mbsf and XCB-cored to 400 mbsf; recovery overall was 81.2%. The section to 400 mbsf is an expanded Pleistocene interval; nannofossil and planktonic data suggest that this section is fairly complete and has an age range at the bottom of the hole from 1.27 to 1.48 Ma. Nannofossil preservation is related to subtle lithologic changes and is good in the upper 100 mbsf, moderate-to-poor between 100 and 300 mbsf, and improves again below 300 mbsf. Preservation of planktonic foraminifers is related to lithologic variability. Benthic foraminifers suggest that sediments above 150 mbsf were deposited in an upper bathyal environment and that sediments below 150 mbsf were deposited in water depths that fluctuated between upper bathyal and outer neritic. The pattern of sedimentation rates at Site 820 is comparable to that at Site 819. High rates of 41.1 cm/k.y. typify the middle Pleistocene; more modest rates of 8.2 cm/k.y., the latest middle Pleistocene; rapid rates of 35 cm/k.y., the earliest late Pleistocene, and a return to modest rates of 10 to 11 cm/k.y. in the latest Pleistocene.

Drilling at Site 820 recovered interbedded greenish-gray to dark greenish-gray wackestone/mixed sediments and coarser greenish-gray bioclastic packstones, the lithologies that reflect the contribution of shelf marine and terrigenous components. Variations in lithology and grain size allowed us to identify three principal lithologic units, described as follows:

1. *Unit I:* depth, 0–150.7 mbsf; age, 0–1.27 Ma, Pleistocene. Generally finer-grained than the underlying sediments, Unit I consists of bioclastic, very fine-grained wackestones and mudstones interbedded with bioclastic packstones. Bioturbation is pervasive throughout the unit. Dolomite increases gradually with depth in this unit, which may be divided into two subunits: an upper clay-rich subunit and a lower, more carbonate-rich subunit.

(1) *Subunit IA:* depth, 0–64.3 mbsf; age, 0–465 k.y., Pleistocene. Here, dominant lithologies are thick beds of dark greenish-gray terrigenous clay and fine calcareous/clayey mixed sediments (<60% carbonate). Quartz and feldspar are common in the mixed sediments and in the dark terrigenous clays. Coarser-grained sediments include gray to dark greenish-gray, silty to medium sand-sized packstones with siliciclastic material. At two levels, 6.6 to 7.65 mbsf and 31.2 to 33.6 mbsf, very coarse beds of gray packstones and rudstones contain pebble-sized rhodoliths and bioclastic debris, including corals, coralline algae, mollusks, echinoid fragments, and abundant benthic and planktonic foraminifers.

(2) *Subunit IB:* depth, 64.3–150.7 mbsf; age, 0.275–1.27 Ma, Pleistocene. The subunit is carbonate-rich and consists of greenish-gray to dark greenish-gray clayey wackestones with nannofossils interbedded with bioclastic packstones and wackestones. Silt-sized quartz and feldspar accompany the fine-to-medium sand-sized packstone and wackestone beds. Between 122.4 and 127.85 mbsf, very coarse-grained *Halimeda,* bryozoan, and mollusk rudstones with a wackestone matrix can be seen.

2. *Unit II:* depth, 150.7–208.1 mbsf; age, 0.93–1.27 Ma, Pleistocene. This unit is composed of a mixture of bioclastic packstones, bioclastic clayey mixed sediments, and silty claystones and represents a transition from an even coarser Unit III below to the finer-grained sediments of Unit I. The base of the unit is marked by an upward-fining sequence, grading from medium-to-coarse bioclastic packstone to silty calcareous mixed sediment containing bioclasts. This, in turn, is overlain by a 7-m-thick section of dark gray claystone that contains silt-sized micrite, bioclasts, and quartz grains. The rest of the unit is composed of

---

[1] Davies, P. J., McKenzie, J. A., Palmer-Julson, A., et al., 1991. *Proc. ODP, Init. Repts.,* 133: College Station, TX (Ocean Drilling Program).

[2] Shipboard Scientific Party is as given in list of participants preceding the contents.

three upward-coarsening sequences: the lower two of which exhibit greenish-gray, clayey mixed sediments that grade upward into medium sand-sized, greenish-gray, nannofossil calcitic packstone. The uppermost unit consists of a thinner and finer, upward-coarsening sequence of bioturbated nannofossil mixed sediment containing quartz and micrite that exhibited a size gradation from silt to fine sand-sized grains.

3. *Unit III:* depth, 208.1–400 mbsf; age, 1.27–1.48 Ma, Pleistocene. The unit is dominated by bioclastic packstones with interbedded, sometimes laminated, finer-grained calcareous mudstones and mixed sediments. Five cycles were recognized in the unit, with each representing an upward-coarsening cycle from dark greenish-gray calcareous mudstone with bioclasts and nannofossils up to medium-to-fine calcareous chalky packstone containing quartz, feldspar, nannofossils, and clay. Dolomite (maximum = 17.4% at 224.4 mbsf) is present in the top three cycles of Unit III.

Downhole measurements were conducted in Hole 820B using the seismic stratigraphic, geochemical, and FMS combinations. Velocity, resistivity, and density strongly correlate throughout the logged interval as a result of porosity dominance in these logs. Changes in velocity and density suggest that mechanical compaction is dominant over diagenesis for controlling porosity at the site. Logged units closely correlate with those defined in the lithology. Between 69 and 150 mbsf in log Unit 1, a smooth compaction profile can be seen in the resistivity and velocity logs, whereas high resistivity and velocity between 120 and 130 mbsf correlate well with the coarser-grained *Halimeda* beds. Log Unit 2 (150–205 mbsf) defines three upward-coarsening sequences related to the distribution of clay and carbonate. In Log Unit 3, the geochemical, resistivity, velocity, and density logs clearly define five subunits, which are clay-rich at the base and carbonate-dominated at the top. These interpretations agree substantially with lithologic information.

The mineralogy of the Pleistocene sediments is dominantly carbonate and clay. Aragonite occurs throughout the section and represents 50% of the carbonate minerals at the top, decreasing to 40% at the base. High-Mg calcite (HMC) is present down to 170 mbsf, disappears between 170 and 265 mbsf, and reappears again below 265 mbsf. Dolomite occurs between 44.5 and 330.3 mbsf and varies from 0.8% to 17.4%, whereas low-Mg calcite (LMC) occurs in all samples, with concentrations varying from 18% to 60%. Quartz also is present in all samples and ranges from 4.9% to 26%.

Interstitial water chemistry is dominated by diagenetic reactions involving (1) dissolution of metastable aragonite and HMC, (2) precipitation of dolomite and LMC, (3) clay mineral alteration, and (4) oxidation of organic material. These processes are reflected in a strong depletion of calcium, magnesium, and sulfate with increasing bottom depth, accompanied by an increase in strontium and ammonia. As a result of the hard nature of the sediments, water samples obtained using the WSTP (water sampler, temperature, and pressure) tool were contaminated by annulus fluids.

Generally, organic carbon values at Site 820 were low, not exceeding 0.45%, and represent a mixture derived from both marine and terrigenous sources. The sediments contained high concentrations of methane, although the C_1:C_2 ratio varied from 13,000 to 700. The observed low sulfate concentrations and high methane and trace of ethane/propane above 190 mbsf suggest a bacterial origin for methane and ethane/propane production. However, below 190 m, methane and ethane/propane generation is more likely related to both thermogenic and biological processes at greater depths.

Paleomagnetic results from Site 820 must await shore-based studies. A large portion of the sediments from the Pleistocene cored sections were found to carry a remanence having a steeply dipping negative inclination. Many of the cores maintained this inclination after AF demagnetization of 15 mT, the maximum field allowable by ODP for demagnetization of the archive half of cores. Detailed AF demagnetization in peak fields greater than 15 mT and thermal treatment will be required to generate a clear magnetic polarity stratigraphy at this site.

BACKGROUND AND SCIENTIFIC OBJECTIVES

Site 820 is one of three sites in close proximity that were occupied in Grafton Passage. For a summary of the background and overall scientific objectives at these sites, the reader is referred to the "Background and Scientific Objectives" section of the "Site 819" chapter (this volume).

Site 820 is located in Grafton Passage on the outer edge of an upper-slope terrace in front of the Great Barrier Reef (see Fig. 1, "Introduction" chapter, and Fig. 2, "Site 819" chapter, this volume). Figure 2 from the "Site 819" chapter shows the location of site-survey seismic data, and Figure 3 in the "Site 819" chapter (this volume) exhibits a seismic section through the site, whereas Figure 1 is the pre-drilling prognosis for this site.

Our objectives for drilling at Site 820 were as follows:

1. To determine the age and facies of central portions of the aggradational and progradational units immediately in front of present-day Great Barrier Reef.
2. To determine the relationship between sea level and depositional facies to extract the sea-level signature.
3. To determine the timing and factors controlling the initiation of reef growth on central Great Barrier Reef.
4. To understand the factors controlling the transition from prograding to aggrading depositional geometries.

OPERATIONS

Transit to Site 820

The ship traveled 1.5 nmi in 1.32 hr at an average speed of 1.1 kt in dynamic positioning (DP) mode. A taut wire beacon was set on the bottom at 0900L (all times given in local time, or L), 12 September 1990.

Hole 820A

The position of Hole 820A is 16°38.221′S, 146°18.229′E; water depth was estimated (using the precision depth recorder, PDR) at 280.6 m from sea level. The bit was positioned at a water depth of 275.7 m, and the first core was shot at 0948L, 12 September. From Core 133-820A-1H, we recovered 7.18 m of sediment and placed the mud line at a water depth of 278.0 m from sea level. Continuous APC cores (Cores 133-820A-1H through -15H) were taken from 0 to 140.2 mbsf, with 140.2 m cored and 143.8 m recovered (102.5% recovery; excessive recovery results from gas expansion of the sediments).

Vibrapercussive (VPC) Cores 133-820A-16V through -17V were taken from 140.2 to 144.2 mbsf, with 4.1 m cored and 2.03 m recovered (49.5% recovery). The bottom hole assembly (BHA) was pulled out of the hole and cleared the seafloor at 1800L, 12 September.

Hole 820B

The *Resolution* moved 20 m west in DP mode, and Hole 820B was spudded at 16°38.219′S, 146°18.218′E at 1907L, 12 September. Based on drill-pipe measurements from Hole 820A, we estimated that the mud line occurred at a water depth of 279.0 m from sea level. However, the first core retrieved from Hole 820B was a water core. The bit was positioned at a water depth of 277.7 m, and Core 133-820B-1H was shot; we recovered 8.23 m of sediment. We determined that the mud line was located at a water depth of 279.0 m. Continuous APC cores (Cores 133-820B-1H through -17H) were taken from 0 to 160.2 mbsf, with 160.2 m cored and 161.4 m recovered (100.7% recovery).

Cores 133-820B-18X through -44X were taken from 160.2 to 400 mbsf, with 239.8 m cored and 163.5 m recovered (68.2% recovery). After a short pipe trip to 104.4 mbsf and back to the bottom with no drag or fill, we pulled the bit to 104.4 mbsf for logging. Logs were run as follows:

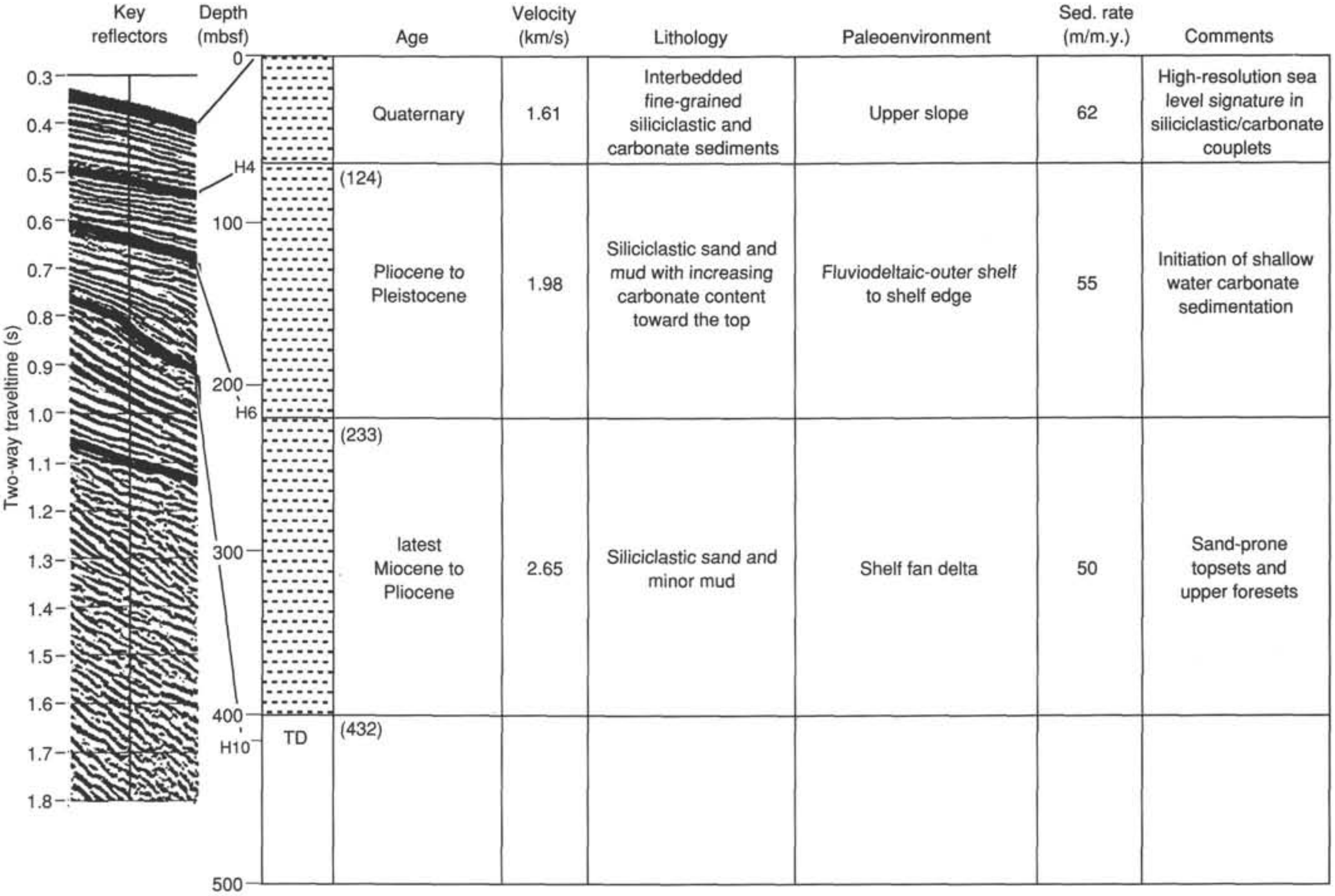

Age	Velocity (km/s)	Lithology	Paleoenvironment	Sed. rate (m/m.y.)	Comments
Quaternary	1.61	Interbedded fine-grained siliciclastic and carbonate sediments	Upper slope	62	High-resolution sea level signature in siliciclastic/carbonate couplets
(124) Pliocene to Pleistocene	1.98	Siliciclastic sand and mud with increasing carbonate content toward the top	Fluviodeltaic-outer shelf to shelf edge	55	Initiation of shallow water carbonate sedimentation
(233) latest Miocene to Pliocene	2.65	Siliciclastic sand and minor mud	Shelf fan delta	50	Sand-prone topsets and upper foresets
(432)					

Figure 1. Pre-drilling prognosis for Site 820.

1. The induction/density/sonic/caliper/gamma-ray (DITE/HLDT/SDT/MCDG/NGT) logging tool was run into the hole at 0900L, 14 September. We found the bottom 10.0 m above the total depth of the hole, and took the tool back out of the hole at 1030L, 14 September.

2. The geochemical/aluminium clay tool/gamma-ray/temperature (FMS/NGT/TCC) logging tool was run into the hole at 1205L; we found bottom 35.6 m above the total depth of the hole, and pulled the tool back out of the hole at 1615L, 14 September.

3. The formation microscanner/gamma-ray/temperature (FMS/NGT/TCC) logging tool was run into the hole at 1910L, when it reported 40.8 m of fill at the bottom of the hole.

4. A vertical seismic profile (VSP) was attempted. We ran the tool into the hole at 2035L for check shots, logged to 65.5 m off bottom, and pulled it back out of the hole at 2315L, 14 September.

Table 1 contains the coring summary for Site 820.

SITE GEOPHYSICS

A general description of the design and operation of the joint site-location survey for Sites 819, 820, and 821 is included in the "Site Geophysics" section, "Site 819" chapter (this volume).

Site 820

After we completed drilling Site 819A and the ship separated from the beacon at JD 254/2118UTC, 11 September 1990, *JOIDES Resolution* returned to its confirmed GPS position for Site 820 using dynamic positioning control. A taut-wire beacon was deployed at the site at JD 254/2241UTC; final coordinates of Hole 820A are 16°38.221′S and 146° 18.229′E, with a water depth of 278.0 m (drill-pipe measurement from sea level).

Site 820 is the middle site of three sites (Sites 819, 820, and 821) on an upper-slope terrace adjacent to Great Barrier Reef, about 3 km west of Site 819 and 2 km east of Site 821 (Figs. 2 and 3). The site lies about 8 km east of the nearest reef (Euston Reef) and was positioned so we could examine the foreset facies of deeper progradational units and the outer part of aggradational units, which form the upper slope in the area (Fig. 4).

Reasonable correspondence of major features at the site can be seen in the *JOIDES Resolution* single-channel seismic profiles and the *Rig Seismic* multichannel seismic profiles (Figs. 3 and 4), but detailed seismic characteristics of the site were difficult to resolve with the *Resolution* profile. Basement is not visible in any of the water-gun data across the site; however, normal resolution Gulf Aquapulse seismic data in the area (Symonds et al., 1983) indicate that it may lie up to 4 s TWT below the seafloor. The site is underlain by an upper 0.18 s TWT (~146 m) thick unit that consists of relatively flat-lying, subparallel reflectors. In *Rig Seismic* data, the reflectors have a higher amplitude in the upper part of the unit above a very irregular, disrupted reflector about 0.13 s TWT (~100 m) below the seafloor. In the *JOIDES Resolution* profile (Fig. 4), the whole unit appears as a zone of variable amplitude reflectors, all of which are distinctly lower in amplitude than those in underlying units. The

Table 1. Coring summary, Site 820.

Core no.	Date (Sept. 1990)	Time (UTC)	Depth (mbsf)	Length cored (m)	Length recovered (m)	Recovery (%)
Hole 820B						
1H	11	2350	0–7.2	7.2	7.18	99.7
2H	12	0000	7.2–16.7	9.5	9.54	100.0
3H	12	0010	16.7–26.2	9.5	9.74	102.0
4H	12	0030	26.2–35.7	9.5	9.66	101.0
5H	12	0050	35.7–45.2	9.5	9.89	104.0
6H	12	0105	45.2–54.7	9.5	9.98	105.0
7H	12	0115	54.7–64.2	9.5	9.54	100.0
8H	12	0135	64.2–73.7	9.5	9.98	105.0
9H	12	0200	73.7–83.2	9.5	9.82	103.0
10H	12	0220	83.2–92.7	9.5	10.17	107.0
11H	12	0245	92.7–102.2	9.5	9.35	98.4
12H	12	0310	102.2–111.7	9.5	10.05	105.8
13H	12	0330	111.7–121.2	9.5	9.94	104.0
14H	12	0355	121.2–130.7	9.5	9.36	98.5
15H	12	0425	130.7–140.2	9.5	9.91	104.0
16V	12	0550	140.2–144.2	4.0	2.02	50.5
17V	12	0700	144.2–144.3	0.1	0.01	10.0
Coring totals				144.3	146.14	101.3
Hole 820B						
1H	12	0925	0–8.2	8.2	8.23	100.0
2H	12	0940	8.2–17.7	9.5	9.69	102.0
3H	12	0955	17.7–27.2	9.5	9.95	105.0
4H	12	1025	27.2–36.7	9.5	9.94	104.0
5H	12	1050	36.7–46.2	9.5	10.04	105.7
6H	12	1120	46.2–55.7	9.5	9.87	104.0
7H	12	1230	55.7–65.2	9.5	9.81	103.0
8H	12	1250	65.2–74.7	9.5	9.59	101.0
9H	12	1310	74.7–84.2	9.5	9.72	102.0
10H	12	1335	84.2–93.7	9.5	9.96	105.0
11H	12	1400	93.7–103.2	9.5	9.81	103.0
12H	12	1530	103.2–112.7	9.5	10.04	105.7
13H	12	1550	112.7–122.2	9.5	9.89	104.0
14H	12	1610	122.2–131.7	9.5	9.88	104.0
15H	12	1630	131.7–141.2	9.5	10.02	105.5
16H	12	1650	141.2–150.7	9.5	8.79	92.5
17H	12	1820	150.7–160.2	9.5	6.14	64.6
18X	12	1900	160.2–165.2	5.0	9.47	189.0
19X	12	1935	165.2–174.8	9.6	9.41	98.0
20X	12	2005	174.8–184.1	9.3	9.74	105.0
21X	12	2030	184.1–193.7	9.6	9.84	102.0
22X	12	2055	193.7–203.4	9.7	9.31	96.0
23X	12	2215	203.4–212.8	9.4	8.74	93.0
24X	12	2245	212.8–222.5	9.7	9.19	94.7
25X	12	2305	222.5–232.1	9.6	4.71	49.0
26X	12	2340	232.1–241.8	9.7	2.18	22.5
27X	13	000	241.8–251.1	9.3	7.67	82.5
28X	13	0125	251.1–260.8	9.7	9.51	98.0
29X	13	0155	260.8–270.4	9.6	6.23	64.9
30X	13	0235	270.4–280.1	9.7	3.33	34.3
31X	13	0305	280.1–289.7	9.6	0.48	5.0
32X	13	0350	289.7–299.4	9.7	3.10	31.9
33X	13	0545	299.4–309.1	9.7	8.36	86.2
34X	13	0625	309.1–318.8	9.7	0.83	8.6
35X	13	0800	318.8–328.5	9.7	3.75	38.6
36X	13	0940	328.5–338.2	9.7	9.93	102.0
37X	13	1110	338.2–347.9	9.7	6.13	63.2
38X	13	1210	347.9–357.5	9.6	5.84	60.8
39X	13	1245	357.5–362.7	5.2	4.27	82.1
40X	13	1435	362.7–367.1	4.4	3.81	86.6
41X	13	1540	367.1–376.7	9.6	6.99	72.8
42X	13	1650	376.7–386.4	9.7	7.87	81.1
43X	13	1755	386.4–396.0	9.6	0.25	2.6
44X	13	1855	396.0–400.0	4.0	2.60	65.0
Coring totals				400.0	324.91	81.2

Note that times are given in Universal Time Coordinated or UTC, which is 10 hr later than local time or L.

reason for this difference in seismic character probably relates in part to processing and displaying parameters used during stacking of BMR *Rig Seismic* data. All the underlying units to beyond TD are progradational facies. The top progradational unit, which is about 0.09 s TWT (~70 m) thick, has a gentle sigmoidal character and consists of high-amplitude reflectors. The remainder of the reflectors (about 0.3 s TWT, or 275 m, thick) has a complex sigmoid-oblique character and contains zones of both high and low amplitude. Site 820 intersects the outer part of the top sets of most of the progradational units and only nears the foreset facies close to TD.

To provide some predictive capability during drilling at Site 820, we estimated the TWT/depth relationship below the seafloor using stacking-derived interval velocities from BMR seismic lines across the site. In Figure 5, we compare this relationship with similarly derived TWT/depth curves for adjacent Sites 819 and 821.

LITHOSTRATIGRAPHY

Lithologic Units

Site 820 is the central site in a transect of three holes (Sites 819 to 821) across the upper slope, immediately east of modern Great Barrier Reef. During APC and VPC operations at Hole 820A, we cored 144.3 m, with 100% recovery. In Hole 820B, approximately 20 m west of Hole 820A, we recorded more than 80% recovery from APC (to 160.2 m) and XCB (to 400.0 m) coring.

Lithologies recovered consisted almost exclusively of greenish-gray to dark greenish-gray, mud-sized wackestone/mixed sediments interbedded with coarser (to medium sand-sized), greenish-gray bioclastic packstone. The range of lithologies within this entirely Pleistocene sequence reflects the varying contributions of shelf carbonates and terrigenous detritus. Subtle variations in grain-size trends and composition have permitted identification of three lithologic units. Unit I (0–150.7 mbsf) generally is finer-grained than underlying units and consists of bioclastic, very fine sand-sized wackestone and mudstone, interbedded with bioclastic packstones. Unit II (150.7–208.1 mbsf) is a transitional unit that consists of three 13- to 16-m-thick upward-coarsening sequences of bioclastic, clayey wackestone/mudstone grading up to very fine to fine sand-sized packstone, together with a thick (7 m) mudstone/wackestone unit and a single basal upward-fining sequence. Unit III (208.1–400.0 mbsf) consists of five thick (22–48+ m) upward-coarsening sequences, characterized by small but definite transitions from mud-sized material up to very fine to fine sand-sized detritus.

Unit I (Sections 133-820A-1H-1 to -17V-CC and 133-820B-1H-1 to -16H-CC, 0–150.7 mbsf; age, Pleistocene, CN15–CN13b, 0–1.27 Ma)

Unit I is dominated by relatively fine-grained mixed sediments and claystones, with interbedded fine sand-sized bioclastic packstones and wackestones. Unit I can be subdivided into two subunits: the upper Subunit IA (133-820A-1H-1 to -8H-1, 13 cm; 133-820B-1H-1 to -7H-6, 25 cm; 0–64.3 mbsf), containing thick beds of mud-sized, dark gray, terrigenous clay-rich mixed sediment (see Fig. 6); and the lower, more carbonate-rich Subunit IB (133-820A-8H-1, 13 cm, to -17V-CC and 133-820B-7H-6, 25 cm, to -16H-CC; 64.3–150.7 mbsf), consisting of interbedded packstone/wackestone and calcareous mixed sediments. The proportion of dolomite increases toward the base of the unit (see "Inorganic Geochemistry" section, this chapter). Bioturbation mottling is

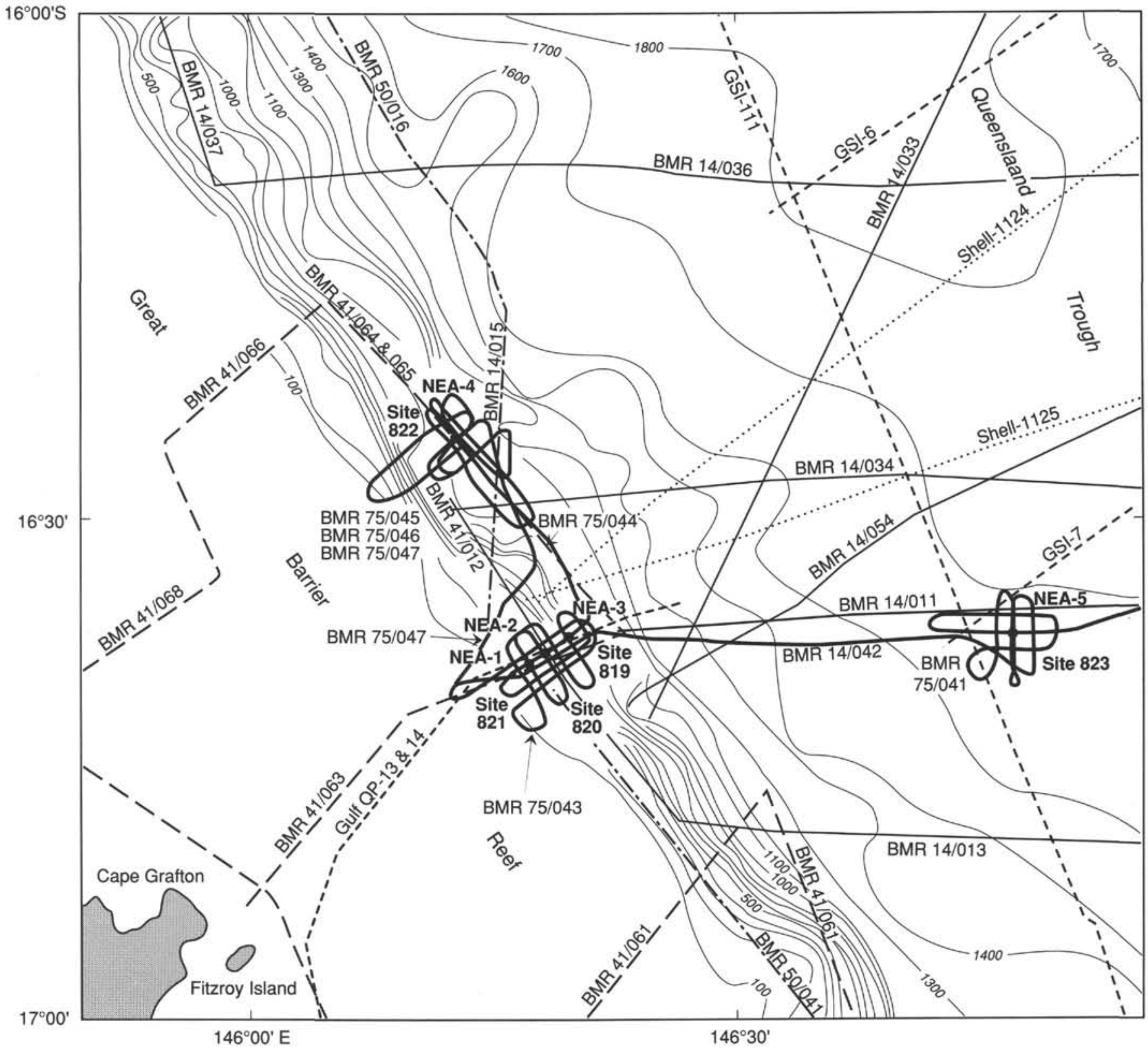

Figure 2. Track chart showing distribution of regional seismic data in the area around Sites 819, 820, and 821. Also shows locations of Sites 822 and 823, and simplified bathymetry in meters.

pervasive throughout the entire unit. Burrows within the finer-grained portion of the unit commonly are filled in with coarser-grained foraminifers and bioclasts.

The dominant lithology in Subunit IA is a dark greenish-gray, unlithified, mud to very fine sand-sized, calcareous, clayey mixed sediment or clayey wackestone with nannofossils. In addition to the clay component in the darker mixed sediments, terrigenous material also is present as silt- and very fine sand-sized grains of quartz and feldspar. The finer-grained beds in Subunit IB are almost exclusively greenish-gray to dark greenish-gray clayey wackestones with nannofossils, with only minor occurrences of mixed sediments (i.e., beds with <60% carbonate content).

The coarser-grained components within both Subunits IA and IB consist of greenish-gray to dark greenish-gray, fine to medium sand-sized, bioclastic packstone or wackestone beds with foraminifers and nannofossils. Silt-sized quartz and feldspar grains form a small component within most packstone and wackestone beds. Bed thickness ranges from approximately 20 cm to 1 m, although pervasive bioturbation throughout the unit has resulted in gradational bed boundaries. Subunit IB contains packstone beds having more "chalky," partially lithified zones.

In addition to these normal beds, unusual, very coarse-grained beds also occur. At 121.5 to 125.0 mbsf (133-820A-14H-1, 30 cm, to -14H-3, 130 cm), a 3.5-m-thick, dark greenish-gray, highly bioturbated, poorly sorted bioclastic wackestone to floatstone can be seen. This bed contains abundant *Halimeda* fragments (Fig. 7A), together with abundant bryozoan and molluscan fragments and other bioclasts up to very coarse sand-size. Both bed boundaries are gradational. By contrast, in Hole 820B, the equivalent horizon (133-820B-14H-1, 30 cm, to -14H-3, 130 cm) is different. Coarse bryozoan and molluscan bioclasts are still present, together with rare

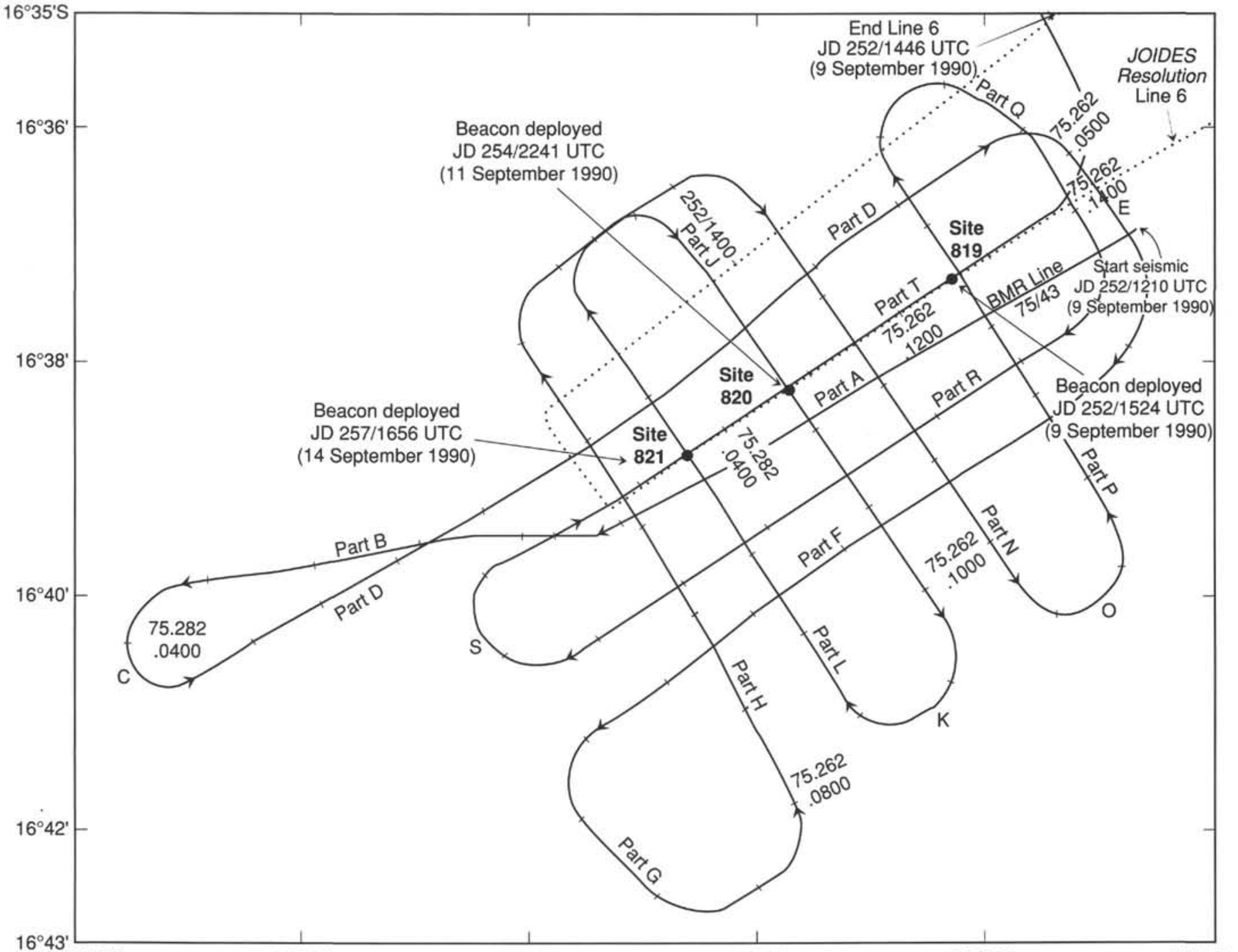

Figure 3. *JOIDES Resolution* Leg 133 site-location tracks (dotted line) and *Rig Seismic* 1987 site-survey tracks (solid line) around Sites 819, 820, and 821.

coral fragments and quartz and glauconite grains, within a light greenish-gray, calcareous, bioclastic silty mudstone with siliciclastic grains, but no *Halimeda* flakes were identified in this bed (Fig. 7B).

At 31.2 to 33.6 mbsf (133-820B-4H-3, 97 cm, to -4H-5, 40 cm), a dark gray to very dark gray sandstone/conglomerate, containing granule- and pebble-sized rhodoliths, intermixed with bioclastic detritus within very dark gray silty mudstone was observed. Bioclastic fragments within this bed include coral, coralline algal, mollusk and echinoid fragments up to coarse sand-sized, and abundant benthic and planktonic foraminifers. Both upper and lower bed boundaries are gradational. A similar bed, although much thinner (only 1.1 m thick) and finer (coarsest grains are up to very coarse sand-size), occurs at 6.6 to 7.7 mbsf (133-820B-1H-5, 60 cm, to -1H-6, 25 cm).

Unit II (Sections 133-820B-17H-1, 0 cm, to -23X-4, 2 cm; depth, 150.7–208.1 mbsf; age, Pleistocene, CN13b, 0.93–1.27 Ma)

Unit II consists of a mixture of relatively coarse bioclastic packstones, finer bioclastic clayey mixed sediments, and very fine-grained silty claystones. Dolomite occurs throughout the unit. This unit represents a transition from the essentially fine-grained Unit I to the thicker, upward-coarsening cycles of Unit III. Although dominated by upward-coarsening sequences, Unit II also includes both upward-fining and uniformly fine-grained sequences.

The base of Unit II is marked by an abrupt transition from uniform packstones at the top of Unit III, into a 1-m-thick upward-fining sequence. This sequence grades from a medium-to-coarse sand-sized, greenish-gray, firm to partially lithified, clayey bioclastic packstone; to silt- to very fine sand-sized, greenish-gray, firm, calcareous, clayey mixed sediment with bioclasts, and then into a 7-m sequence of very dark gray claystone that contains silt-sized micrite, bioclast, and quartz grains. Minor bioturbation occurs throughout the finer-grained parts of this sequence, with many burrows filled in with medium-to-coarse sand-sized grains, mostly foraminifers and bioclasts.

This thick claystone sequence is overlain by three upward-coarsening sequences, within an overall upward-fining trend. The lower two upward-coarsening sequences (from 133-820B-20X-3, 130 cm, to -22X-1, 60 cm, and 133-820B-18X-4, 0 cm,

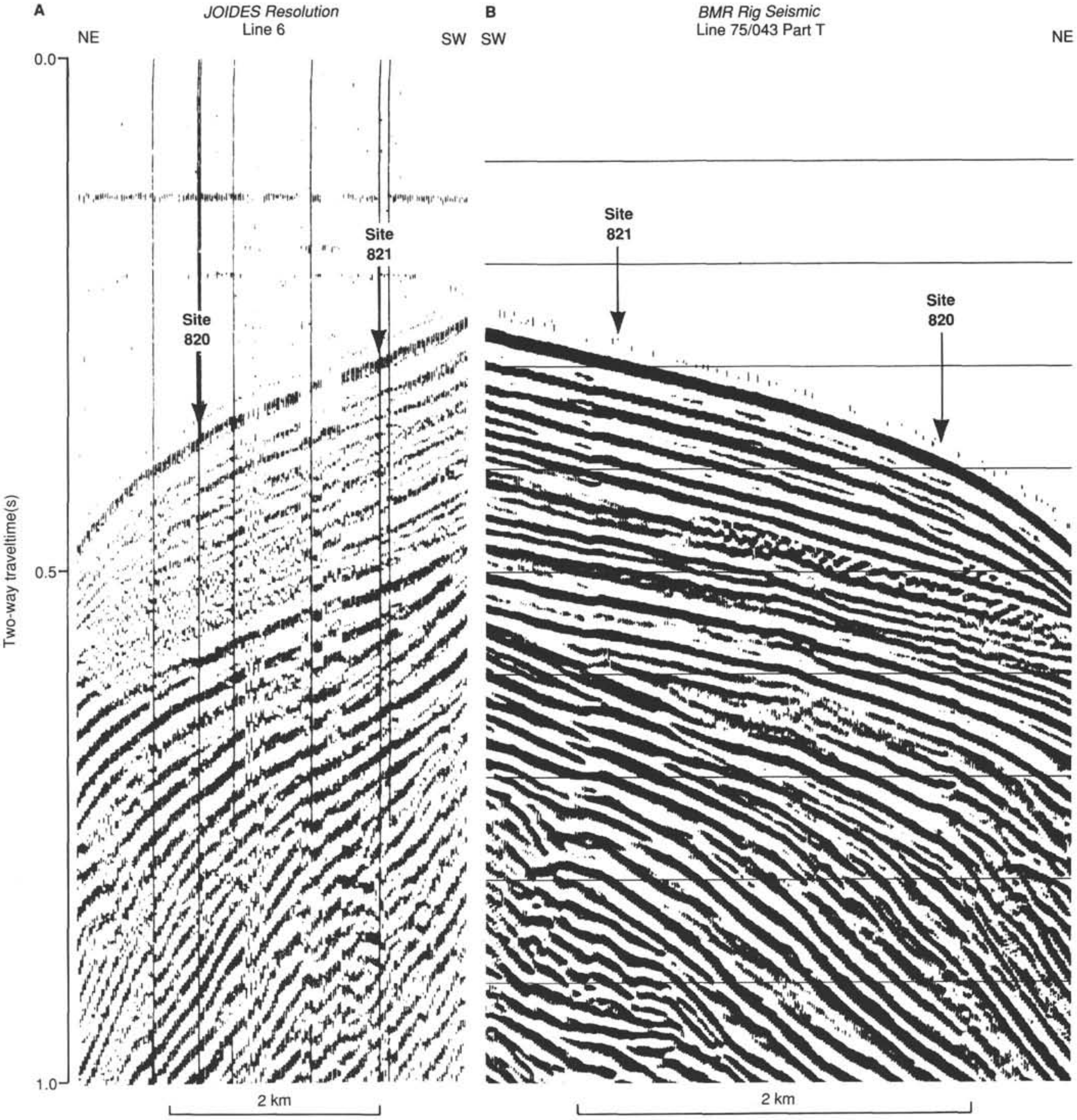

Figure 4. Comparison of *JOIDES Resolution* (**A**) and *Rig Seismic* (**B**) 80-in.^{3} water-gun seismic profiles across Site 820.

to -20X-3, 130 cm) consist of silt-sized, greenish-gray, clayey mixed sediment with micrite and bioclasts grading up to silt- to fine sand-sized, greenish-gray, partially to moderately lithified, nannofossil calcitic packstone with micrite, clay, and bioclasts.

The uppermost part of this unit consists of a thinner and finer upward-coarsening sequence (from 133-820B-17H-1, 0 cm, to -18X-3, 150 cm), with a grain size gradation within dark gray, bioturbated nannofossil mixed sediment with quartz and micrite from silt- to fine sand-size.

Unit III (Sections 133-820B-23X-4, 2 cm, to -44X-CC; depth, 208.1–400.0 mbsf); age, Pleistocene; CN13b, 1.27–1.48 Ma)

Unit III is dominated by bioclastic packstones, with interbedded finer-grained calcareous mudstones and mud-sized mixed sediments. The unit can be subdivided into five sequences, each representing a single, subtle, upward-coarsening cycle. The finer parts of each cycle consist of partially lithified, dark greenish-gray, calcareous mudstone with bioclasts and nannofossils, whereas the coarser portions of each

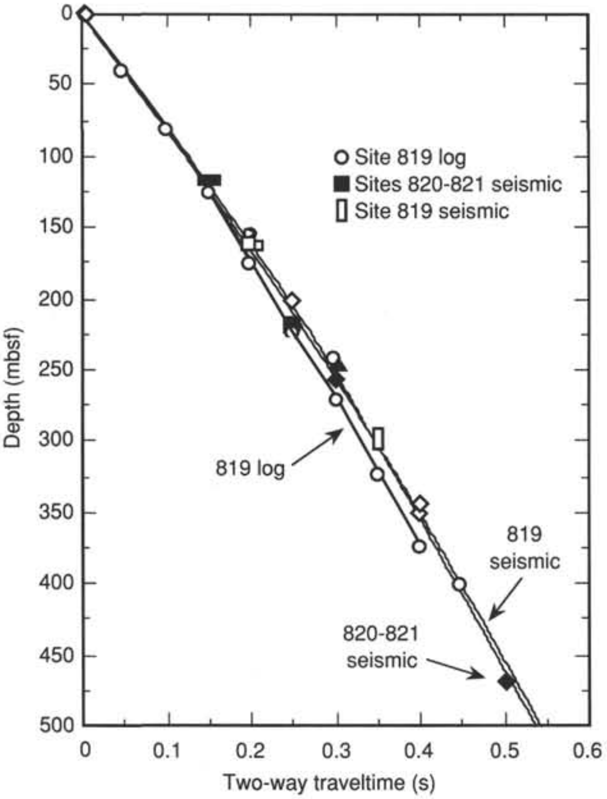

Figure 5. Comparison of TWT/depth curve estimated for Site 820 with those for Sites 819 and 821.

cycle consist of partially to moderately lithified, calcareous, bioclastic, "chalky" packstone with feldspar, quartz, clay, and nannofossils. Unit III cycles 2, 3, and 4 also contain significant proportions of dolomite (see "Inorganic Geochemistry" section, this chapter). The coarsest grains in each cycle are fine-to-medium sand-sized. The subtlety of the variations in grain size (represented by each of the identified cycles) is that the coarsest parts of each cycle contain significant proportions of mud-sized materials. Similarly, the finer parts contain very fine or fine sand-sized detritus, which normally occurs as thin (2–4 cm), greenish-gray, foraminifer bioclast packstone beds. Variations in grain size within each cycle thus are slight in the relative proportions of mud- to sand-sized components. Bioturbation mottling occurs throughout Unit III; in some cases, completely disrupting thinner beds. This is particularly obvious where thin coarser beds occur within the finer portions of each cycle. Despite the pervasive bioturbation mottling, lamination occurs within all sequences, except cycle 5. Lamination occurs as thin, darker "wisps" within the coarser packstone beds, and as more continuous horizontal lamination within finer beds. One example of cross lamination occurs in cycle 4 (at 133-820B-37X-3, 80 cm). Within cycle 3, an unusually high proportion of molluscan bioclastic material also was observed at 133-820B-36X-5, 95 cm, to -36X-CC.

The cycle 5 sequence differs slightly from overlying portions of Unit III in having greater uniformity and lacking both lamination and clear bedding boundaries (although this may be the result of a combination of XCB drilling disturbance and pervasive bioturbation).

Interpretation

The suite of lithological and other data from Site 820, when combined with data from Sites 819 and 821 and seismic and log ties between each of these sites, has the potential to reveal a detailed and tightly constrained interpretation of sedimentary processes on shelf margins. As a first step, we were able to make limited interpretations of lithologies recovered at Site 820.

Each of the upward-coarsening cycles comprising Unit III represents a slight increase in depositional energy. Seismic data show that each upward-coarsening sequence corresponds to a single shelf-margin progradational cycle (see "Seismic Stratigraphy" section, this chapter). Therefore, each cycle may represent a regressive, upward-shallowing sequence, while deposition is controlled by a base level, determined by the relationship between variation in sea level and subsidence. Fluctuations between outer neritic (100–200 m) and upper bathyal (200–600 m) water depths, determined from a limited number of benthic foraminifer analyses (see "Biostratigraphy" section, this chapter), indicate that the upward-coarsening cyclicity of Unit III may reflect upward-shallowing cycles near the boundary between upper bathyal and outer neritic depth zones (i.e., approximately 200 m).

The upward-coarsening cycles comprising the upper part of Unit II may have been similarly deposited as regressive, upward-shallowing sequences. The thinner cycles and the slightly finer grain size of the coarsest portions of each cycle, together with evidence of an overall upward-deepening from benthic foraminifer analyses (see "Biostratigraphy" section, this chapter), indicate deposition in a slightly deeper environment compared with Unit III, probably entirely within the upper bathyal range.

The continuation of progradational seismic geometries, similar to those corresponding to the lower part of Site 820 (Units II and III), into much deeper parts of the sediment pile (see Fig. 4 in "Site Geophysics" section, this chapter) suggest that these may represent similar upward-coarsening and upward-shallowing cycles, although not necessarily with the same compositional variation.

The well-developed cyclicity apparent within Subunit IA (which occurs as gradational variation in the proportion of darker-colored, terrigenous clay within mud-sized, clayey mixed sediments or mudstone horizons relative to the lighter-colored, clayey wackestone horizons containing higher calcium carbonate contents) reflects variability in the relative contributions of shelfal carbonate and terrigenous detritus. This variation probably was controlled by glacial/interglacial cyclicity in sea level.

The coarse-grained bed containing abundant *Halimeda* flakes at 121.5 to 125.0 mbsf in Hole 820A and the equivalent, coarse, bioclast-bearing bed lacking *Halimeda* in Hole 820B only 20 m away indicate pronounced lateral bed discontinuity. Either this is the result of an original channelized depositional geometry, if the *Halimeda* and other bioclastic material were emplaced by sediment gravity flow, or it may indicate that Hole 820A penetrated the edge of an *in-situ Halimeda*-dominated mound. Discrimination between these possibilities may be possible after more detailed examination of the bioclastic material within each core.

BIOSTRATIGRAPHY

The expanded Pleistocene section recovered at Site 820 generally is rich in calcareous microfossils. Preservation of these microfossils varies from excellent in clayey intervals to poor in sandy intervals. Four nannofossil events were recognized and used to subdivide the section into four zones/subzones (Fig. 8). Calcareous nannofossils indicate that the sequence is complete, while the oldest sediment penetrated (400 mbsf) has an age between 1.27 and 1.48 Ma. Planktonic foraminifers are in agreement with this assess-

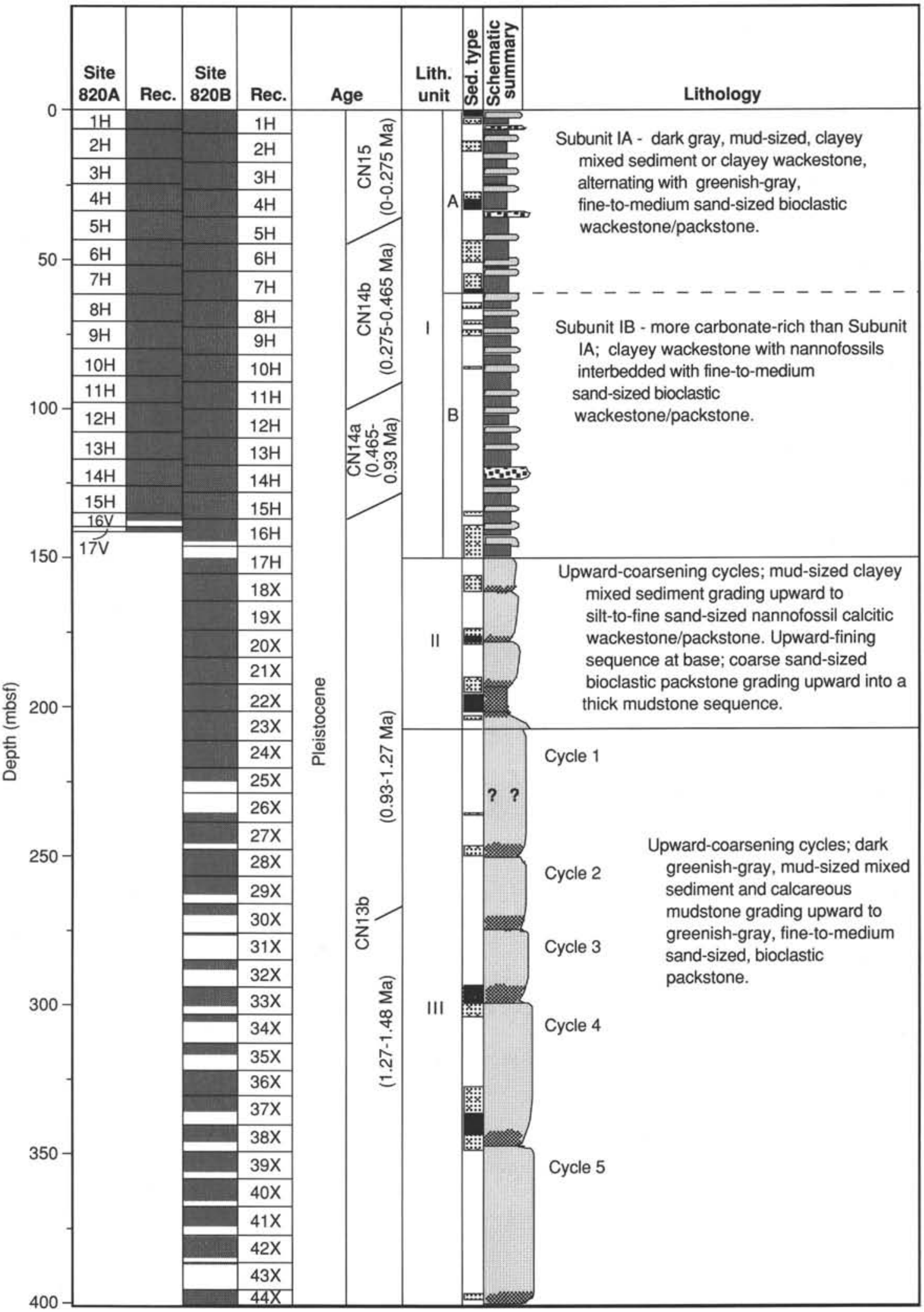

Figure 6. Summary chart showing lithology for each lithologic unit identified at Site 820. Shading indicates core recovery for each hole. Biostratigraphic data are from analyses of planktonic foraminifer and nannofossil associations (see "Biostratigraphy" section, this chapter). The column showing sediment type is based on carbonate analyses (see "Inorganic Geochemistry" section, this chapter) and shows distribution of carbonate sediments (clear = >60% $CaCO_3$); mixed sediments (stippled = between 40% and 60% $CaCO_3$); and siliciclastic sediments (black = <40% $CaCO_3$). Schematic summary is a graphic representation of variations in grain size, with coarser-grained beds and sequences projecting farther right. Question marks within cycle 1 of Unit III mark possible position of a farther cycle boundary, based on logs (see "Downhole Measurements" section, this chapter) in an interval of no recovery in the core.

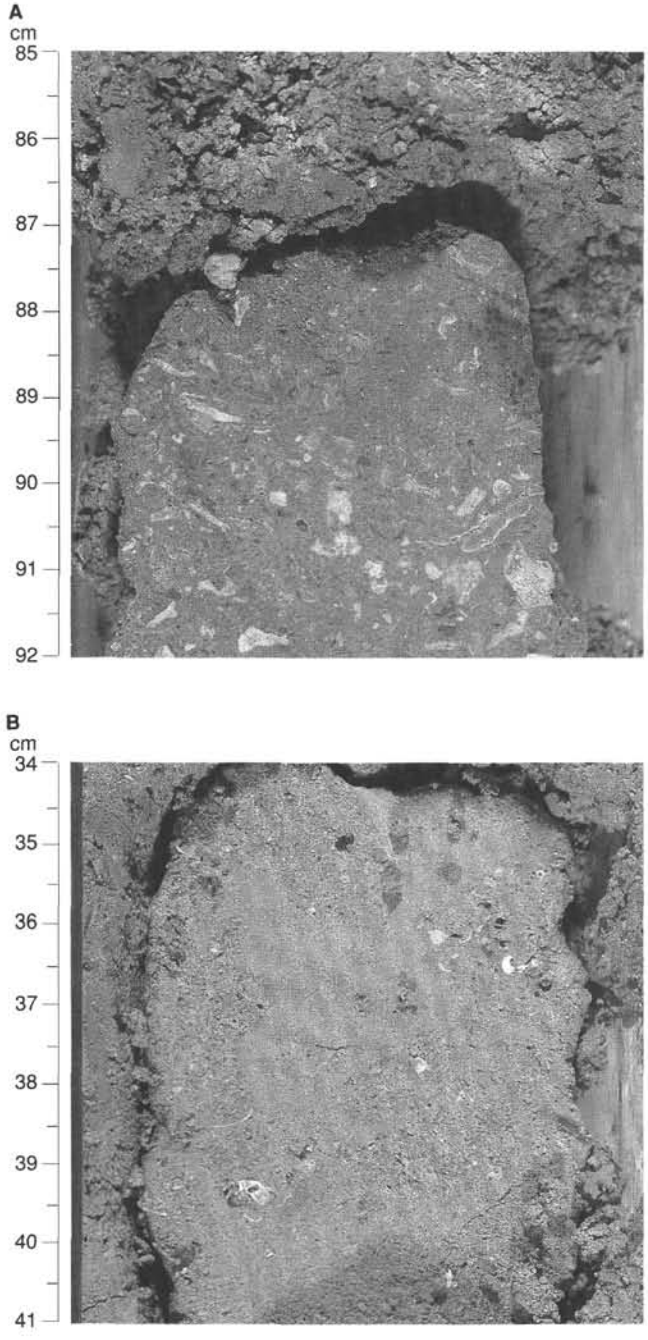

Figure 7. Photographs showing equivalent horizons in Holes 820A and 820B. **A.** Photograph of 85 to 92 cm in Section 133-820A-14H-2 (123.6 mbsf), showing *Halimeda* flakes and fragments, together with other bioclastic material, distributed throughout partially lithified, dark greenish-gray, highly bioturbated, bioclastic wackestone/floatstone. **B.** Photograph of 34 to 41 cm in Section 133-820B-14H-2 (124.1 mbsf), showing numerous and diverse bioclastic fragments distributed throughout partially lithified, dark greenish-gray, highly bioturbated, bioclastic wackestone.

ment of nannofossil age. Benthic foraminifers indicate that sediments above 150 mbsf were deposited in an upper bathyal environment and that paleodepth fluctuated between upper bathyal and outer neritic for sediments below 150 mbsf (see also "Sedimentation Rates" section, "Site 819" chapter (this volume).

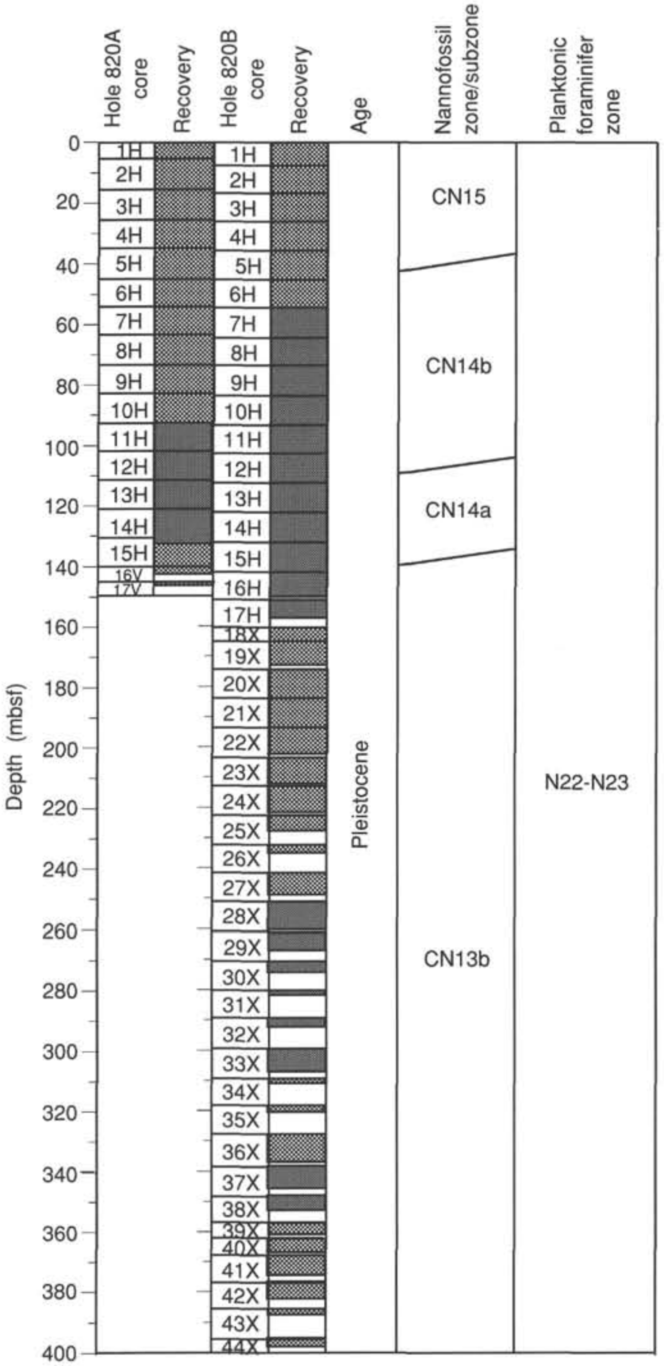

Figure 8. Preliminary nannofossil and foraminifer biostratigraphy, Site 820.

Calcareous Nannofossils

From Site 820, as at the previous Site 819, we recovered an expanded Pleistocene section (400 m of sediment representing <1.48 m.y.). One sample per core was examined for calcareous nannofossils from both Holes 820A and 820B. Almost all the samples are rich in nannofossils; preservation of nannofossils is generally good in the upper 100 m, moderate-to-poor in the next approximately 200 m, then improves again from about 300 to 400 mbsf. Note, however, that fossil preservation is closely linked to subtle lithologic changes, and these changes may occur at closer spacing than the 9.5-m spacing of core-catcher samples analyzed for nannofossils.

In Hole 820B, the stratigraphic sequence cored in Hole 820A is repeated for the upper 150 m and extends to 400 mbsf. Because the nannofossil biostratigraphy from Hole 820A repeats that from Hole 820B, we describe only the nannofossil events recognized in Hole 820B. Summaries of the biostratigraphic results from the two holes are graphically presented in Figure 8.

The lowest occurrence of *Emiliania huxleyi* is in Sample 133-820B-4H-CC, where the species is rare. Samples at this level and above were assigned to Zone CN15 (0–0.275 Ma). The interval from Samples 133-820B-5H-CC to -11H-CC contains abundant *Gephyrocapsa caribbeanica* and/or *G. oceanica,* but lacks *Emiliania huxleyi* as well as *Pseudoemiliania lacunosa;* we placed it in Subzone CN14b (0.275–0.465 Ma). *Pseudoemiliania lacunosa* occurs from Samples 133-820B-12H-CC downward to the bottom of the hole and is accompanied by common-to-abundant large *Gephyrocapsa* through Sample 133-820B-14H-CC. Thus, this interval was assigned to Subzone CN14a (0.465–0.93 Ma). In Sample 133-820B-15H-CC and in several samples below it, large species of *Gephyrocapsa* are rare to very rare, while small species are overwhelmingly abundant. Sample 133-820B-15H-CC thus was taken as the top of an interval where small *Gephyrocapsa* (0.93 Ma) dominated.

Helicosphaera sellii occurs in Sample 133-820B-30X-CC; this sample has a minimum age of 1.27 Ma. It occurs within Zone CN13b. The next lower marker should be *Calcidiscus tropicus*; however, we did not observe it in this hole. This combined with the presence of large-to-medium and large species of *Gephyrocapsa* to the bottom of the hole (Sample 133-820B-44X-CC) indicates that the hole was not penetrated into the lowermost Pleistocene (i.e., below the 1.48 Ma datum).

Planktonic Foraminifers

All core-catcher samples from Hole 820A were examined for planktonic foraminifers. The upper Cores 133-820A-1H through -10H contain abundant-to-common specimens. Preservation of tests is excellent in this interval. Cores 133-820A-10H through -17V yielded common-to-rare specimens, while generally preservation is poor.

Diverse assemblages are present in the upper part (Cores 133-820A-1H through -10H); these are dominated by *Globigerinoides ruber* "white," along with other species, such as *Globigerinoides sacculifer* and *Globigerinella aequilateralis*. Typical late Pleistocene species in this interval are *Bolliella adamsi* (present only in Sample 133-820A-1H), *Bolliella praeadamsi* (Samples 133-820A-1H through -3H), *Globigerina rubescens* "pink" (Samples 133-820A-2H and -3H), and *Globigerinoides ruber* "pink" (Samples 133-820A-4H through -7H). Cores 133-820-11H through -17V did not yield age-diagnostic species, which can be ascribed mainly to deteriorating preservation of the specimens.

From Site 820B (Cores 133-820B-19X through -44X), we recovered low-diversity planktonic foraminiferal assemblages, with moderate-to-poor preservation of specimens. However, some samples (133-820B-21X-CC; 133-820B-36X-CC through -38X-CC) contain planktonic foraminifers having excellent preservation. We think that preservation of planktonic foraminifers relates to lithological variability (see "Lithostratigraphy" section, this chapter).

Benthic Foraminifers

Core-catcher samples examined from Hole 820A contain abundant, well-preserved benthic foraminifers. The benthic foraminiferal assemblages indicate an upper bathyal paleodepth (200–600 m) for Hole 820A, while Hole 820B fluctuated from outer neritic (100–200 m) to upper bathyal (200–600 m) below Core 133-820B-18X.

Most core-catcher samples examined contain upper bathyal species associations that include the depth indicators *Bulimina marginata, Bulimina mexicana, Cibicidoides, C. cicatricosus dutemplei, C. mundulus, C. pachyderma, C. subhaidingerii, Hanzawaia mantaensis, Hoeglundina elegans, Hyalinea balthica, Lenticulina peregrina, Nuttallides umbonifera, Sigmoilopsis schlumbergeri, Sphaeroidina bulloides, Uvigerina peregrina, U. pigmaea,* and *U. proboscidea* (van Morkhoven et al., 1986). Most samples that were examined include at least a small component of transported specimens, such as *Amphistegina* spp., *Discorbis* spp., and *Planorbulina* spp.

Hole 820B core-catcher samples below Core 133-820B-18X generally contain poorly preserved benthic foraminifers that are not as abundant as those in Hole 820A. Whereas poor preservation and dilution by terrigenous material yielded faunas that contain few depth-indicative benthic foraminifers, our preliminary analysis suggests that the paleodepth at Hole 820B fluctuated from outer neritic (100–200 m) to upper bathyal (200–600 m). Samples 133-820B-19X-CC, -21X-CC, -25X-CC, -36X-CC, -39X-CC, and possibly -44X-CC contain upper bathyal benthic foraminiferal assemblages. Samples 133-820B-23X-CC, -27X-CC, -29X-CC, -32X-CC, and -35X-CC contain outer neritic benthic foraminiferal assemblages. We could not estimate paleobathymetry for Sample 133-820B-42X-CC.

PALEOMAGNETISM

Two holes were drilled at Site 820. All sections of archive-halves of the cores from Hole 820A and Cores 133-820B-1H through -35X from Hole 820B were measured at 10-cm intervals using the shipboard pass-through cryogenic magnetometer both before and after AF demagnetization at a level of 15 mT. We measured whole-core magnetic susceptibilities at 10-cm intervals for all cores in both holes, using a Bartington pass-through susceptibility meter.

Paleomagnetic properties of the sediments cored in both holes are similar. Data from about the upper 100 m in each hole are of acceptable quality and may be used to determine polarities (Fig. 9). However, downhole from about a level of 100 m, directional data are extremely erratic. An example of this is shown in Figure 10, which depicts the directional and magnetic intensity data obtained after AF demagnetization at a level of 15 mT from Hole 820B in the depth interval from 160 to mbsf. We attribute the observed inclination scatter to severe drilling deformation caused by the XCB system and to re-orientation and remagnetization of some of the drilling biscuits and slurry, respectively. Some of the biscuits having diameters less than that of the core-liner may have experienced rotation about the vertical and horizontal axes during drilling, thereby causing large scatter in inclination directions. Thus, inclination data below 100 mbsf in these holes could not be used to interpret polarities. Accordingly, shore-based analyses of discrete samples collected from less disturbed (not rotated) portions of sediments from this site will be necessary to establish a reliable magnetostratigraphy.

Figure 9 depicts inclination data for the upper 100 m of sediments recovered in Holes 820A and 820B. These data were obtained after AF demagnetization at 15 mT. In this depth interval, inclinations are predominantly normal, with most inclination values at about 30°, near the expected geocentric axial dipole inclination for Site 820 (±30.9°). A stable magnetic remanence was isolated upon 15-mT demagnetization, which may tentatively be used to interpret magnetostratigraphy. We are not sure of the relative contribution of

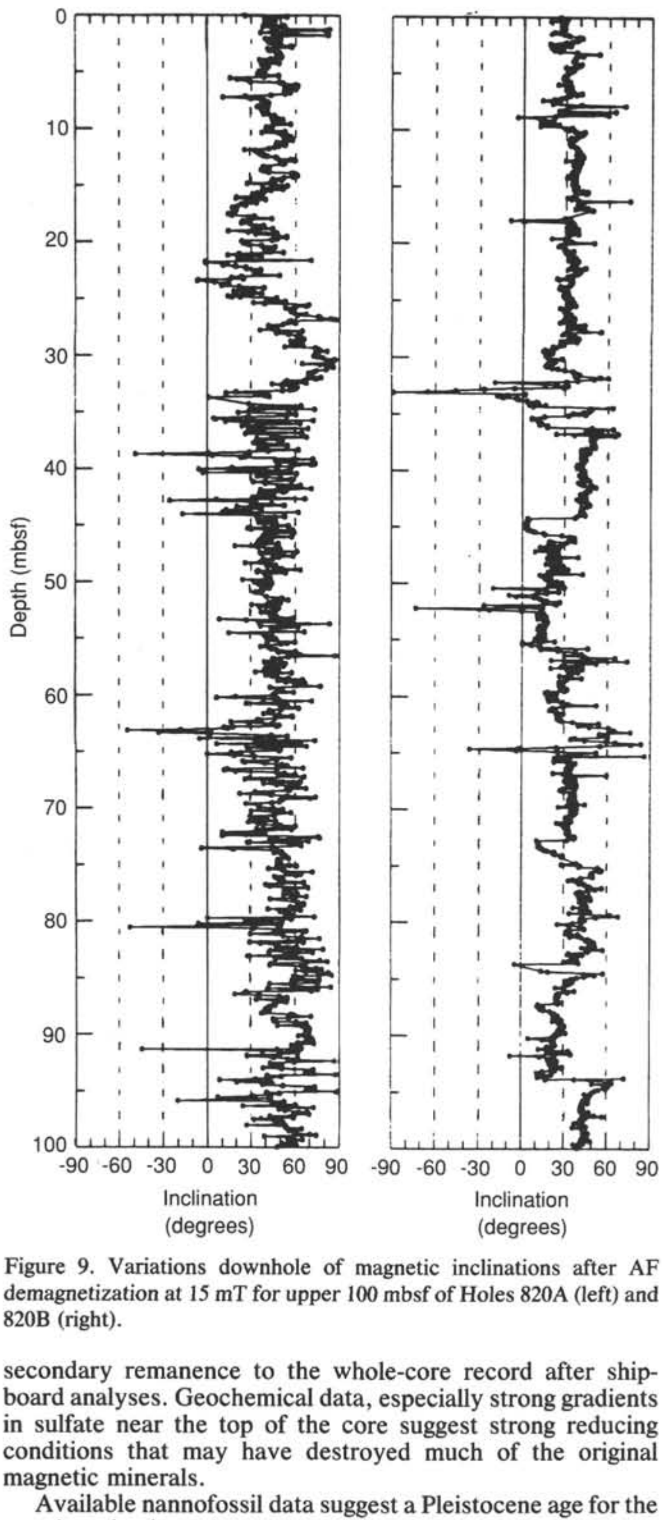

Figure 9. Variations downhole of magnetic inclinations after AF demagnetization at 15 mT for upper 100 mbsf of Holes 820A (left) and 820B (right).

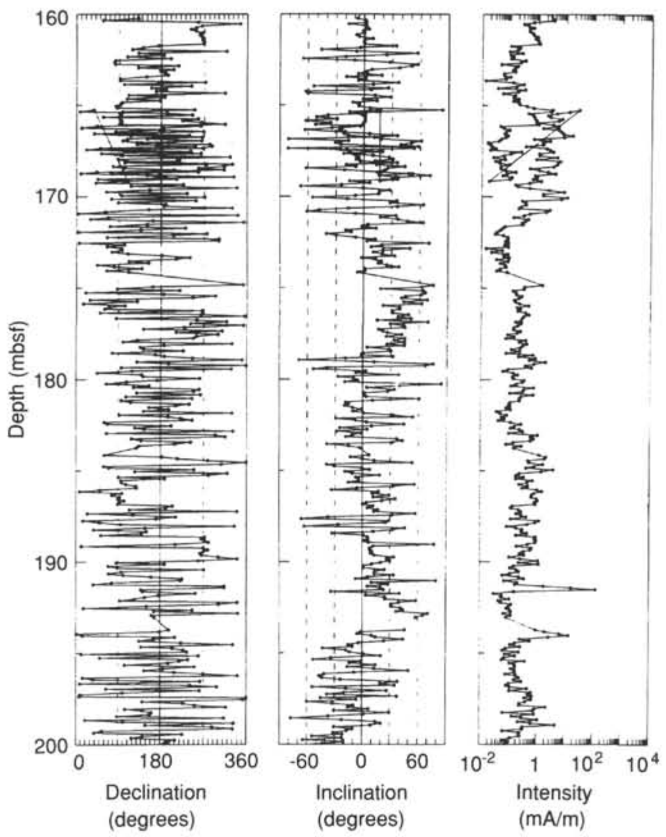

Figure 10. Example of scattered operation results obtained from XCB cores in Hole 820B, 160–200 mbsf.

secondary remanence to the whole-core record after shipboard analyses. Geochemical data, especially strong gradients in sulfate near the top of the core suggest strong reducing conditions that may have destroyed much of the original magnetic minerals.

Available nannofossil data suggest a Pleistocene age for the cored section in each hole (see "Biostratigraphy" section, this chapter). These data also suggest that the Brunhes/Matuyama boundary should lie below 110 mbsf. Therefore, we tentatively concluded that the upper 100 m of the cored sediments imprinted with normal polarity either were deposited or overprinted/remagnetized during the Brunhes normal chron. Based on nannofossil data, the upper 100 m of Site 820 is less than 0.5 m.y.

Variations downhole of NRM intensity and magnetic susceptibility for the upper 100 m in both holes is shown in Figures 11 and 12. Susceptibility and NRM intensity values between the two holes co-vary. Large peaks and troughs in the two data sets correlate well within each hole (e.g., susceptibility peaks at 5, 32, and 65 mbsf correlate with intensity peaks at the same depth levels) and between holes. Peaks in intensity and susceptibility correspond to relatively high noncarbonate contents in these sediments (see "Inorganic Geochemistry" section, this chapter). NRM intensity and magnetic susceptibility data of this site can provide a simple and rapid method for interhole and regional-scale correlation of lithostratigraphy. Furthermore, variations in susceptibility may reflect major changes in relative sea level, with increased terrigenous (magnetic) influx during lowstands of sea level.

INORGANIC GEOCHEMISTRY

Interstitial Waters

Interstitial water samples were taken from Cores 133-820A-1H to -10H and 133-820A-13H, -16V, -17X, -20X, -23X, -27X, -33X, -36X, -39X, and -42X. In addition, the "Barnes" downhole water sampler (WSTP) was deployed before Cores 133-820A-12H, -17X, -23X, -28X, -30X, and -33X. Samples were squeezed and analyzed according to the methods outlined in the "Explanatory Notes" chapter (this volume).

Calcium, Magnesium, Potassium, and Strontium

Concentrations of calcium decrease from a surface-water value of 10.56 to 3.63 mM at 382.6 mbsf (Fig. 13 and Table 2). The interstitial-water profile of Mg^{2+} is similar to that of calcium, with a decrease from surface-water concentration of 52.50 to 9.41 mM at 382.6 mbsf (Fig. 13 and Table 2).

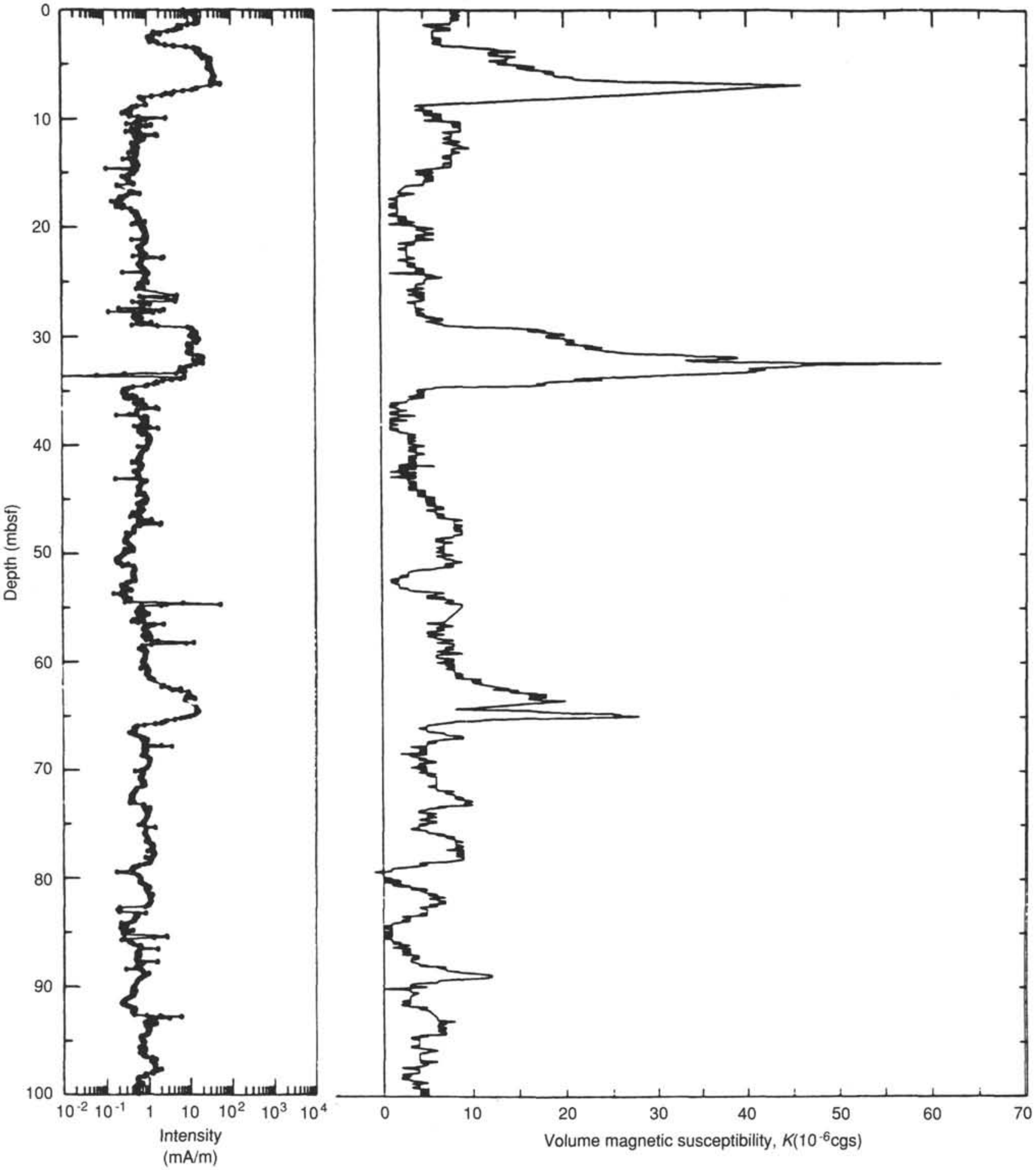

Figure 11. Variations downhole of NRM intensity and magnetic susceptibility for upper 100 m, Hole 820A.

Concentrations of Sr^{2+} increase from a surface-water value of 114 to 575 μM at the bottom of the cored interval (Fig. 13 and Table 2). A downward increase in Sr^{2+} results from diagenesis of carbonate minerals. Concentrations of potassium are 10.68 mM in seawater, but decrease to 2.49 mM at 382.6 mbsf (Fig. 13 and Table 2).

When concentrations are normalized to surface-water chlorinity, an average loss of 7.5 mM of Ca^{2+} and 43 mM of Mg^{2+} takes place (Fig. 14). Calcium probably is being used to form authigenic calcite, whereas Mg^{2+} is being consumed during formation of dolomite. Potassium also is being depleted in the pore waters and shows a net loss of 8.10 mM (Fig. 14). The loss of K^+ and some Mg^{2+} may be the result of uptake into clays.

Chloride

Concentrations of chloride decrease from a seawater value of 555.55 to 536.06 mM at the bottom of the cored interval (Fig. 13 and Table 2). The relationship between salinity and chlorinity is

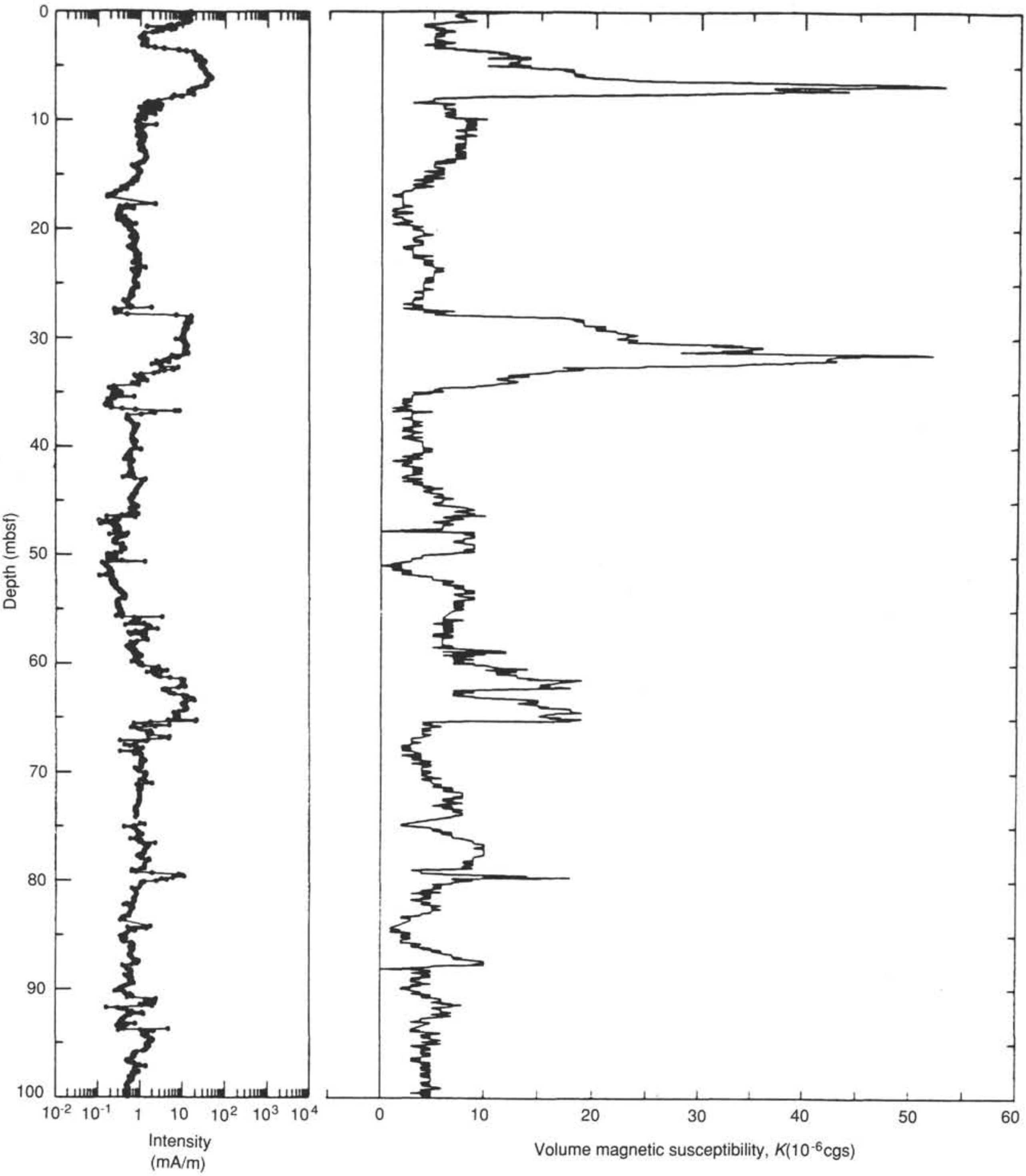

Figure 12. Variations downhole of NRM intensity and magnetic susceptibility for upper 100 m, Hole 820B.

not conservative at this site (Fig. 15). Most samples are depleted in salinity relative to their concentration of Cl^-; therefore, salinity is being reduced by diagenetic reactions within the sediments that involve removal of Ca^{2+}, Mg^{2+}, HCO_3^-, and SO_4^{2-} from pore fluids as authigenic precipitates.

Alkalinity, Ammonia, Phosphate, and Sulfate

Sediments at Site 820 are characterized by sulfate reduction, as is often seen in other hemipelagic sequences (Gieskes, 1981). As a result, the profiles of alkalinity, ammonia, and sulfate are related (Fig. 16 and Table 2).

Concentrations of sulfate decrease rapidly from surface-water values of 29.39 to 0 mM at 52.65 mbsf (Fig. 16 and Table 2). Values remain at or near zero for the remainder of the sampled section, except for a slight increase to values of 3.54 mM at 360.4 mbsf. We postulate that the small increases in sulfate lower in the section are not significant and result merely from contamination by modern seawater.

Table 2. Interstitial water data, Site 820.

Sample	Depth (mbsf)	pH	Alkalinity (mM)	Salinity (g/kg)	Calcium (mM)	Magnesium (mM)	Chloride (mM)	Silica (μM)	Strontium (μM)	Sulfate (mM)	Ammonia (μM)	Potassium (mM)	Phosphate (μM)
Seawater	0.00	8.10	2.574	35.000	10.56	52.50	555.55	3	114	29.39	0	10.68	1
133-820A-													
1H-5, 145-150	7.45	7.47	6.384	35.000	8.39	53.80	554.57	190	103	24.91	0	10.20	7
2H-5, 145-150	14.65	7.56	5.386	36.200	6.96	51.13	560.42	154	126	22.46	0	10.11	4
3H-5, 145-150	24.15	7.52	5.501	34.000	6.88	43.31	562.37	174	175	16.62	521	9.41	3
4H-5, 145-150	33.65	7.48	6.157	33.000	6.22	34.33	558.47	105	210	9.63	1042	7.98	2
5H-5, 145-150	43.15	7.41	6.490	32.000	5.20	27.07	553.60	203	241	3.46	1782	7.51	2
6H-5, 145-150	52.65	7.50	7.621	31.800	4.89	22.12	551.65	156	221	0.00	1947	6.92	3
7H-5, 145-150	62.10	7.94	7.901	31.800	4.62	20.69	554.57	106	227	0.80	1974	6.36	1
8H-5, 145-150	71.60	7.63	7.700	31.500	4.04	18.91	543.85	172	271	0.00	2111	6.31	2
9H-5, 145-150	81.10	7.44	7.348	30.500	6.54	15.76	538.98	170	318	0.00	2029	5.65	2
10H-5, 145-150	90.60	7.67	6.365	31.200	3.15	12.80	542.88	146	304	0.00	1974	5.58	2
12H-1, 0–7	103.20	7.91	7.311	31.000	2.74	9.58	538.98	128	331	0.00	1508	4.67	2
13H-5, 145-150	119.10	8.02	5.613	30.200	3.01	8.73	541.90	149	426	0.88	1179	4.86	2
16V-5, 145-150	141.60	7.79	6.652	31.000	3.53	14.80	539.95	113	331	3.23	2029	5.50	2
133-820B-													
17H-1, 0-7	150.70	7.95	3.217	34.000	8.24	43.47	546.78	65	251	2.00	823	8.42	2
17H-3, 140-150	155.10	7.88		31.000	2.44	7.25	537.03	128	400	0.29	1316	4.01	2
20X-5, 145-150	182.20	7.82	7.651	31.000	2.31	5.65	536.06	149	444	0.29	1289	2.89	2
23X-1, 0-7	203.40	8.44	7.840	32.500	4.20	15.85	538.98	103	369	7.93	1289	4.29	2
23X-2, 145-150	206.3	7.89	6.981	30.200	2.31	4.88	538.01	146	416	0.43	905	2.65	2
27X-3, 145-150	246.2	7.89	6.214	30.200	1.80	3.89	539.95	147	471	0.36	877	2.25	2
28X-1, 0-7	251.1	8.16		31.000	4.66	15.99	550.68	153	573	9.90	2248	3.25	2
30X-1, 0-7	271.8	7.94	5.382	31.800	4.32	11.2	549.7	170	421	5.86	1700	3.08	2
33X-1, 0-7	299.4	8.29	3.902	35.000	9.38	44.96	536.06	97	353	26.47	2358	7.47	10
33X-1, 140-150	300.8	8.23	6.604	30.000	2.81	5.77	535.08	135	554	0.00	658	2.03	2
36X-5, 140-150	335.9	8.14	5.716	30.500	2.94	9.05	541.9	149	504	2.62	631	2.43	2
39X-2, 140-150	360.4			30.500	3.48	9.25	536.06	142	642	3.54	1618	2.58	2
42X-4, 140-150	382.6	7.89	6.195	30.200	3.63	9.41	536.06	153	575	2.20	1015	2.49	2

At Site 820, alkalinity values increase from a surface-water value of 2.57 mM to a maximum value of 7.9 mM at 62.10 mbsf (Fig. 16 and Table 2). A peak in alkalinity between 43.15 and 90.60 mbsf corresponds to a maximum in ammonia and a minimum in sulfate concentrations within this interval. Below 119 mbsf, alkalinity increases to a maximum value of 7.7. Alkalinity values decrease slightly over the remainder of the sampled interval to a value of 5.72 mM at 335.9 mbsf (Fig. 16 and Table 2). During sulfate reduction, for every mole of sulfate consumed, two moles of alkalinity should be produced, as shown by the reaction:

$$(CH_2O)_{106}(NH_3)_{16}(H_3PO_4) + 53\ SO_4^{2-} = \qquad (1)$$
$$106\ HCO_3^- + 53\ H_2S + 16\ NH_3 + H_3PO_4$$

The first term in Equation 1 is a simplified organic molecule with Redfield stoichiometry of 106:16:1 (C:N:P). Based on the

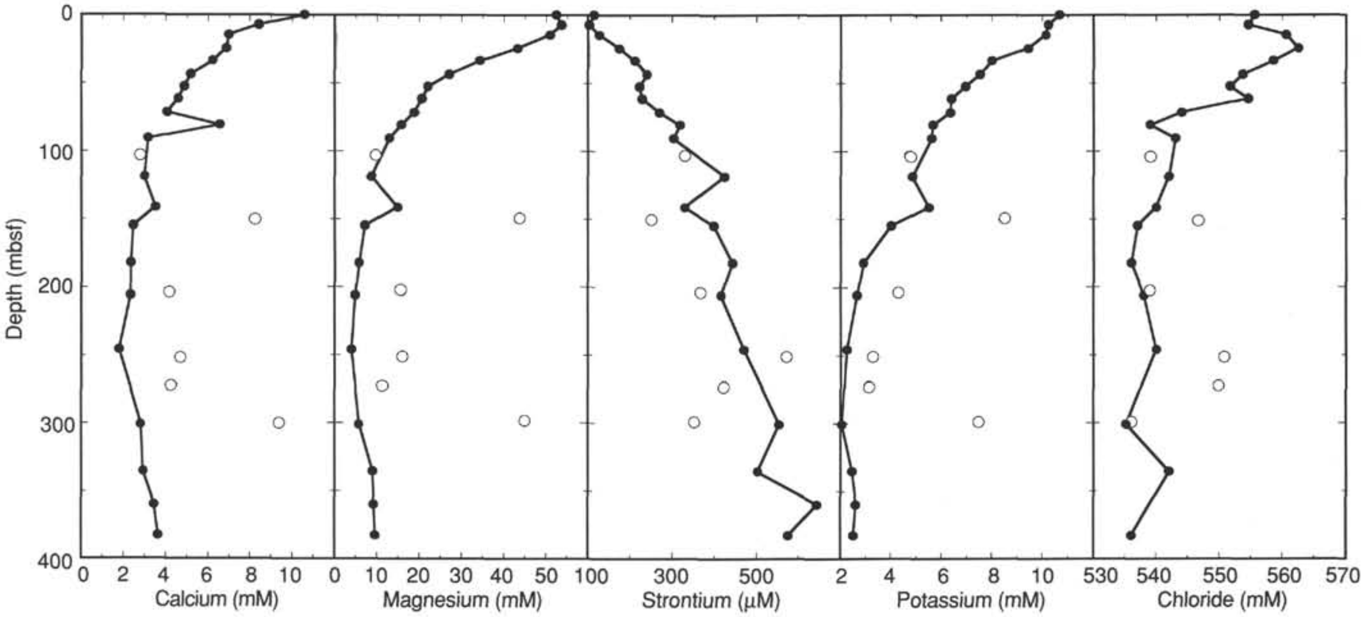

Figure 13. Calcium, magnesium, strontium, potassium, and chloride data as a function of depth for Site 820. Open circles indicate data from WSTP samples.

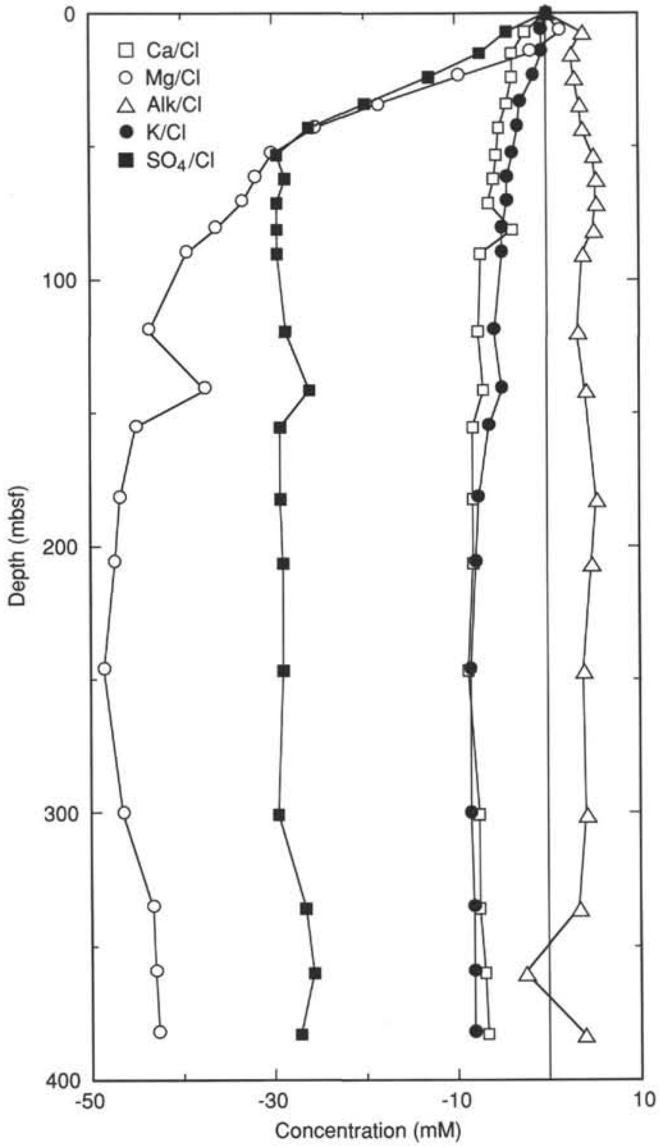

Figure 14. Concentrations of calcium, magnesium, alkalinity, potassium, and sulfate adjusted for surface-water salinity as a function of depth for Site 820.

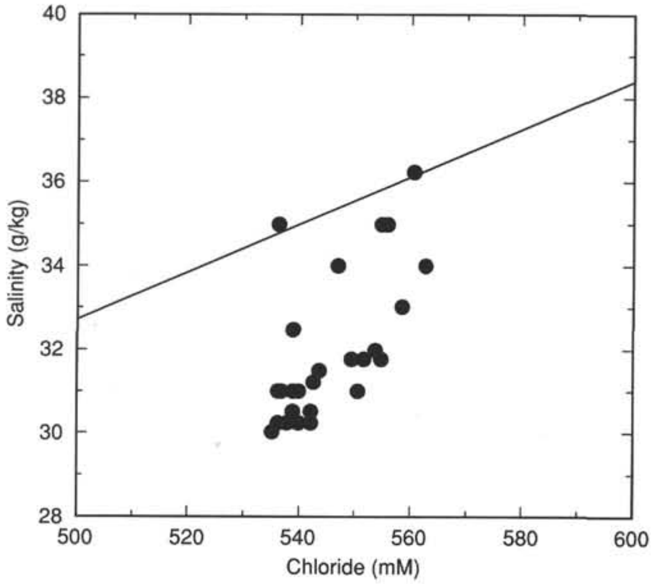

Figure 15. Concentrations of salinity vs. chloride for Site 820. Line in graph depicts a conservative relationship between salinity and chlorinity.

products of the reaction above, at Site 820 one would expect alkalinity values of approximately 60 mM, whereas the highest values measured are only 7.8 mM. The loss of alkalinity relative to expected values is a consequence of authigenic carbonate formation.

Concentrations of ammonia increase from a seawater value of 0 to 2111 μM at 71.6 mbsf (Fig. 16 and Table 2). Below this interval, values decrease to 1179 μM at 119 mbsf and then increase again to 2029 μM at 141.6 mbsf. As with sulfate, we think that these small peaks in the ammonia profile result from contamination by seawater. Below 141.6 mbsf, values decrease to 631 μM. At 360.4 mbsf, ammonia concentrations increase to 1618 μM and then decrease to 1015 μM at the bottom of the sampled interval. Increases in concentration of ammonia are related to sulfate reduction of sedimented organic matter. During sulfate reduction, the maximum amount of ammonia that can be produced if all of the sulfate is consumed is about 8000 μM, as can be seen from Equation 1. As the maximum value for concentrations of ammonia measured was 2358 μM at Site 820, ammonia may be undergoing ion exchange reactions with clay minerals. Evidence for this process is the maxima in magnesium concentrations near the top of the sampled section (Fig. 13 and Table 2), which may partly result from the release of magnesium from clays as ammonia is taken up.

In addition, 1 mole of phosphate should be produced for every 53 moles of sulfate consumed. Therefore, in these sediments, one would expect a maximum value of concentrations of phosphate (associated with remineralization of organic matter) of 55 μM. As the highest measured phosphate value was only 7 μM, a large amount of phosphate must be lost from pore fluids, possibly into clay or amorphous phosphate minerals.

Silica

Concentrations of silica increase from a seawater value of 3 to 190 μM at 7.45 mbsf (Fig. 17 and Table 2). Below this depth, silica concentrations remain nearly constant at 150 %M for the rest of the sampled interval. Concentrations of pore-water silica reflect the low contents of biogenic silica of the sediments, as shown by micropaleontological analysis.

Results From WSTP Samples

Because of the degree of induration of sediments at Site 820, we were unable to penetrate successfully these sediments using the WSTP to acquire representative water samples. As a result, all WSTP samples have been contaminated with seawater and do not accurately reflect variations in interstitial water chemistry shown by squeezed samples (Figs. 13, 16, and 17).

Carbonate Content and X-Ray Diffraction Data

Samples for X-ray diffraction (XRD) analyses were taken from interstitial water squeeze cakes and physical properties samples.

At Site 820, aragonite is present throughout the entire sampled section. Relative concentrations average 50% at the top of the section and decrease slightly downhole to 40% (Fig. 18 and Table 3). HMC is present in the top 170 mbsf, with concentrations as high as 20% (Fig. 18 and Table 3).

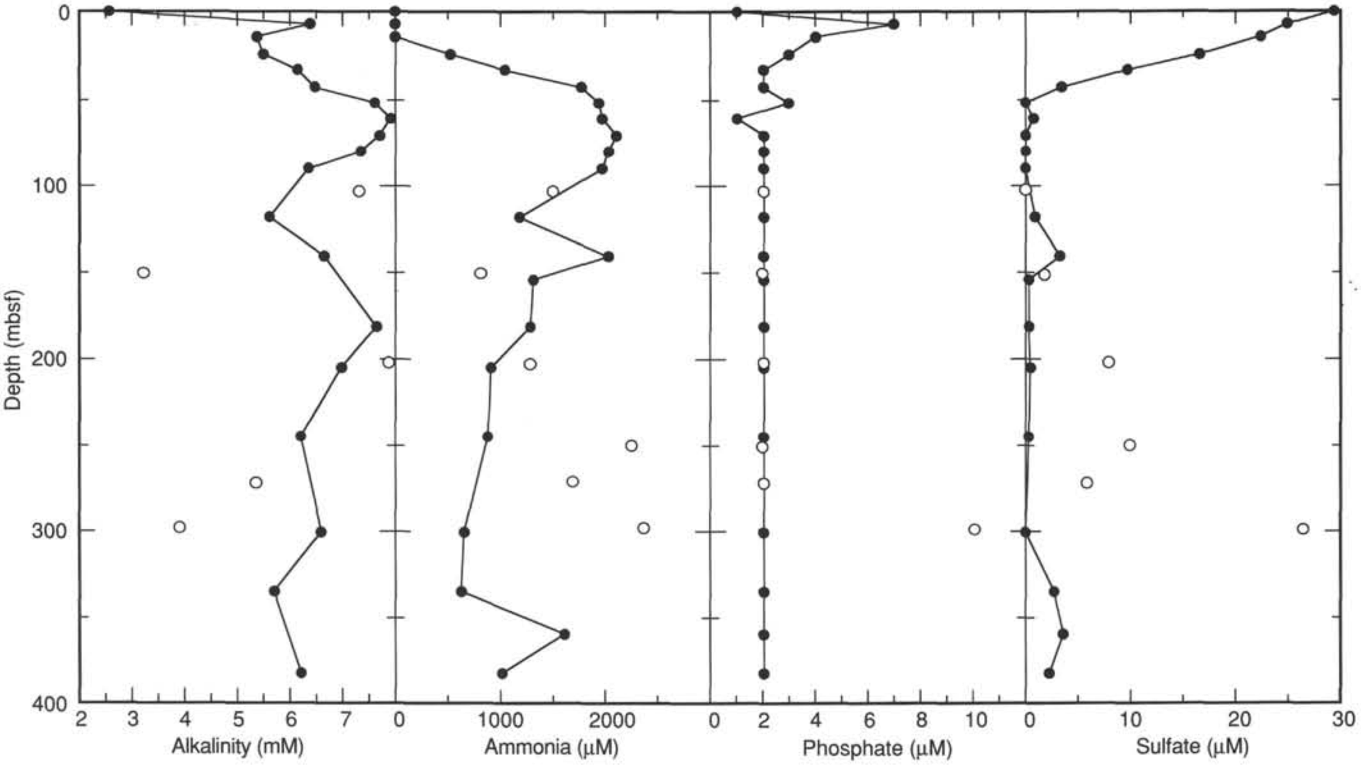

Figure 16. Alkalinity, ammonia, phosphate, and sulfate data as a function of depth for Site 820. Open circles depict WSTP data.

HMC disappears between 170 and 265 mbsf, then reappears at 265 mbsf and is present throughout the rest of the sampled section. Quartz is present in all samples at Site 820 and ranges from 4.9% to 26.1% (Fig. 18 and Table 3). Dolomite is present between 44.45 and 330.30 mbsf, with concentrations of 0.8% to 17.4% (Fig. 18 and Table 3). LMC is present in all samples, with variable concentrations of 18% to 60% (Fig. 18 and Table 3).

Contents of calcium carbonate are highly variable at Site 820, with values ranging from 28.3% to 88.1% (Fig. 19 and Table 4). Using a running average for every five points, one can see distinct trends of cyclic carbonate variations (Fig. 19). These variations most likely result from dilution of the carbonate fraction of the sediments.

ORGANIC GEOCHEMISTRY

In addition to safety monitoring for hydrocarbons, our main purpose for shipboard organic geochemistry studies at Site 820 was to assess the amount and origin of organic matter preserved in Pleistocene mixed sediments deposited in front of the present-day Great Barrier Reef. Our second purpose was to characterize the proportions of different light hydrocarbons generated in these sediments through biogenic or thermogenic decay of organic matter.

Samples

Forty-six samples were collected from Site 820 at 10-m intervals over a depth ranging from 4 to 398 mbsf. All sediments were analyzed for compositions of light hydrocarbons (C_1–C_6) using headspace analyses and for total nitrogen, sulfur, and carbon contents using an NA-1500 Carlo Erba NCS analyzer.

Volatile Hydrocarbons

Hydrocarbon gases (C_1–C_6) in sediments were analyzed as part of ODP's safety and pollution-prevention monitoring program using the headspace technique, the vacutainer technique (when gas pockets were observed in the core liner), the Carle gas chromatograph (for determining C_1–C_3 concentrations), and the NGA gas chromatograph (mainly for determining C_4–C_6 concentrations). The results of 46 headspace analyses and of three vacutainer analyses from Holes 820A and 820B are presented in Table 5. Figure 20 shows WSTP-temperature data from Sites 817 and 820 and the geothermal gradient used at Site 820 for interpreting the depth-related evolution of the C_1/C_2 ratio.

Sediments at Site 820 contain high concentrations of methane, but these represented no safety and/or pollution hazards: the evolution of the C_1/C_2 ratio with increasing depth and temperature indicated no anomalous trend (Fig. 21). C_1/C_2 values from headspace analyses ranged between 13,000 and 700.

Headspace-gas concentrations of methane (Fig. 22) were low in the first 40 mbsf (3–7 ppm), but increased sharply below 50 mbsf, at the bottom of the sulfate-reduction zone (see "Inorganic Geochemistry" section, this chapter). Methane was the main component below this depth. Concentrations reached a maximum value at a depth of 110 mbsf (75,000 ppm in Sample 133-820A-12H-6, 0–2 cm), decreased between 190 and 200 mbsf, reached a minimum value at a depth of 309 mbsf (1000 ppm in Sample 133-820B-34X-CC, 0–2 cm), and increased again below this depth. Propane and ethane appeared together at 62 mbsf (Fig. 22). Concentrations of these gases did not exceed 40 ppm and followed the trend of methane. Between 62 and 150 mbsf, concentrations of ethane were twice those of propane (C_2/C_3 = 2). Between 150 and 300 mbsf, the C_2/C_3 ratio = 1, and below 300 mbsf, propane concentrations exceeded the ethane (C_2/C_3 ratio < 1) and increased to 38 ppm at a depth of 397 mbsf (Sample 133-820B-44X-1, 148–150 cm).

The observed coincidence among low sulfate concentrations, high amounts of methane (>1000 ppm), and trace amounts of ethane and propane in sediments suggests a bacterial origin for methane (and ethane-propane?) section

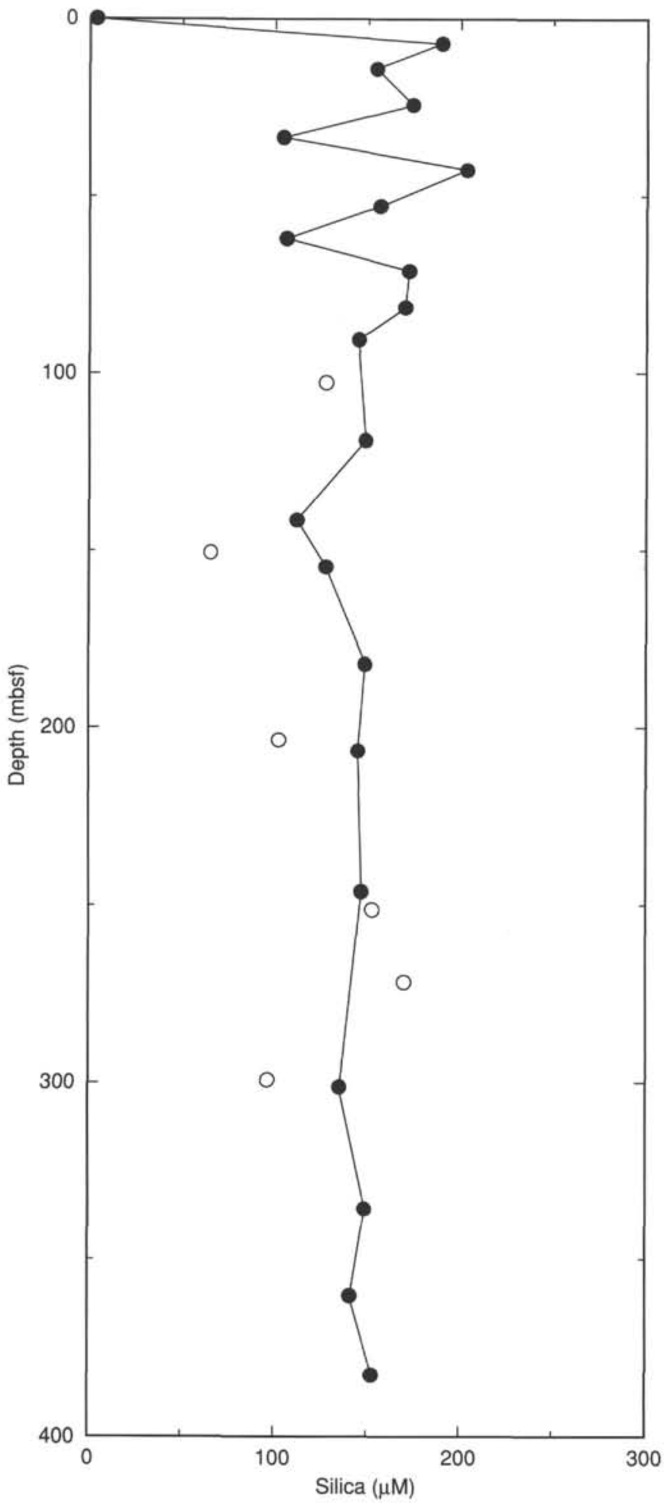

Figure 17. Concentrations of silica in interstitial water as a function of depth at Site 820. Open circles represent WSTP data.

between 50 and 190 mbsf (Figs. 22 and 23). Below 190 mbsf, two factors seem to indicate the beginning of mixing with thermogenic free-hydrocarbons:

1. A progressive increase of propane content and the decrease of both the C_2/C_3 and $C_1/(C_2+C_3)$ ratios at very shallow depths and low temperatures (Figs. 22 and 23).

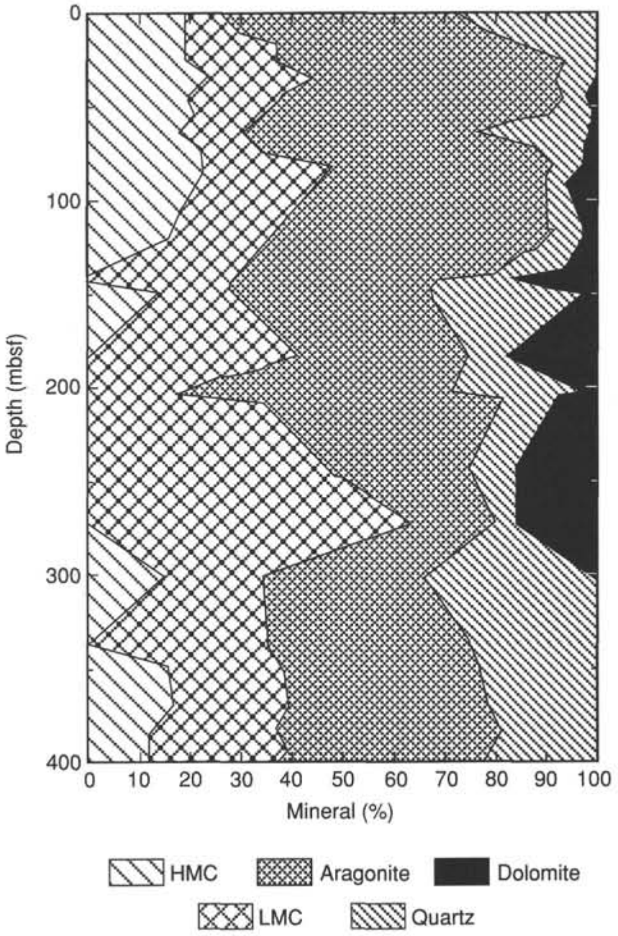

Figure 18. X-ray diffraction data for Site 820. We have assumed that the sediments are composed entirely of calcite, aragonite, quartz, and dolomite.

Table 3. X-ray diffraction data, Site 820.

Core, section, interval (cm)	Depth (mbsf)	Calcite (%)	Aragonite (%)	Quartz (%)	Dolomite (%)
133-820A-					
1H-4, 145–150	5.95	27.3	46.6	26.1	0
2H-5, 145–150	15.95	37.1	45.8	17.1	0
3H-5, 145–150	25.45	36.8	56.6	6.6	0
4H-5, 145–150	34.95	44.5	47.5	8	0
5H-5, 145–150	44.45	37.9	55.1	5.3	1.7
6H-5, 145–150	53.95	34.8	55.5	9.7	0
7H-5, 145–150	63.45	30.5	45	23.7	0.8
8H-5, 140–150	72.9	33.5	54.3	10.4	1.8
9H-5, 140–150	82.4	48.2	42.8	6.6	2.4
10H-5, 140–150	91.9	44.5	45.2	4.9	5.4
13H-5, 140–150	118.4	35.6	54.7	8.2	1.5
15H-5, 140–150	137.8	30.4	49.3	13.7	6.6
16V-1, 148–150	141.6	28.1	39.9	15.9	16.1
133-820B-					
17H-3, 140–150	155.1	28.2	38.5	32.2	1.1
20X-5, 140–150	182.2	41.7	33	7.9	17.4
21X-6, 140–150	194.5	16.5	54.7	27.6	1.2
22X-2, 140–150	201.2	33.3	47.6	11.4	7.7
23X-1, 140–150	206.3	46.7	28	9.7	15.6
27X-1, 140–150	246.2	63.5	16.6	4.9	15
30X-1, 140–150	271.8	34.4	31.1	34.5	0
36X-5, 140–150	335.9	35.3	39.5	25.2	0
39X-5, 140–150	361.9	38.1	38.7	23.2	0
41X-5, 140–150	371.5	39.3	39.4	21.3	0
42X-5, 148–150	381.1	37.4	43.6	19.1	0
43X-5, 140–150	390.9	37.8	44.7	17.6	0
44X-7, 0–7	405.0	40.5	37.1	22.4	0

2. A strong decrease of both C_1 content, the C_1/C_2 and $C_1/(C_2+C_3)$ ratios at depths of 310, 340–350, and 385 mbsf, and strong decreases in porosity and water contents (Fig. 24; see "Physical Properties" section, this chapter) of lithified bioclastic packstones observed in Subunits IIID and IIIE (see "Lithostratigraphy" section, this chapter).

Organic Carbon Contents

Total organic carbon (TOC) and total inorganic carbon contents together with concentrations of total nitrogen and sulfur recorded in Site 820 are presented in Table 6.

Amounts of organic carbon at Site 820 were low and did not exceed 0.45% TOC (Fig. 25); these varied with changes in lithology. We observed very low TOC values ($< 0.25\%$) in the sand-sized bioclastic wackestones/packstones, and we observed higher TOC values in the more clay-rich mudstones.

Total sulfur concentrations in the sediments (Fig. 25) were below detection limits of the NCS analyzer in Unit I. Values increased in Unit II and reached 0.15% to 20% in the more organic-rich mudstone horizons encountered in Subunits IIIC and IIID.

Total nitrogen concentrations in the sediments was low; average values ranged between 0.02% in the first 300 m and 0.04% below this depth (Fig. 25).

We observed intense short-term variations in distribution of the TOC/nitrogen ratios (Fig. 25). The type of organic matter preserved in Pleistocene sediments at Site 820 was a variable mixture of marine and terrigenous organic materials. As a consequence of low organic contents, we were unable to conduct detailed geochemical characterization of kerogen types using the Rock-Eval pyrolysis method, as originally planned. More detailed shore-based studies (elemental analysis and optical investigations of extracted kerogens) will permit characterization of short-term fluctuations in vertical distribution and preservation of the different components of organic matter in sediments encountered at Site 820.

PHYSICAL PROPERTIES

Physical properties analyzed in cores from this site include bulk density, *P*-wave velocity, and magnetic susceptibility of unsplit cores and *P*-wave velocity, electrical resistivity formation factor, shear strength, and index properties (including bulk density, grain density, water content, porosity, and void ratio) of split cores. The methods used are described in detail in the "Explanatory Notes" chapter (this volume).

Bulk Density

Bulk densities for Site 820 were determined by measuring volumes and mass of discrete core samples and from gamma-ray absorption of whole-round cores (Fig. 26 and Table 7). After an initial increase with depth in the upper 100 mbsf, density increases much more slowly with depth. This increase in density is primarily a function of decreasing porosity from increasing overburden with depth (see discussion of porosity below).

P-Wave Velocity

P-wave velocities were measured on whole-round cores using the multisensor track (MST) and on discrete core samples using the Hamilton Frame (Table 8 and Fig. 26). As indicated in Figure 27, velocity, to some extent, correlates with shear strength in that major low-velocity peaks correlate with low shear-strength peaks, while a general increase in velocity with depth parallels the increase of shear strength with depth.

Porosity

Porosity was one of the index properties determined from discrete core samples using mass balance and the pycnometer (Table 7). A graph of porosity vs. depth is shown in Figure 27. Similarly, the water content, derived from the same set of index-property measurements, is plotted in Figure 26. Also shown is a plot of water content vs. bulk density that indicates the expected relationship for a two-phase system, which can be modeled using a grain density of 2.76 g/cm^3 and a water density of 1.0245 g/cm^3.

Upon accumulating data from several sites, we began to recognize trends in porosity data. To find clues to the processes that led to development of these porosity-depth trends, one may use simple algebraic relationships between porosity and depth and compare these relationships among several sites. The processes governing compaction, such as development of lithostatic pressure, may have algebraic relationships to depth similar to the resulting porosity. In the case of porosity loss from increasing overburden, a fairly simple stress-strain relationship may exist between overburden pressure and porosity. Logarithmic plots often are useful for providing simple algebraic relationships, and the appearance of the raw data for Sites 819 and 820 suggests exponential relationships between depth and porosity.

Plots of porosity vs. depth for Site 817 in Figure 28A show that the general trend of porosity vs. depth at Site 817 can be well represented by a linear regression of porosity on depth or ln porosity on depth and that these data are not represented at all well by a linear regression of ln porosity on ln depth. By contrast, Figure 28B indicates that the porosity-depth trend at Site 819 is not at all well represented by a linear regression of porosity on depth, but is well represented by a linear regression of ln porosity on ln depth. Site 820 is intermediate between Sites 817 and 819 in that a linear regression of ln porosity on ln depth is marginally better at describing the data than either the linear regression of porosity on depth or ln porosity on depth (Fig. 28C). These general trends are summarized in Figure 24.

The linear regression of ln porosity on depth is of special significance in that the inverse of this function is of the form porosity $\phi = a\ \exp(-cz)$, where the constants, a and c, are determined by the regression of ln porosity on depth, z. This form is the normal compaction curve. For Site 820, $a = 0.45$ and $c = 0.001$, when z is measured in meters and fractional porosity ϕ is expressed as a fraction where $0 < \phi < 1$. When z is expressed in centimeters, $c = 10^{-5}$.

To see the significance of this form, we must consider expression of overburden stress or lithostatic pressure at depth, z, which is g × bulk density × depth, where g is the acceleration of gravity at Earth's surface: 980 cm/s^2. Because bulk density varies with depth, a general relationship for overburden pressure, P, is $P = g \times ([\text{bulk density}])\ dz = g \times k \times ([1-\phi]dz$, where ϕ is fractional porosity and k is grain density (2.76 g/cm^3). For $\phi = a \times \exp(-cz)$, $g \times k \times ((1-\phi)dz = g \times k \times [z + (a/c) \times \exp(-cz) - a/c]$. Our compaction curves then can be understood as the result of a loss of porosity directly proportional to lithostatic pressure.

This explains the general shape of our porosity-depth curve, but does not explain the fine structure of observed curves or why curves at Sites 819 and 820 are more similar to each other than to those from Site 817. For an explanation of this, we shall have to look at variations in composition of the material composing the stratigraphic section, as well as at the history of the lithostatic load at each site.

Electrical-Resistivity Formation Factor

We measured the formation factor in cores from Hole 820A (see Table 9 and Fig. 27. Qualitatively, we see the

Table 4. Carbonate data, Site 820.

Core, section interval (cm)	Depth (mbsf)	Sample code	Total carbon (%)	Inorganic carbon (%)	Organic carbon (%)	$CaCO_3$ (%)	Nitrogen (%)	Sulfur (%)	OrgC/N	OrgC/S
133-820A-										
1H-1, 102–104	1.02	PP		4.22		35.2				
1H-2, 102–104	2.52	PP		7.89		65.7				
1H-3, 102–104	4.02	PP	6.74	6.52	0.22	54.3	0.02		11.00	
1H-4, 102–104	5.52	PP		8.40		70.0				
1H-5, 62–65	6.62	PP		5.23		43.6				
2H-1, 21–23	7.41	PP		8.64		72.0				
2H-1, 102–105	8.22	PP		7.66		63.8				
2H-2, 20–23	8.90	PP		7.75		64.6				
2H-3, 102–105	11.22	PP		5.44		45.3				
2H-4, 102–105	12.72	PP		5.31		44.2				
2H-5, 17–19	13.37	PP		5.70		47.5				
2H-5, 145–150	14.65	XRD	7.12	6.82	0.30	56.8	0.03		10.00	
2H-6, 20–23	14.90	PP		7.29		60.7				
3H-1, 100–103	17.70	PP		9.58		79.8				
3H-2, 100–103	19.20	PP		9.22		76.8				
3H-3, 100–103	20.70	PP		8.15		67.9				
3H-4, 100–103	22.20	PP		9.08		75.6				
3H-5, 100–103	23.70	PP		8.18		68.1				
3H-5, 145–150	24.15	XRD	8.11	7.72	0.39	64.3	0.03		13.00	
3H-6, 100–103	25.20	PP		8.23		68.6				
4H-1, 100–103	27.20	PP		9.15		76.2				
4H-2, 100–103	28.70	PP		7.04		58.6				
4H-3, 100–103	30.20	PP		4.67		38.9				
4H-4, 100–103	31.70	PP		4.82		40.2				
4H-5, 100–103	33.20	PP		6.08		50.6				
4H-5, 140–150	33.60	XRD	9.39	9.10	0.29	75.8	0.02		14.00	
4H-6, 100–103	34.70	PP		8.15		67.9				
5H-1, 100–103	36.70	PP		9.67		80.6				
5H-2, 100–103	38.20	PP		9.49		79.1				
5H-3, 100–103	39.70	PP		8.80		73.3				
5H-4, 100–103	41.20	PP		8.83		73.6				
5H-5, 100–103	42.70	PP		9.17		76.4				
5H-5, 140–150	43.10	XRD	9.47	9.09	0.38	75.7	0.03		12.00	
5H-6, 100–103	44.20	PP		8.46		70.5				
6H-1, 100–103	46.20	PP		6.79		56.6				
6H-2, 100–103	47.70	PP		6.57		54.7				
6H-3, 100–103	49.20	PP		6.50		54.1				
6H-4, 100–103	50.70	PP		5.80		48.3				
6H-5, 100–103	52.20	PP		9.44		78.6				
6H-5, 140–150	52.60	XRD	9.63	9.32	0.31	77.6	0.01		31.00	
6H-6, 100–103	53.70	PP		7.78		64.8				
7H-1, 100–103	55.70	PP		7.91		65.9				
7H-2, 100–103	57.20	PP		6.98		58.1				
7H-3, 100–103	58.70	PP		6.50		54.1				
7H-4, 100–103	60.20	PP		6.91		57.6				
7H-5, 100–103	61.70	PP		4.96		41.3				
7H-5, 140–150	62.10	XRD	4.75	4.33	0.42	36.1	0.03		14.00	
7H-6, 100–103	63.20	PP		3.66		30.5				
8H-1, 118–120	65.38	PP		9.26		77.1				
8H-1, 140–150	65.60	XRD	7.89	7.71	0.18	64.2	0.02		9.00	
8H-2, 118–120	66.88	PP		6.71		55.9				
8H-3, 118–120	68.38	PP		8.80		73.3				
8H-4, 118–120	69.88	PP		8.62		71.8				
8H-5, 118–120	71.38	PP		7.98		66.5				
8H-6, 118–120	72.88	PP		6.11		50.9				
9H-1, 100–103	74.70	PP		8.03		66.9				
9H-2, 100–103	76.20	PP		6.70		55.8				
9H-3, 100–103	77.70	PP		5.85		48.7				
9H-4, 100–103	79.20	PP		10.39		86.5				
9H-5, 100–103	80.70	PP		9.43		78.6				
9H-5, 140–150	81.10	XRD	8.80	8.61	0.19	71.7	0.02		9.50	
9H-6, 100–103	82.20	PP		6.97		58.1				
10H-1, 101–104	84.21	PP		10.31		85.9				
10H-2, 101–104	85.71	PP		9.94		82.8				
10H-3, 101–104	87.21	PP		9.08		75.6				
10H-4, 101–104	88.71	PP		5.56		46.3				
10H-5, 101–104	90.21	PP		9.29		77.4				
10H-5, 140–150	90.60	XRD	9.40	9.31	0.09	77.6	0.01		9.00	
10H-6, 101–104	91.71	PP		9.33		77.7				
11H-1, 100–103	93.70	PP		7.09		59.1				
11H-2, 100–103	95.20	PP		7.80		65.0				
11H-3, 100–103	96.70	PP	9.20	8.75	0.45	72.9	0.02		22.00	
11H-4, 100–103	98.20	PP		8.92		74.3				
11H-5, 100–103	99.70	PP		8.85		73.7				

Table 4 (continued).

Core, section interval (cm)	Depth (mbsf)	Sample code	Total carbon (%)	Inorganic carbon (%)	Organic carbon (%)	$CaCO_3$ (%)	Nitrogen (%)	Sulfur (%)	OrgC/N	OrgC/S
11H-6, 100–103	101.20	PP		8.73		72.7				
12H-1, 100–103	103.20	PP		9.24		77.0				
12H-2, 100–103	104.70	PP		9.93		82.7				
12H-3, 100–103	106.20	PP	9.78	9.40	0.38	78.3	0.02		19.00	
12H-4, 100–103	107.70	PP		9.50		79.1				
12H-5, 100–103	109.20	PP		9.57		79.7				
12H-6, 100–103	110.70	PP		8.97		74.7				
13H-1, 100–103	112.70	PP		8.96		74.6				
13H-2, 100–103	114.20	PP		9.42		78.5				
13H-3, 100–103	115.70	PP		9.28		77.3				
13H-4, 100–103	117.20	PP		8.30		69.1				
13H-5, 100–103	118.70	PP		7.15		59.6				
13H-5, 140–150	119.10	XRD	8.79	8.46	0.33	70.5	0.02		16.00	
13H-6, 100–103	120.20	PP		8.90		74.1				
14H-1, 100–103	122.20	PP		9.22		76.8				
14H-1, 140–150	122.60	XRD	4.55	4.14	0.41	34.5	0.03		13.00	
820B-14H-1, 76–79	122.96	PP		7.75		64.6				
14H-2, 76–79	124.46	PP		9.40		78.3				
14H-3, 76–79	125.96	PP		9.36		78.0				
14H-4, 76–79	127.46	PP		8.94		74.5				
14H-5, 76–79	128.96	PP		8.75		72.9				
14H-6, 76–79	130.46	PP		8.75		72.9				
820A-15H-1, 100–103	131.70	PP		8.85		73.7				
820B-15H-1, 57–60	132.27	PP		8.59		71.6				
820A-15H-2, 100–103	133.20	PP		8.68		72.3				
820B-15H-2, 57–60	133.77	PP		8.54		71.1				
820A-15H-3, 100–103	134.70	PP		8.60		71.6				
820B-15H-3, 57–60	135.27	PP	9.97	9.81	0.16	81.7	0.01		16.00	
820A-15H-4, 100–103	136.20	PP		8.29		69.1				
820B-15H-4, 57–60	136.77	PP		7.62		63.5				
820A-15H-5, 100–103	137.70	PP		9.66		80.5				
15H-5, 140–150	138.10	XRD	8.24	8.07	0.17	67.2	0.01	0.03	17.00	5.60
820B-15H-5, 57–60	138.27	PP		7.36		61.3				
820A-15H-6, 100–103	139.20	PP		6.41		53.4				
820B-15H-6, 57–60	139.77	PP		7.27		60.6				
820A-16V-1, 100–103	141.20	PP		7.29		60.7				
16V-1, 140–150	141.60	XRD	7.34	7.13	0.21	59.4	0.02		10.0	
133-820B-										
16H-1, 57–60	141.77	PP	7.83	7.46	0.37	62.1	0.01	0.06	37.00	6.10
16H-2, 57–60	143.27	PP		4.58		38.2				
17H-1, 33–36	151.03	PP		6.24		52.0				
17H-2, 33–36	152.53	PP		5.67		47.2				
17H-3, 33–36	154.03	PP		4.85		40.4				
17H-3, 140–150	155.10	XRD	4.83	4.58	0.25	38.2	0.03	0.06	8.30	4.10
17H-4, 33–36	155.53	PP		4.42		36.8				
18X-1, 54–56	160.74	PP		5.80		48.3				
18X-2, 54–56	162.24	PP		5.39		44.9				
18X-3, 54–56	163.74	PP	6.74	6.60	0.14	55.0	0.03	0.04	4.60	3.50
18X-4, 54–56	165.24	PP		7.77		64.7				
19X-1, 90–93	166.10	PP		9.72		81.0				
18X-5, 54–56	166.74	PP		9.19		76.6				
19X-2, 90–93	167.60	PP		9.87		82.2				
18X-6, 54–56	168.24	PP		7.31		60.9				
19X-3, 90–93	169.10	PP	9.10	8.89	0.21	74.1	0.01	0.07	21.00	3.00
19X-4, 90–93	170.60	PP		9.40		78.3				
19X-5, 90–93	172.10	PP		9.08		75.6				
19X-6, 90–93	173.60	PP		8.48		70.6				
20X-1, 90–93	175.70	PP		5.02		41.8				
20X-2, 90–93	177.20	PP		4.47		37.2				
20X-3, 90–93	178.70	PP		5.31		44.2				
20X-4, 90–93	180.20	PP		9.08		75.6				
20X-5, 90–93	181.70	PP		9.13		76.1				
20X-5, 140–150	182.20	XRD	9.50	9.14	0.36	76.1	0.02		18.00	
20X-6, 90–93	183.20	PP		9.23		76.9				
21X-1, 90–92	185.00	PP		8.72		72.6				
21X-2, 90–92	186.50	PP		8.54		71.1				
21X-3, 90–92	188.00	PP	8.71	8.47	0.24	70.6	0.02	0.02	12.00	12.00
21X-4, 90–92	189.50	PP		7.33		61.1				
21X-5, 90–93	191.00	PP		6.10		50.8				
21X-6, 90–93	192.50	PP		5.55		46.2				
22X-1, 90–93	194.60	PP		4.02		33.5				
22X-2, 90–93	196.10	PP		3.68		30.7				
22X-3, 90–93	197.60	PP		3.40		28.3				
22X-4, 90–93	199.10	PP		3.51		29.2				
22X-5, 90–93	200.60	PP		3.04		25.3				

Table 4 (continued).

Core, section interval (cm)	Depth (mbsf)	Sample code	Total carbon (%)	Inorganic carbon (%)	Organic carbon (%)	$CaCO_3$ (%)	Nitrogen (%)	Sulfur (%)	OrgC/N	OrgC/S
22X-6, 0–2	201.20	XRD	3.60	3.39	0.21	28.2	0.03	0.04	7.00	5.20
22X-6, 90–93	202.10	PP		3.57		29.7				
23X-1, 90–93	204.30	PP		7.21		60.1				
23X-2, 90–93	205.80	PP		6.51		54.2				
23X-2, 140–150	206.30	XRD	7.31	7.11	0.20	59.2	0.01		20.00	
23X-3, 90–93	207.30	PP		7.41		61.7				
23X-4, 90–93	208.80	PP		7.93		66.1				
23X-5, 90–93	210.30	PP		9.22		76.8				
23X-6, 90–93	211.70	PP		9.43		78.6				
24X-1, 90–93	213.70	PP		9.17		76.4				
24X-2, 90–93	215.20	PP		9.28		77.3				
24X-3, 90–93	216.70	PP	9.48	9.14	0.34	76.1	0.02		17.00	
24X-4, 90–93	218.20	PP		8.94		74.5				
24X-5, 90–93	219.70	PP		8.86		73.8				
24X-6, 90–93	221.20	PP		8.66		72.1				
25X-1, 90–93	223.40	PP		9.25		77.1				
25X-2, 90–93	224.90	PP		8.64		72.0				
25X-3, 90–93	226.40	PP	9.03	8.74	0.29	72.8	0.01		29.00	
26X-1, 90–93	233.00	PP	6.53	6.39	0.14	53.2	0.03	0.05	4.60	2.80
27X-2, 40–43	243.70	PP		8.64		72.0				
27X-3, 40–43	245.20	PP		9.85		82.1				
27X-3, 140–150	246.20	XRD	8.49	8.25	0.24	68.7	0.01		24.00	
27X-4, 40–43	246.70	PP		8.35		69.6				
27X-5, 40–43	248.20	PP		8.50		70.8				
28X-1, 10–13	251.20	PP		6.92		57.6				
28X-2, 10–13	252.70	PP		6.15		51.2				
28X-3, 10–13	254.20	PP	7.43	7.40	0.03	61.6	0.02	0.06	1.00	0.50
28X-4, 10–13	255.70	PP		6.90		57.5				
28X-5, 10–13	257.20	PP		7.24		60.3				
30X-1, 97–100	271.37	PP		8.02		66.8				
30X-1, 140–150	271.80	XRD	9.82	9.51	0.31	79.2	0.02	0.02	15.00	15.00
30X-2, 55–58	272.45	PP		7.34		61.1				
32X-2, 92–95	292.12	PP	8.03	7.67	0.36	63.9	0.02	0.17	18.00	2.10
33X-1, 90–93	300.30	PP	5.11	4.96	0.15	41.3	0.04	0.20	3.70	0.75
33X-1, 140–150	300.80	XRD		4.73		39.4				
33X-2, 90–93	301.80	PP		4.17		34.7				
33X-3, 90–93	303.30	PP		5.01		41.7				
33X-4, 90–93	304.80	PP		4.73		39.4				
33X-5, 90–93	306.30	PP		3.58		29.8				
34X-CC, 10–13	309.54	PP	5.41	5.15	0.26	42.9	0.05	0.09	5.20	2.90
36X-1, 9–11	328.59	PP		8.31		69.2				
36X-2, 25–27	330.25	PP		7.90		65.8				
36X-3, 25–27	331.75	PP		7.82		65.1				
36X-4, 25–27	333.25	PP		7.07		58.9				
36X-5, 25–27	334.75	PP		6.45		53.7				
36X-5, 140–150	335.90	XRD	6.79	6.56	0.23	54.6	0.03	0.06	7.60	3.80
36X-6, 25–27	336.25	PP		6.40		53.3				
37X-1, 16–19	338.36	PP		3.99		33.2				
37X-2, 16–19	339.86	PP		3.62		30.2				
37X-3, 16–19	341.36	PP	2.96	2.73	0.23	22.7	0.06	0.21	3.80	1.10
37X-4, 16–19	342.86	PP		3.57		29.7				
38X-1, 12–15	348.02	PP		3.25		27.1				
38X-2, 13–16	349.53	PP		4.77		39.7				
38X-3, 13–16	351.03	PP	5.05	4.69	0.36	39.1	0.05		7.20	
38X-4, 13–16	352.53	PP		4.44		37.0				
39X-1, 15–18	357.65	PP		4.57		38.1				
39X-2, 9–12	359.09	PP		7.75		64.6				
39X-3, 12–15	360.62	PP	7.15	7.01	0.14	58.4	0.04	0.13	3.50	1.10
40X-1, 23–25	362.93	PP		10.58		88.1				
40X-2, 23–25	364.43	PP		9.07		75.6				
40X-3, 23–25	365.93	PP	7.86	7.72	0.14	64.3	0.05	0.13	2.80	1.10
41X-1, 12–15	367.22	PP		9.32		77.6				
41X-2, 12–15	368.72	PP		8.94		74.5				
41X-3, 12–15	370.22	PP	9.14	8.89	0.25	74.1	0.02	0.02	12.00	12.00
41X-4, 12–15	371.72	PP		9.44		78.6				
41X-5, 12–15	373.22	PP		8.48		70.6				
42X-1, 11–13	376.81	PP		8.28		69.0				
42X-2, 11–13	378.31	PP		8.48		70.6				
42X-3, 11–13	379.81	PP	9.05	8.91	0.14	74.2	0.03	0.08	4.60	1.70
42X-4, 11–13	381.31	PP		8.44		70.3				
42X-5, 11–13	382.81	PP		7.82		65.1				
44X-1, 33–34	396.33	PP		6.64		55.3				
44X-2, 33–34	397.83	PP	8.18	7.87	0.31	65.6	0.03	0.01	10.00	31.00

XRD = X-ray diffraction; PP = physical properties.

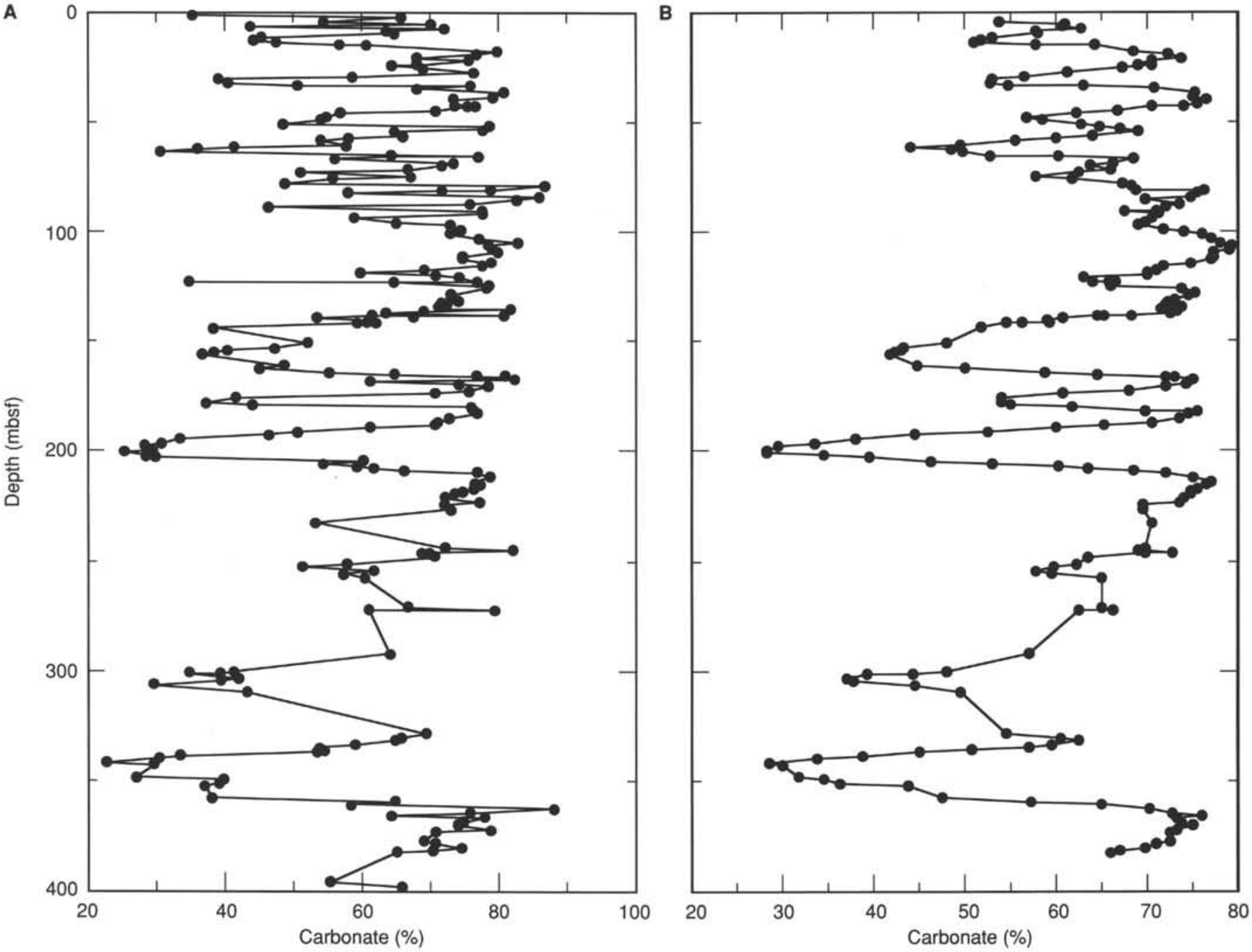

Figure 19. Carbonate data for Site 820 as a function of depth. **A.** Raw data. **B.** Smoothed data.

expected inverse relationship between porosity and formation factor.

Shear Strength

We measured shear strength in the upper section of Hole 820A (Table 10 and Fig. 27). One might expect for shear strength to be inversely proportional to porosity and, in general, this is what one sees; however, local exceptions exist, with some local peaks in shear strength that coincide with peaks in porosity.

Thermal Conductivity, Temperature, and Heat Flow

In Hole 820B, we obtained five measurements of temperature in the hole using the Barnes-Uyeda temperature probe, a measure of bottom-water temperature using an expendable bathythermograph (15.9°C), and measurements of thermal conductivity in the cores (see Table 11 and Figs. 26 and 29). We failed to measure conductivity between two of our temperature measurements because of gas in the cores. As expected, we can see an inverse relationship between thermal conductivities in the sediments and water contents (Fig. 26).

Thermal conductivity times vertical temperature gradients equals the heat flow with heat being transported primarily by conduction. For steady-state conduction, the heat flow measured at different depths should be the same. Our data permit us to calculate heat flow over four different intervals (see Fig. 30). Taking our data at face value, we have a positive heat flow of approximately 2.7 W/m^2 between 0 and 103 mbsf, a positive heat flow of only 0.7 W/m^2 over the interval from 103 to 151 mbsf, and a negative heat flow of -4.4 W/m^2 from 251 to 299 mbsf. A negative heat flow means that heat is traveling downward. This pattern of heat flow indicates either nonsteady-state or horizontal advection of significant heat in depths ranging from 150 to 250 mbsf.

DOWNHOLE MEASUREMENTS

Reliability of Logs

Hole size is the most important control of accuracy of logs from Leg 133, and hole size at Hole 820B was relatively uniform. Three types of caliper log were obtained: (1) an apparent caliper calculated from the sonic log (see "Explanatory Notes" chapter, this volume), (2) a caliper from the mechanical caliper device (MCD), and (3) a two-axis caliper (Fig. 31) from the FMS. The lithodensity tool caliper did not operate at this site. The FMS caliper is much more reliable than either sonic of MCD calipers. Based on correlation of

Table 5. Volatile hydrocarbon data from headspace and vacutainer analyses at Site 820.

Core, section, interval (cm)	Depth (mbsf)	Sample	Volume (mL)	Gas chromato.	C_1 (ppm)	C_2 (ppm)	C_3 (ppm)	C_1/C_2	C_2/C_3	$C_1/(C_2+C_3)$
133-820A-										
1H-4, 145–146	5.95	HS	5	CAR132	7	0	0			
2H-5, 145–146	14.65	HS	5	CAR132	5	0	0			
3H-5, 145–146	24.15	HS	5	CAR132	3	0	0			
4H-5, 145–146	33.65	HS	5	CAR132	3	0	0			
5H-5, 145–146	43.15	HS	5	CAR132	49	0	0			
6H-5, 145–146	52.65	HS	5	CAR132	4,271	0	0			
7H-5, 140–141	62.1	HS	5	CAR132	9,265	3	1	3,088	3.0	2316
8H-5, 149–150	71.69	HS	5	CAR132	37,926	7	2	5,418	3.5	4214
9H-5, 140–141	81.1	HS	5	CAR132	16,170	4	2	4,042	2.0	2695
10H-5, 149–150	90.69	HS	5	CAR132	64,134	14	6	4,581	2.3	3207
11H-5, 0–2	98.7	HS	5	CAR132	74,378	18	9	4,132	2.0	2755
12H-6, 0–2	109.7	HS	5	CAR132	74,611	21	10	3,553	2.1	2407
13H-5, 149–150	119.19	HS	5	CAR132	58,740	14	7	4,196	2.0	2797
14H-3, 0–2	123.75	HS	5	CAR132	9,506	4	3	2,376	1.3	1358
15H-5, 148–150	138.18	HS	5	CAR132	9,337	3	2	3,112	1.5	1867
16V-1, 140–141	141.6	HS	5	CAR132	12,833	1	6	12,833	0.2	1833
133-820B-										
14H-6, 0–2	129.7	HS	5	CAR132	66,075	13	8	5,082	1.6	3146
15H-5, 0–2	137.7	HS	5	CAR132	65,106	14	5	4,650	2.8	3427
16H-5, 0–2	147.2	HS	5	CAR132	31,729	6	3	5,288	2.0	3525
17H-3, 149–150	155.19	HS	5	CAR132	33,953	9	8	3,773	1.1	1997
18X-6, 0–2	167.7	HS	5	CAR132	68,586	18	12	3,810	1.5	2286
19X-5, 149–150	172.69	HS	5	CAR132	43,488	9	6	4,832	1.5	2899
20X-5, 140–141	182.2	HS	5	CAR132	62,141	10	6	6,214	1.7	3884
21X-6, 0–2	191.6	HS	5	CAR132	34,414	9	8	3,824	1.1	2024
22X-6, 0–2	201.2	HS	5	CAR132	10,053	6	7	1,675	0.9	773
23X-2, 140–142	206.3	HS	5	CAR132	8,926	4	4	2,231	1.0	1116
24X-6, 0–2	220.3	HS	5	CAR132	9,593	5	6	1,919	0.8	872
25X-2, 149–150	225.49	HS	5	CAR132	8,087	5	7	1,617	0.7	674
26X-1, 149–150	233.59	HS	5	CAR132	9,780	4	4	2,445	1.0	1222
27X-3, 149–150	246.29	HS	5	CAR132	5,906	2	3	2,953	0.7	1181
29X-3, 0–1	263.8	HS	5	CAR132	3,814	2	2	1,907	1.0	953
30X-1, 140–141	271.8	HS	5	CAR132	4,337	3	4	1,446	0.8	620
32X-1, 149–150	291.19	HS	5	CAR132	9,900	4	4	2,475	1.0	1237
33X-1, 149–150	300.89	HS	5	CAR132	2,445	2	4	1,222	0.5	407
34X-CC, 0–1	309.44	HS	5	CAR132	964	1	2	964	0.5	321
35X-2, 149–150	321.79	HS	5	CAR132	8,856	4	6	2,214	0.7	885
36X-5, 149–150	335.99	HS	5	CAR132	8,360	5	9	1,672	0.6	597
37X-2, 149–150	341.19	HS	5	CAR132	2,093	3	9	698	0.3	174
38X-2, 149–150	350.89	HS	5	CAR132	3,373	3	8	1,124	0.4	307
39X-2, 149–150	360.49	HS	5	CAR132	30,048	9	13	3,339	0.7	1366
40X-2, 0–2	364.2	HS	5	CAR132	8,004	4	9	2,001	0.4	616
41X-2, 148–150	370.08	HS	5	CAR132	30,748	9	15	3,416	0.6	1281
42X-5, 0–1	382.7	HS	5	CAR132	50,574	14	22	3,612	0.6	1405
43X-CC, 0–2	386.4	HS	5	CAR132	8,763	8	22	1,095	0.4	292
44X-1, 148–150	397.48	HS	5	CAR132	28,137	15	38	1,875	0.4	531
17H-2, 73–75	152.93	VAC	5	CAR132	177,000	56	26	3,161	2.2	2158
24X-2, 120–130	215.5	VAC	5	CAR132	86,034	20	13	4,301	1.5	2607
27X-4, 120–125	247.5	VAC	5	CAR132	105,670	30	19	3,522	1.6	2156

HS = headspace sample; VAC = vacutainer sample.

largest caliper values with anomalously low density values (Fig. 31), we suspect that occasional lowest-density portions of the lithodensity run are unreliable because pad contact against the borehole wall was insufficient. As discussed later, this pattern implies that porosity and Archie component (*m*) calculations will be in error in these zones (Fig. 32). Most other logs do not require pad contact and thus are relatively insensitive to changes in borehole size. Three minor exceptions are the gamma-ray, resistivity, and neutron porosity logs, which probably will be changed slightly by post-cruise borehole corrections.

As is often the case with ODP holes, the initial sonic logs from Hole 820B exhibited a few zones in which cycle-skipping caused unreliable swings in apparent velocity. Reprocessing (see "Explanatory Notes" chapter, this volume) seems to have removed all unreliable data, and we consider the reprocessed velocity log in Figure 31 to be of very good quality. For the short interval from 371.0 to 386.4 mbsf at the bottom of the hole, resistivity logs (but not sonic logs) are available because the resistivity tool is much lower on the tool string. A pseudosonic log was generated and used for this interval, based on regression of sonic transit time on logarithm of shallow resistivity for the overlying interval from 319.3 to 370.8 mbsf ($R = -0.94$).

The spectral gamma-ray tool is the only tool in the seismic stratigraphic combination that can provide useful formation data through pipe. On the geochemical tool string, useful through-pipe data were obtained by the spectral gamma-ray, aluminum clay, and gamma spectroscopy tools. At Hole 820B, through-pipe spectral gamma-ray logs were obtained for the interval from 0 to 69.6 mbsf during one run of the seismic stratigraphic combination and two runs of the geochemical combination; geochemical runs have a higher signal-to-noise ratio for spectral gamma-ray logs because of a slower logging speed. Through-pipe aluminum and gamma-ray spectroscopy logs were obtained from two passes of the geochemical string, while pipe was moved 5 m between the two passes to permit

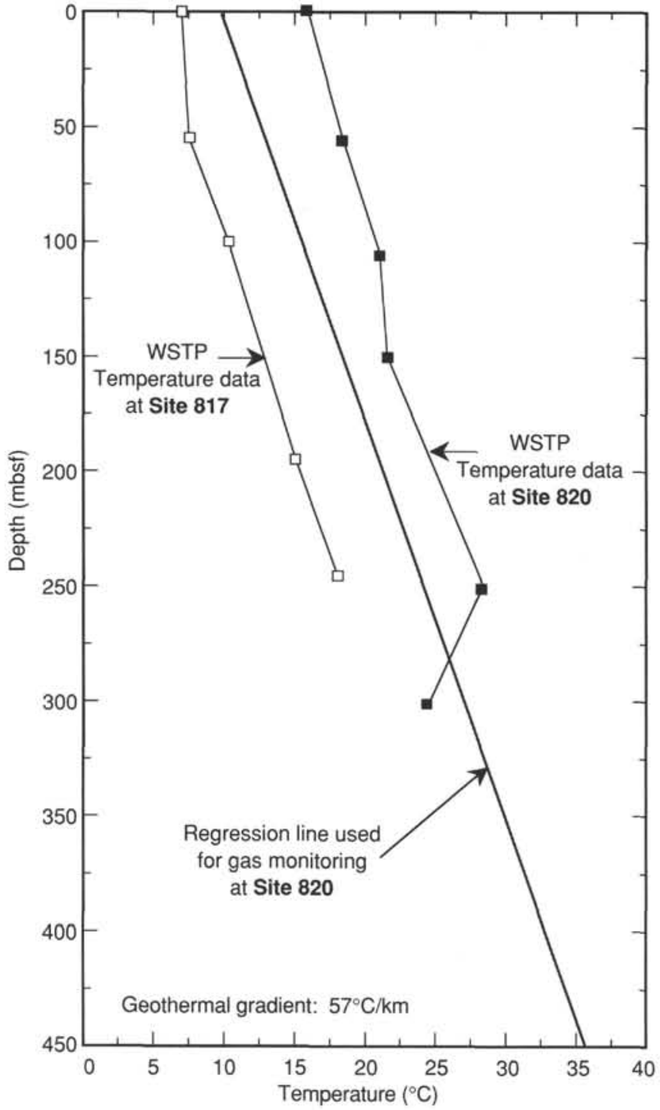

Figure 20. WSTP-temperature data from Sites 817 and 820, and geothermal gradient used at Site 820.

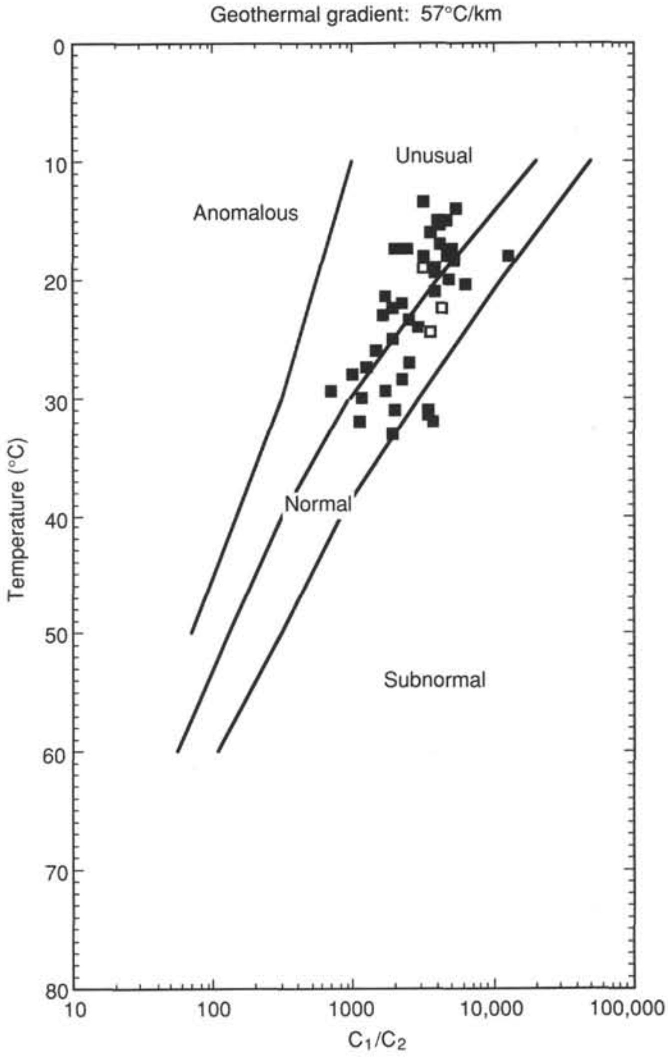

Figure 21. Distribution of C_1/C_2 ratio with temperature at Site 820 (black points = headspace samples; white points = vacutainer samples). This diagram was compiled for ODP's shipboard safety and pollution-prevention monitoring program.

discrimination of changes in pipe thickness from those in the formation. Subjective examination of through-pipe geochemical logs for Hole 820B indicates that these did detect geochemical changes in the formation. However, we have not yet corrected for pipe size in any of these logs.

When we repeated a pass of the geochemical combination, we also obtained a short interval of open-hole logs. As expected, second runs of spectral gamma-ray and aluminum logs were offset by irradiation effects in zones where the tool string paused or slowed for calibration before we began the second run. In general, however, the two passes exhibit a high correlation of log character (Fig. 33). Exceptions are the potassium log, which appears to have fair-to-poor replicability, and the small-scale (<2 m) character on most of the logs.

We noted electronic tool problems throughout the logging with the FMS. We decided to log anyway, and the problem was later traced to three loose components in the electronic cartridge of the tool. One obvious adverse effect of the problem was that we lost 50 cm of data every 4.4 m; the rest of the data are acceptable, particularly those from the second pass. Post-cruise reprocessing will be required to assess whether this remaining portion of the log has been degraded in any way.

Velocity, Resistivity, and Density Relationships

Velocity, resistivity, and density strongly correlate throughout almost all the logged interval at Hole 820B (Figs. 31 and 34). This correlation was created because of porosity dominance in all three logs. Two additional porosity logs were obtained using the geochemical tool string (Fig. 34): neutron and hydrogen. An uncalibrated neutron porosity log was generated by the aluminum clay tool; because the californium source is much stronger than the americium/beryllium sources used in conventional neutron porosity tools, apparent porosities are much higher and are uncalibrated. Apparent neutron porosity values at Hole 820B ranged from 120% to 170% (fractional "porosities" of 1.2–1.7), but variations in relative porosity are probably reliable. The gamma-ray spectrometry tool (GST) detects variations in amounts of hydrogen relative to several other elements (see "Explanatory Notes" chapter, this volume); again, values are not calibrated, but are potentially useful as a measure of relativity. We detected hydrogen from both the neutron porosities and GST hydrogen counts, without distinguishing whether it was as free water in pores or bound

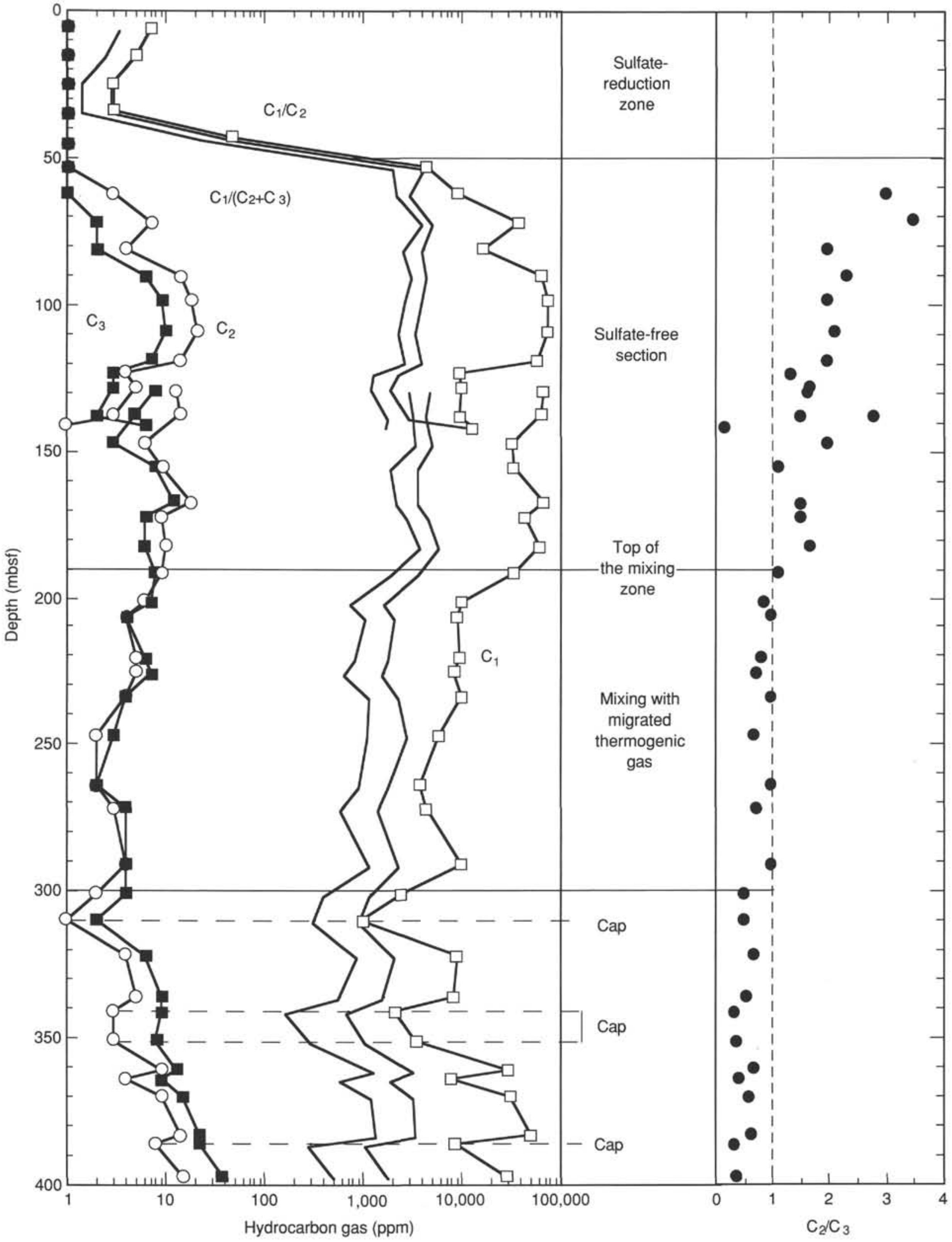

Figure 22. Distribution with depth of amounts of hydrocarbon gas in headspace samples at Site 820 showing evolution of C_1/C_2, C_2/C_3, and $C_1/(C_2 + C_3)$ ratios.

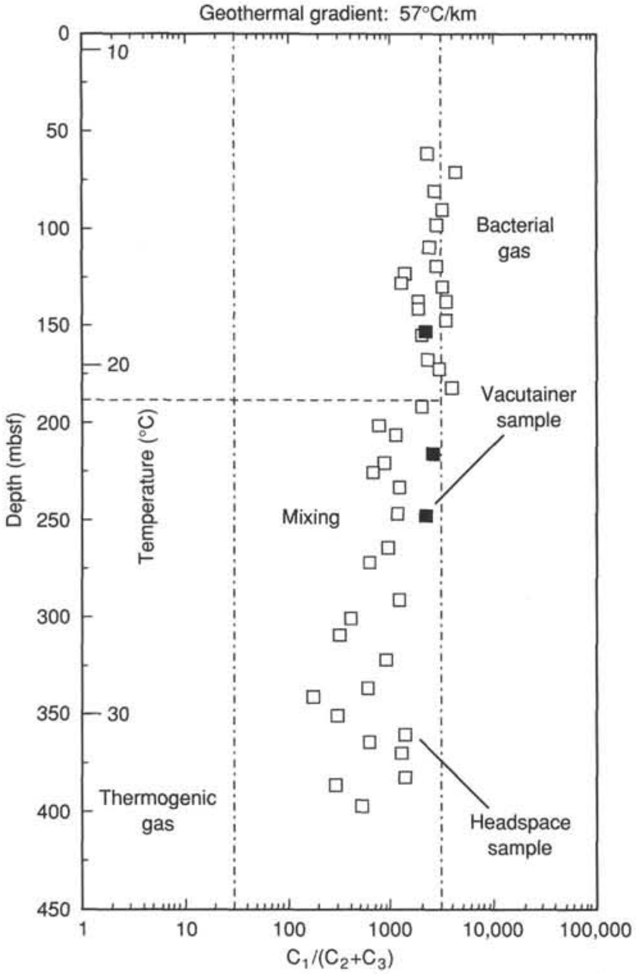

Figure 23. Evolution with depth and temperature of the $C_1/(C_2 + C_3)$ ratio at Site 820.

water in clay minerals. Thus, these two logs can overestimate porosity in clay-rich intervals. All five porosity-sensitive logs in Figure 34, although uncalibrated as to absolute porosity, exhibit strong interlog correlations and, consequently, are considered to be good indicators of variations in relative porosity at Site 820.

Changes in velocity and density with depth (Fig. 31) generally follow a gradual compaction profile, suggesting that mechanical compaction dominates diagenesis for controlling porosity at this site. Similar patterns were observed at Sites 814, 817, and 819 (see "Site 814," "Site 817," and "Site 819" chapters, this volume). Velocity and density within the open-hole logged interval are somewhat greater than normally are observed in terrigenous or calcareous sediments of comparable depths. Average velocity increases from 1.7 km/s at 80 mbsf to 2.4 to 2.5 km/s at 380 mbsf, compared with typical values for these depths of 1.55 to 1.60 and 1.9 to 1.95 km/s (Hamilton, 1979). Density increases very little, from 2.0 g/cm^3 at 80 mbsf to 1.8 to 2.2 g/cm^3 at 310 to 350 mbsf, compared with typical values for these depths of about 1.64 and 1.98 g/cm^3 (Hamilton, 1976).

The density log has a half dozen intervals that may be affected by poor pad contact. Thus, we used the neutron log to evaluate the extent of problems with the density log and to determine porosity, as follows. The raw density log was converted to porosity, assuming a constant grain density of 2.71 (see "Physical Properties" section, this chapter). Comparison of this porosity log to the uncalibrated neutron porosity log indicated that the bulk of the neutron porosity values were too high by a factor of 2.8. This ratio did not hold in the washed-out intervals having anomalously high, density-based porosities. Neutron porosities then were divided by 2.8 and converted to density, again using a grain density of 2.71.

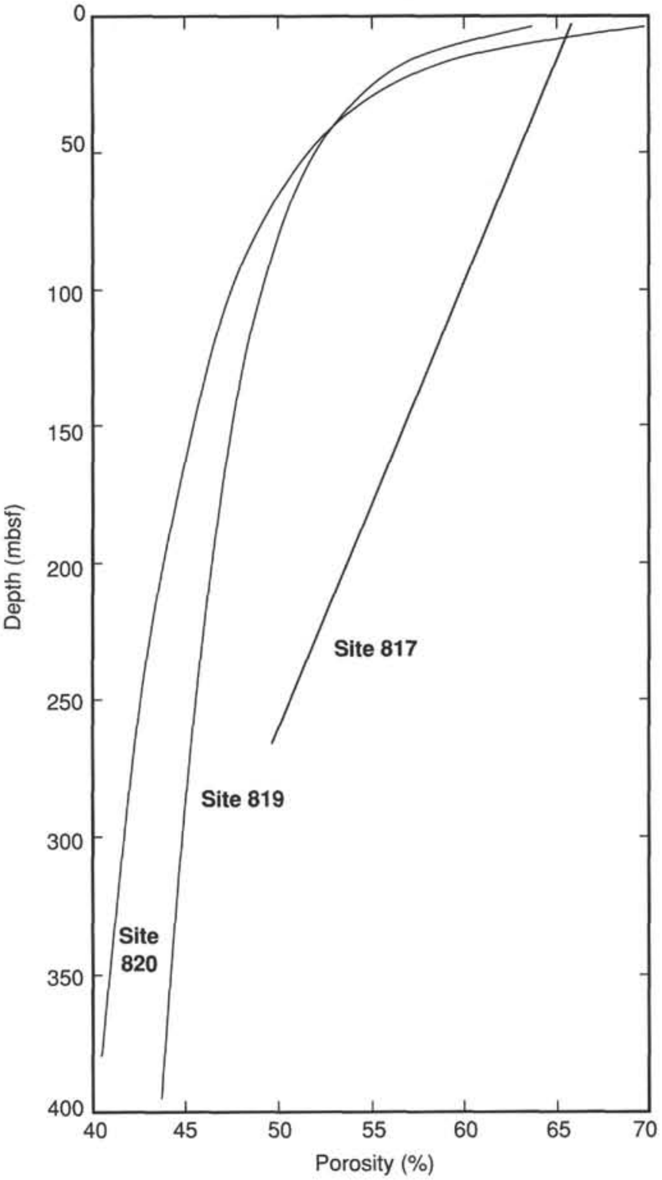

Figure 24. Generalized porosity-depth trends for Sites 817, 819, and 820, obtained by linear regression of porosity vs. depth for Site 817 and ln porosity vs. ln depth at Sites 819 and 820. Sediments at Site 817 experienced a different style of compaction from those at Sites 819 and 820, which is most probably related to differences in composition. These curves may suggest different consolidation processes acting at the two sites.

This neutron porosity value was used to calculate the Archie component, *m* (Fig. 32), to assess possible changes in style of pore structure (see "Site 817" chapter, this volume). Although the Archie (1942) relationship may not be applicable in this lithology, it can identify a trend for further study. For example, washouts where density is in error have anomalously high values of *m*. If pore morphology changes with

Table 6. Concentrations of total organic carbon, inorganic carbon, total carbon, total nitrogen, and sulfur in headspace samples from Site 820.

Core, section, interval (cm)	Depth (mbsf)	Sample	Total organic carbon (%)	Total inorganic carbon (%)	Total carbon (%)	Total nitrogen (%)	Total sulfur (%)	TOC/nitrogen	TOC/sulfur
133-820A-									
1H-3, 102–104	4.02	PP	0.22	6.52	6.74	0.02	0	11	
2H-5, 145–150	14.65	XRD	0.3	6.82	7.12	0.03	0	10	
3H-5, 145–150	24.15	XRD	0.39	7.72	8.11	0.03	0	13	
4H-5, 140–150	33.6	XRD	0.29	9.1	9.39	0.02	0	14	
5H-5, 140–150	43.1	XRD	0.38	9.09	9.47	0.03	0	12	
6H-5, 140–150	52.6	XRD	0.31	9.32	9.63	0.01	0	31	
7H-5, 140–150	62.1	XRD	0.42	4.33	4.75	0.03	0	14	
8H-1, 140–150	65.6	XRD	0.18	7.71	7.89	0.02	0	9	
9H-5, 140–150	81.1	XRD	0.19	8.61	8.8	0.02	0	9.5	
10H-5, 140–150	90.6	XRD	0.09	9.31	9.4	0.01	0	9	
11H-3, 100–103	96.7	PP	0.45	8.75	9.2	0.02	0	22	
12H-3, 100–103	106.2	PP	0.38	9.4	9.78	0.02	0	19	
13H-5, 140–150	119.1	XRD	0.33	8.46	8.79	0.02	0	16	
14H-1, 140–150	122.6	XRD	0.41	4.14	4.55	0.03	0	13	
15H-3, 57–60	135.27	PP	0.16	9.81	9.97	0.01	0	16	
820B-15H-5, 140–150	138.1	XRD	0.17	8.07	8.24	0.01	0.03	17	5.6
820A-16H-V-1, 140–150	141.6	XRD	0.21	7.13	7.34	0.02	0	10	
133-820B-									
16H-1, 57–60	141.77	PP	0.37	7.46	7.83	0.01	0.06	37	6.1
17H-3, 140–150	155.1	XRD	0.25	4.58	4.83	0.03	0.06	8.3	4.1
18X-3, 54–56	163.74	PP	0.14	6.6	6.74	0.03	0.04	4.6	3.5
19X-3, 90–93	169.1	PP	0.21	8.89	9.1	0.01	0.07	21	3
20X-5, 140–150	182.2	XRD	0.36	9.14	9.5	0.02	0	18	
21X-3, 90–92	188	PP	0.24	8.47	8.71	0.02	0.02	12	12
22X-6, 0–2	201.2	XRD	0.21	3.39	3.6	0.03	0.04	7	5.2
23X-2, 140–150	206.3	XRD	0.2	7.11	7.31	0.01	0	20	
24X-3, 90–93	216.7	PP	0.34	9.14	0.02		0	17	
25X-3, 90–93	226.4	PP	0.29	8.74	9.03	0.01	0	29	
26X-1, 90–93	233	PP	0.14	6.39	6.53	0.03	0.05	4.6	2.8
27X-3, 140–150	246.2	XRD	0.24	8.25	8.49	0.01	0	24	
28X-3, 10–13	254.2	PP	0.03	7.4	7.43	0.02	0.06	1	0.5
30X-1, 140–150	271.8	XRD	0.31	9.51	9.82	0.02	0.02	15	15
32X-2, 92–95	292.12	PP	0.36	7.67	8.03	0.02	0.17	18	2.1
33X-1, 90–93	300.3	PP	0.15	4.96	5.11	0.04	0.2	3.7	0.75
34X-CC, 10–13	309.54	PP	0.26	5.15	5.41	0.05	0.09	5.2	2.9
36X-5, 140–150	335.9	XRD	0.23	6.56	6.79	0.03	0.06	7.6	3.8
37X-3, 16–19	341.36	PP	0.23	2.73	2.96	0.06	0.21	3.8	1.1
38X-3, 13–16	351.03	PP	0.36	4.69	5.05	0.05	0	7.2	
39X-3, 12–15	360.62	PP	0.14	7.01	7.15	0.04	0.13	3.5	1.1
40X-3, 23–25	365.93	PP	0.14	7.72	7.86	0.05	0.13	2.8	1.1
41X-3, 12–15	370.22	PP	0.25	8.89	9.14		0.02	12	12
42X-3, 11–13	379.81	PP	0.14	8.91	9.05	0.03	0.08	4.6	1.7
44X-2, 33–34	397.83	PP	0.31	7.87	8.18	0.03	0.01	10	31

PP = physical properties sample; XRD = X-ray diffraction sample.

lithology, then *m* will vary and can be used as an additional indicator. Similarly, velocity and resistivity ratios (Fig. 35) are useful for identifying changes in pore morphology.

The velocity log was converted to an integrated traveltime log (Fig. 36) to facilitate depth-to-time conversion for comparing Site 820 data with seismic facies. For the unlogged interval between the seafloor and 73.9 mbsf, we used a simple linear interpolation between water velocity at the seafloor and the first log value at 73.9 mbsf. We subjectively estimate an error of less than 5 ms associated with uncertainties of velocities in the top 73.9 mbsf.

Vertical Seismic Profile

The vertical seismic profile (VSP) at Site 820B was a true VSP, with approximately 20-m spacing of geophone-clamping stations and with recording of full waveforms. However, shipboard analysis was confined to first-break arrivals, rather than waveform processing; thus, this analysis is more appropriately considered to be a checkshot survey.

Acquisition parameters for the VSP were as follows. The Schlumberger well seismic tool (WST) was the tool used downhole; the WST is a one-component (vertical) geophone that is clamped against the borehole wall by a spring-arm. The zero depth datum for the tool was the rig floor, 10.7 m above sea level. A reference hydrophone was 15.2 m below sea level. The *Resolution*'s 80 in.^{3} water gun was fired at a depth of 13.7 m below sea level, at a horizontal offset of 48.5 m from the drill string and an offset direction of 188°.

Spacing between geophone-clamping stations was only approximately uniform, because uniform spacing was a lower priority than selection of small-diameter intervals of the hole to maximize our chances for good clamping. We found that the two-axis caliper of the FMS (Fig. 31) was particularly useful for selecting clamping depths. Five to ten shots were fired and recorded at each clamping depth. One-way traveltimes shown in Table 12 represent the results of a simple stack of the three to seven best shots at each depth. We subjectively estimate the error in checkshot traveltime at each depth as about 1 ms. This small error will be reduced further during post-cruise full-waveform analysis, but its magnitude is large enough to make interval velocities over short 20-m intervals unreliable.

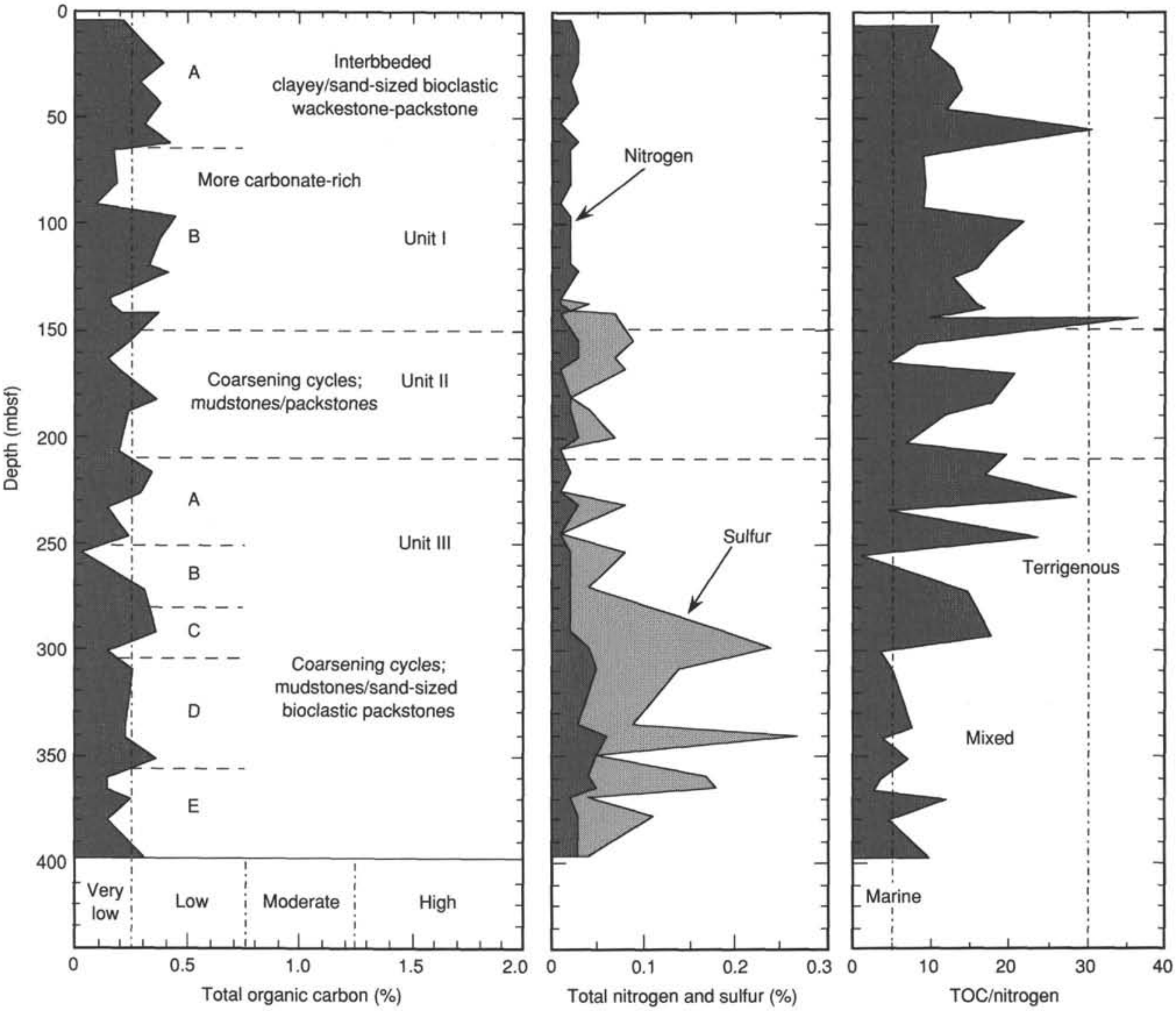

Figure 25. Distribution with depth of concentrations of total organic carbon, sulfur, and nitrogen, and of TOC/nitrogen ratio in headspace samples at Site 820.

A checkshot survey provides a ground-truth traveltime to specific horizons that is independent of assumptions made when comparing hole depth to seismic time by the two alternative methods more routinely used during Leg 133: synthetic seismograms (see "Seismic Stratigraphy" section, this chapter) and integrated sonic logs (Fig. 36). Consequently, comparison of checkshot results with results of the other two techniques used at Site 820 has implications for reliability of these two techniques at all other Leg 133 sites. Implicit in the use of synthetic seismograms is the assumption that a wavelet is accurate. Implicit in use of a log-based integrated traveltime function is an assumed traveltime for the unlogged top of the hole. Implicit in both types of analyses is the assumption that velocities measured at the borehole wall are representative of larger-scale formation velocities seen in seismic profiling.

Our integrated sonic log (Fig. 36) implied that total one-way traveltime between the shallowest (93.8 mbsf) and deepest (334.6 mbsf) checkshots was 117.6 ms; checkshots indicated that one-way traveltime was 117 ms. This agreement is well within checkshot uncertainties and confirms the reliability of our integrated sonic relative traveltimes. Assuming a water velocity of 1.5 km/s, one-way traveltime to the seafloor is 186.4 ms, implying a traveltime for 0 to 93.8 mbsf of 52.6 ms, based on checkshots. In contrast, our estimate of the integrated-sonic value is 57.9 ms, assuming a linearly increasing velocity from 1.5 km/s at the seafloor to 1.7 km/s at the first velocity log value at 73.9 mbsf. We had subjectively estimated potential error in this estimate as <5 ms at Site 820, and as <4 to 7 ms at other Leg 133 sites.

Log-Based Units

Lithostratigraphy at Site 820 is dominated by variations in concentration of the two principal components: calcite (either nannofossils or micrite) and clay minerals. This conclusion is based on smear-slide descriptions (see "Lithostratigraphy" section, this chapter) and was independently demonstrated by the geochemical logs. Figure 37 shows a strong correlation among logs obtained using three different tools. The elements potassium, aluminum, and silicon (all abundant in the clay minerals illite and kaolinite) correlate positively with each other and correlate inversely with abundances of calcium. Thus, these geochemical logs are semiquantitative indicators of relative abundance of calcite and clay minerals. Accordingly, calcite analyses of core samples correlate well with logs (see "Lithostratigraphy" section, this chapter).

Table 7. Index properties data, Site 820.

Core, section, interval (cm)	Depth (mbsf)	Bulk density (g/cm³)	Grain density (g/cm³)	Porosity (%)	Water content (%)	Void ratio
133-820A-						
1H-1, 102–105	1.02	1.72	2.64	63.3	60.5	1.72
1H-2, 102–105	2.52	1.72	2.70	62.1	58.4	1.64
1H-3, 102–105	4.02	1.72	2.74	62.5	59.0	1.66
1H-4, 102–105	5.52	1.64	2.74	67.9	74.0	2.11
1H-5, 62–65	6.62	1.65	2.76	67.6	72.6	2.09
2H-1, 22–25	7.42	1.78	2.69	55.0	46.4	1.22
2H-1, 103–105	8.23	1.82	2.68	56.3	46.3	1.29
2H-2, 103–105	9.73	1.82	2.72	57.0	47.0	1.32
2H-3, 103–105	11.23	1.77	2.74	59.9	53.1	1.49
2H-4, 103–105	12.73	1.66	2.77	60.0	58.9	1.50
2H-5, 103–105	14.23	1.76	2.80	61.7	55.9	1.61
2H-6, 103–105	15.73	1.71	2.74	60.2	56.7	1.51
3H-1, 100–103	17.70	1.77	2.70	55.1	46.7	1.23
3H-2, 100–103	19.20	1.88	2.71	54.7	42.7	1.21
3H-3, 100–103	20.70	1.81	2.65	57.7	48.4	1.37
3H-4, 100–103	22.20	1.87	2.75	55.1	43.0	1.23
3H-5, 100–103	23.70	1.88	2.68	56.2	44.2	1.28
3H-6, 100–103	25.20	1.95	2.69	58.7	44.5	1.42
4H-1, 100–103	27.20	1.86	2.71	54.6	42.9	1.20
4H-2, 100–103	28.70	1.84	2.72	56.5	46.0	1.30
4H-3, 100–103	30.20	1.75	2.76	59.8	53.7	1.49
4H-4, 100–103	31.70	1.77	2.57	59.1	51.8	1.44
4H-5, 100–103	33.20	2.02	2.96	52.1	35.9	1.09
4H-6, 100–103	34.70	1.88	2.77	54.2	41.8	1.18
5H-1, 100–103	36.70	2.06	2.73	54.0	36.6	1.17
5H-2, 100–103	38.20	1.88	2.69	50.5	38.0	1.02
5H-3, 100–103	39.70	1.93	2.64	51.5	37.7	1.06
5H-4, 100–103	41.20	1.97	2.79	50.1	35.3	1.01
5H-5, 100–103	42.70	1.94	2.71	50.9	36.7	1.04
5H-6, 100–103	44.20	1.87	2.71	50.8	38.6	1.03
6H-1, 100–103	46.20	1.86	2.74	55.9	44.5	1.27
6H-2, 100–103	47.70	1.88	2.69	53.7	41.3	1.16
6H-3, 100–103	49.20	1.91	2.69	54.1	40.8	1.18
6H-4, 100–103	50.70	1.93	2.71	55.4	41.6	1.24
6H-5, 100–103	52.20	1.90	2.74	52.3	39.2	1.10
6H-6, 100–103	53.70	1.98	2.75	55.0	39.6	1.22
7H-1, 100–103	55.70	2.06	2.73	56.5	39.0	1.30
7H-2, 100–103	57.20	1.93	2.71	52.7	38.7	1.11
7H-3, 100–103	58.70	1.92	2.72	50.9	37.2	1.04
7H-4, 100–103	60.20	1.95	2.71	50.3	35.9	1.01
7H-5, 100–103	61.70	1.87	2.71	54.6	42.6	1.20
7H-6, 100–103	63.20	1.82	2.73	57.3	47.7	1.34
8H-1, 100–103	65.20	1.90	2.78	51.8	38.7	1.08
8H-2, 100–103	66.70	1.91	2.77	52.6	39.3	1.11
8H-3, 100–103	68.20	2.05	2.80	48.4	31.9	0.94
8H-4, 100–103	69.70	1.97	2.80	49.1	34.4	0.96
8H-5, 100–103	71.20	1.82	2.77	46.1	35.1	0.86
8H-6, 100–103	72.70	1.92	2.71	50.5	36.8	1.02
9H-1, 100–103	74.70	1.92	2.74	51.7	38.1	1.07
9H-2, 100–103	76.20	1.96	2.76	52.8	38.2	1.12
9H-3, 100–103	77.70	1.89	2.74	52.6	39.9	1.11
9H-4, 100–103	79.20	1.99	3.12	49.9	34.5	1.00
9H-5, 100–103	80.70	1.99	2.80	49.1	33.9	0.96
9H-6, 100–103	82.20	1.83	2.63	49.2	37.9	0.97
10H-1, 100–103	84.20	1.99	2.56	50.6	35.3	1.02
10H-2, 100–103	85.70	1.98	2.81	49.9	34.7	0.99
10H-3, 100–103	87.20	1.95	2.76	48.2	33.8	0.93
10H-4, 100–103	88.70	1.89	2.78	51.8	39.0	1.07
10H-5, 100–103	90.20	1.98	2.75	47.8	32.9	0.92
10H-6, 100–103	91.70	1.97	2.76	50.6	35.7	1.03
11H-1, 100–103	93.70	2.00	2.81	46.3	31.0	0.86
11H-2, 100–103	95.20	1.88	2.84	47.2	34.7	0.89
11H-3, 100–103	96.70	2.00	2.76	46.3	31.2	0.86
11H-4, 100–103	98.20	2.03	2.76	45.1	29.5	0.82
11H-5, 100–103	99.70	2.05	2.76	45.2	29.1	0.82
11H-6, 100–103	101.20	2.08	2.80	45.6	28.9	0.84
12H-1, 100–103	103.20	2.03	2.75	45.0	29.4	0.82
12H-2, 100–103	104.70	2.09	2.75	44.0	27.6	0.79
12H-3, 100–103	106.20	2.01	2.62	46.0	30.7	0.85
12H-4, 100–103	107.70	2.01	2.81	46.8	31.3	0.88
12H-5, 100–103	109.20	2.01	2.74	46.1	30.7	0.86
12H-6, 100–103	110.70	2.05	2.75	44.8	28.9	0.81
13H-1, 100–103	112.70	2.12	3.05	45.7	28.4	0.84
13H-2, 100–103	114.20	1.92	2.78	43.1	30.0	0.76
13H-3, 100–103	115.70	2.06	2.74	43.5	27.6	0.77
13H-4, 100–103	117.20	2.01	2.98	47.7	32.2	0.91
13H-5, 100–103	118.70	1.93	2.70	47.1	33.2	0.89
13H-6, 100–103	120.20	2.02	2.84	44.6	29.2	0.81
14H-1, 100–103	122.20	2.07	2.78	45.4	29.0	0.83
15H-1, 100–103	131.70	1.98	2.78	46.3	31.6	0.86
15H-2, 100–103	133.20	2.03	2.74	44.7	29.2	0.81
15H-3, 100–103	134.70	2.16	2.77	46.6	28.4	0.87
15H-4, 100–103	136.20	2.05	2.78	43.2	27.6	0.76
15H-5, 100–103	137.70	2.18	2.78	39.7	23.0	0.66
15H-6, 100–103	139.20	1.87	2.78	54.1	42.1	1.18
16V-1, 100–103	141.20	2.07	2.80	43.5	27.4	0.77
133-820B-						
14H-1, 76–79	122.96	1.98	2.73	45.5	30.8	0.83
14H-2, 76–79	124.46	1.94	2.86	49.3	35.2	0.97
14H-3, 76–79	125.96	2.03	2.74	45.5	29.8	0.84
14H-4, 76–79	127.46	2.08	2.80	42.8	26.8	0.75
14H-5, 76–79	128.96	2.06	2.75	42.8	27.1	0.75
14H-6, 76–79	130.46	1.97	2.73	46.9	32.3	0.88
15H-1, 57–60	132.27	2.04	2.75	43.5	27.9	0.77
15H-2, 57–60	133.77	2.06	2.83	43.0	27.2	0.76
15H-3, 57–60	135.27	2.12	2.74	40.4	24.2	0.68
15H-4, 57–60	136.77	1.97	2.89	42.8	28.6	0.75
15H-5, 57–60	138.27	2.05	2.79	43.2	27.4	0.76
15H-6, 57–60	139.77	2.08	2.78	42.2	26.2	0.73
16H-1, 57–60	141.77	2.04	2.80	43.7	28.2	0.78
16H-2, 57–60	143.27	2.00	2.79	46.3	31.2	0.86
17H-1, 33–36	151.03	1.98	2.74	44.7	30.0	0.81
17H-2, 33–36	152.53	2.01	2.73	46.0	30.6	0.85
17H-3, 33–36	154.03	2.04	2.74	43.4	27.9	0.77
17H-4, 33–36	155.53	1.98	2.72	45.4	30.6	0.83
18X-1, 54–57	160.74	1.97	2.79	49.6	34.9	0.99
18X-2, 54–57	162.24	1.98	2.73	49.9	34.7	0.99
18X-3, 54–57	163.74	1.98	2.62	49.7	34.7	0.99
18X-4, 54–57	165.24	2.03	2.85	44.7	29.1	0.81
19X-1, 90–93	166.10	1.99	2.80	46.8	31.8	0.88
18X-5, 54–57	166.74	1.94	2.77	50.7	36.5	1.03
19X-2, 90–93	167.60	1.99	2.81	45.9	31.0	0.85
18X-6, 54–57	168.24	2.08	2.72	42.7	26.7	0.75
19X-3, 90–93	169.10	2.04	2.76	44.4	28.6	0.80
19X-4, 90–93	170.60	2.05	2.72	46.1	30.0	0.86
19X-5, 90–93	172.10	2.05	2.79	42.4	26.8	0.74
19X-6, 90–93	173.60	2.05	2.72	48.2	31.8	0.93
20X-1, 90–93	175.70	2.01	2.73	46.6	31.1	0.87
20X-2, 90–93	177.20	2.01	2.76	46.1	30.8	0.85
20X-3, 90–93	178.70	2.00	2.72	44.8	29.7	0.81
20X-4, 90–93	180.20	1.88	2.78	53.2	40.8	1.14
20X-5, 90–93	181.70	2.04	2.80	44.6	28.9	0.81
20X-5, 90–93	183.20	1.99	2.73	46.2	31.2	0.86
21X-1, 90–93	185.00	1.97	2.76	46.5	31.9	0.87
21X-2, 96–99	186.56	1.97	2.94	45.6	31.1	0.84
21X-3, 90–93	188.00	2.02	2.74	45.0	29.6	0.82
21X-4, 90–93	189.50	2.04	2.71	43.0	27.6	0.75
21X-5, 90–93	191.00	2.11	2.77	38.9	23.4	0.64
21X-6, 90–93	192.50	2.10	2.76	41.3	25.3	0.70
22X-1, 90–93	194.60	1.94	2.78	49.5	35.4	0.98
22X-2, 90–93	196.10	1.93	2.76	48.9	35.2	0.96
22X-3, 90–93	197.60	1.95	2.72	48.6	34.2	0.95
22X-4, 90–93	199.10	1.95	2.77	49.3	34.9	0.97
22X-5, 90–93	200.60	1.96	2.75	47.1	32.7	0.89
22X-6, 90–93	202.10	1.99	2.75	45.6	30.7	0.84
23X-1, 90–93	204.30	2.08	2.79	42.6	26.5	0.74
23X-2, 90–93	205.80	2.07	2.80	43.6	27.5	0.77
23X-3, 90–93	207.0	2.05	2.77	46.7	30.4	0.88
23X-4, 90–93	208.80	2.05	2.75	43.3	27.6	0.76
23X-5, 90–93	210.30	2.04	2.77	45.1	29.2	0.82
23X-6, 90–93	211.70	2.05	2.74	45.9	29.8	0.85
24X-1, 90–93	213.70	1.97	2.75	47.0	32.4	0.89
24X-2, 90–93	215.20	1.98	2.77	46.9	32.0	0.89
24X-3, 90–93	216.70	2.07	2.79	47.2	30.5	0.89
24X-4, 90–93	218.20	2.12	2.77	41.3	25.0	0.70
24X-5, 90–93	219.70	2.06	2.64	40.7	25.4	0.69
24X-6, 90–93	221.20	2.10	2.78	40.6	24.7	0.68
25X-1, 90–93	223.40	2.07	2.67	43.1	27.2	0.76
25X-2, 90–93	224.90	2.05	2.79	44.7	28.9	0.81
25X-3, 90–93	226.40	2.01	2.71	45.3	30.1	0.83
26X-1, 90–93	233.00	2.07	2.77	43.9	27.8	0.78
27X-2, 40–43	243.70	2.12	2.83	40.5	24.3	0.68
27X-3, 40–43	245.20	2.11	2.77	41.2	25.0	0.70
27X-4, 40–43	246.70	2.07	2.76	41.8	26.0	0.72
27X-5, 40–43	248.20	2.07	2.70	40.9	25.3	0.69
28X-1, 40–43	251.50	2.03	2.73	44.6	29.0	0.81
28X-2, 40–43	253.00	2.00	2.74	47.5	32.1	0.91
28X-3, 40–43	254.50	2.05	2.78	40.7	25.5	0.69
28X-4, 40–43	256.00	2.08	2.72	41.2	25.5	0.70
28X-5, 40–43	257.50	2.13	2.73	38.5	22.7	0.63
30X-1, 97–100	271.37	2.06	2.73	43.8	27.9	0.78
30X-2, 57–60	272.47	2.10	2.73	38.8	23.4	0.63
32X-2, 93–96	292.13	2.19	2.72	35.5	19.9	0.55
33X-1, 93–96	300.33	2.06	2.71	43.0	27.2	0.75
33X-2, 93–96	301.83	2.07	2.76	44.5	28.3	0.80
33X-3, 93–96	303.33	2.03	2.75	43.1	27.7	0.76
33X-4, 93–96	304.83	2.04	2.71	45.8	29.8	0.84
33X-5, 93–96	306.33	2.00	2.72	46.1	31.0	0.86
34X-CC, 10–13	309.54	2.05	2.75	45.7	29.7	0.84
36X-1, 9–11	328.59	2.12	2.81	39.4	23.5	0.65
36X-2, 26–28	330.26	2.18	2.72	39.9	23.1	0.67
36X-3, 26–28	331.76	2.20	2.69	38.1	21.6	0.62
36X-4, 26–28	333.26	2.23	2.67	41.1	23.4	0.70
36X-5, 26–28	334.76	2.13	2.74	38.4	22.7	0.62
36X-6, 26–28	336.26	2.11	2.75	41.3	25.1	0.70
37X-1, 16–19	338.36	2.09	2.91	43.7	27.3	0.78
37X-2, 16–19	339.86	2.07	2.75	44.1	28.0	0.79
37X-3, 16–19	341.36	2.01	2.77	42.9	28.0	0.75
37X-4, 16–19	342.86	2.02	2.75	45.3	29.8	0.83
38X-1, 13–16	348.03	2.00	2.83	49.9	34.3	1.00
38X-2, 13–16	349.53	2.09	2.73	47.0	30.0	0.89
38X-3, 13–16	351.03	2.06	2.83	44.6	28.4	0.81
38X-4, 13–16	352.53	2.05	2.77	46.0	29.8	0.85
39X-1, 15–18	357.65	2.01	2.77	47.7	32.2	0.91
39X-2, 9–12	359.09	2.34	2.50	36.3	18.9	0.57
39X-3, 12–15	360.62	2.09	2.95	41.5	25.6	0.71
40X-1, 12–15	362.82	2.44	2.85	26.5	12.5	0.36
40X-2, 12–15	364.32	2.23	2.76	35.0	19.2	0.54
40X-3, 12–15	365.82	2.13	2.76	41.4	24.9	0.71
41X-1, 12–15	367.22	2.28	2.74	28.0	14.4	0.39
41X-2, 12–15	368.72	2.25	2.73	38.7	21.4	0.63
41X-3, 12–15	370.22	2.28	2.72	32.3	17.0	0.48
41X-4, 12–15	371.72	2.30	2.74	31.1	16.1	0.45
41X-5, 12–15	373.22	2.18	2.75	35.1	19.8	0.54
42X-1, 10–13	376.80	2.22	2.73	34.2	18.7	0.52
42X-2, 9–11	378.29	2.13	2.73	35.2	20.3	0.54
42X-3, 10–12	379.80	2.30	2.69	34.1	17.9	0.52
42X-4, 10–13	381.30	2.18	2.58	35.8	20.2	0.56
42X-5, 10–13	382.80	2.24	3.09	37.8	21.0	0.61
44X-1, 31–33	396.31	2.17	2.73	37.9	21.8	0.61
44X-2, 31–33	397.81	2.14	2.72	43.8	26.5	0.78

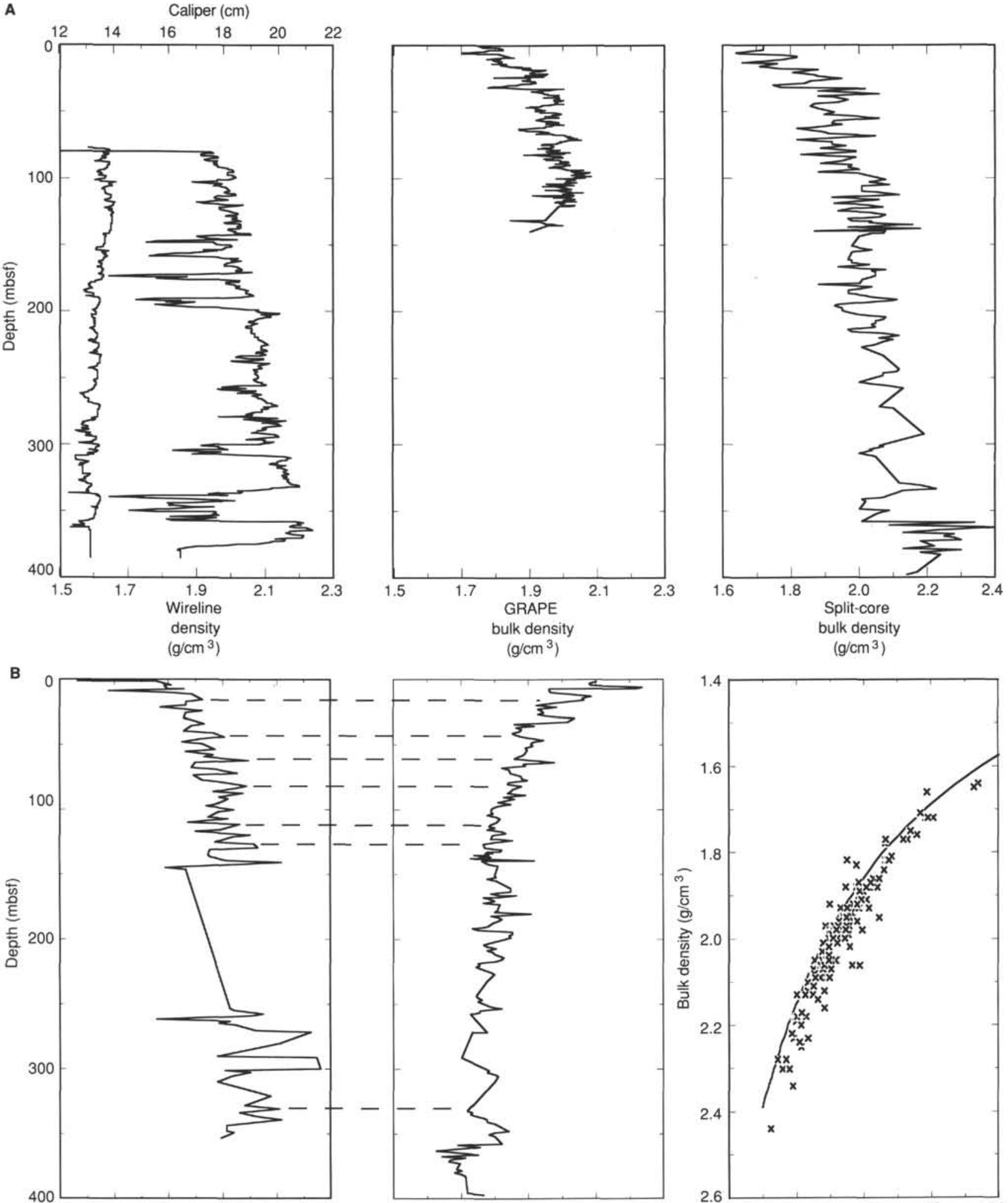

Figure 26. **A.** Wireline, unfiltered GRAPE, and split-core bulk density measurements for Site 820. The caliper log was plotted with wireline density profile to indicate portions of data that are unreliable because of varying hole conditions. **B.** Thermal conductivity and water content at Site 820. Dashed lines indicate the inverse correlation between water content and thermal conductivity. Graph on right displays actual measurements of water content and bulk density (shown by "*x*"s), along with a line representing the expected relationship between bulk density and water content for a two-component system of seawater and grains having a grain density of 2.76 g/cm^3. Dashed lines indicate the inverse correlation between water content and thermal conductivity.

Table 8. Compressional-wave velocity data, Site 820.

Core, section, interval (cm)	Depth (mbsf)	Distance (mm)	Traveltime (μs)	Velocity (m/s)
133-820A-				
1H-1, 102–105	1.02	29.43	21.51	1542
1H-2, 102–105	2.52	29.52	21.49	1549
1H-3, 102–105	4.02	28.37	20.84	1540
1H-4, 102–105	5.52	27.84	20.81	1512
1H-5, 62–65	6.62	28.94	21.34	1529
2H-1, 22–25	7.42	28.11	19.20	1683
2H-1, 102–105	8.22	28.81	20.62	1586
2H-2, 102–105	9.72	29.71	21.20	1585
2H-3, 102–105	11.22	29.69	21.39	1567
2H-4, 102–105	12.72	29.15	21.40	1536
2H-5, 102–105	14.22	29.72	21.62	1549
2H-6, 102–105	15.72	29.52	21.38	1559
3H-1, 100–103	17.70	28.50	20.47	1582
3H-2, 100–103	19.20	27.67	19.86	1589
3H-3, 100–103	20.70	29.55	21.32	1566
3H-4, 100–103	22.20	29.56	21.06	1589
3H-5, 100–103	23.70	29.30	21.08	1573
3H-6, 100–103	25.20	29.08	20.86	1580
4H-1, 100–103	27.20	30.05	21.31	1595
4H-2, 100–103	28.70	30.94	22.13	1573
4H-3, 100–103	30.20	29.42	21.48	1544
4H-4, 100–103	31.70	29.11	20.99	1570
4H-5, 100–103	33.20	29.42	22.24	1482
4H-6, 100–103	34.70	29.77	21.04	1603
5H-1, 100–103	36.70	28.55	19.93	1636
5H-2, 100–103	38.20	28.90	20.17	1634
5H-3, 100–103	39.70	30.16	21.40	1593
5H-4, 100–103	41.20	30.47	24.00	1405
5H-5, 100–103	42.70	29.78	20.91	1615
5H-6, 100–103	44.20	29.73	20.96	1608
6H-1, 100–103	46.20	29.37	21.06	1578
6H-2, 100–103	47.70	30.37	21.54	1592
6H-3, 100–103	49.20	30.42	22.40	1522
6H-4, 100–103	50.70	30.85	21.89	1588
6H-5, 100–103	52.20	29.73	22.44	1482
6H-6, 100–103	53.70	28.99	20.54	1604
7H-1, 101–103	55.71	28.98	20.50	1607
7H-2, 100–103	57.20	29.03	20.40	1619
7H-3, 100–103	58.70	29.03	20.42	1618
7H-4, 100–103	60.20	29.03	20.41	1619
7H-5, 100–103	61.70	29.31	20.80	1598
7H-6, 100–103	63.20	30.54	21.86	1574
8H-2, 100–103	66.70	27.81	19.68	1616
8H-3, 100–103	68.20	29.73	20.91	1613
8H-4, 100–103	69.70	29.51	20.23	1664
8H-6, 100–103	72.70	28.95	20.03	1651
9H-1, 100–103	74.70	27.86	19.25	1662
9H-2, 100–103	76.20	29.18	20.30	1638
9H-3, 100–103	77.70	29.10	20.65	1600
10H-1, 100–103	84.20	28.88	21.78	1489
10H-2, 100–103	85.70	28.38	21.10	1518
10H-3, 100–103	87.20	28.81	20.08	1637
10H-4, 100–103	88.70	28.99	20.45	1612
10H-5, 100–103	90.20	28.50	20.44	1584
11H-1, 100–103	93.70	28.87	19.55	1694
11H-3, 100–103	96.70	29.10	21.84	1496

The five porosity logs in Figure 33 correlate moderately well with the gamma-ray log (SGR in Fig. 37), with gamma ray maxima corresponding to velocity, resistivity, and density minima. Furthermore, other geochemical logs (potassium, aluminum and silicon) correlate moderately with porosity logs. This pattern is not as strong as the correlation among porosity logs or the correlation among geochemical logs, but it does imply a substantial effect of mineralogy on porosity. This pattern is typical in ODP for variations in clay minerals. Higher concentrations of clay minerals are evidenced by higher gamma-ray counts, particularly if illite (3%–8% potassium; Serra, 1986) is a significant constituent of the clays, and clay minerals substantially increase the porosity of uncompacted (<2 km overburden) sediments.

The spectral gamma-ray values at Site 820 are similar in magnitude to those at nearby Sites 819 and 821, but are substantially higher than at previous Leg 133 sites. The potassium value in particular increased by more than a factor of 10, to values ranging from 0.5% to 1.0%. Thorium increased by a factor of three, and total SGR count nearly doubles that at Site 817 (see "Site 817" chapter, this volume), with values ranging from 30 to 50 API units. These patterns are attributable to much higher clay contents and proportionately lower carbonate contents at Sites 819, 820, and 821, compared to earlier Leg 133 sites.

Based on log responses, the openhole logged interval at Site 820 can be divided into three units and several subunits: log Unit 1 from the base of the pipe (69 mbsf) to 150 mbsf, log Unit 2 from 150 to 205 mbsf, and log Unit 3 from 205 mbsf to the bottom of the logged interval at 382 mbsf.

Log Unit 1 is characterized by a smooth compaction profile for velocity and resistivity logs, as shown in Figure 31. A small number of thin layers of higher resistivity and velocity can be seen that probably result from density changes within similar lithologies.

Log Unit 2 is characterized by a number of discrete washouts that correlate with increased potassium/SGR, indicating higher proportions of clay minerals in these discrete zones. Further inspection of intervening layers suggests that the Archie component, *m*, is decreasing upward (Fig. 32). Such a trend may have been caused by an increase in the proportion of clay minerals, which should result in a more platey shape to the particles; this is known to increase the value of *m*. This situation may have occurred between 179 to 192 mbsf, where *m* (Fig. 32) and the potassium/SGR decrease upward, whereas calcium contents increase (Fig. 37). This indicates a sequence that coarsens upward, where grain shapes are likely to become more spherical.

Log Unit 3 consists of a number of subunits in which calcium contents increase upward; these trends are most distinct in the depth interval from 205 to 350 mbsf. After careful examination, one can observe that most of these same log patterns described for log Unit 2 also occur in log Unit 3. Thus, the same interpretation of sequences that are coarsening upward probably applies. The change in Archie *m* is not so pronounced, but the same trends are evident. Note that washouts disturb the Archie *m* component to a greater extent than they disturb the geochemical logs, which explains the observed responses described above. These log-based upward-coarsening sequences are discussed in more detail in the "Lithostratigraphy" section (this chapter).

Temperature

We ran the L-DGO temperature tool at the bottom of the seismic stratigraphic and geochemical tool strings. Because hole temperatures were reduced by circulation during coring and by hole conditioning immediately before logging, we were unable to infer an equilibrium thermal profile reliably from only two temperature-logging runs. Our recorded maximum temperatures of 26.5° and 27.8°C thus are minimum estimates of equilibrium temperature. WSTP measurements of the thermal gradient at this site show an approximately linear increase in bottom-water temperature from 15.8° to 28°C at 250 mbsf (see "Physical Properties" section, this chapter). In comparison, temperature logging measurements of bottom-water temperature are 16.7° and 15.4°C (Fig. 38); two log measurements at 250 mbsf of 25.2° and 25.8°C show that the final approach to equilibrium temperatures is slow.

We ran the temperature tool, not to estimate heat flow, but in case fluid flow was present. In Figure 38, a plot of measured temperature as a function of pressure recorded simultaneously by this tool is presented. Depths shown are approximate and may be revised by up to 5 m during post-cruise merging of the Schlumberger time/depth data with the temperature-tool time/pressure data.

The temperature pattern in Figure 38 exhibits evidence of thermal lags resulting from a mud-clogged end sub. Mud

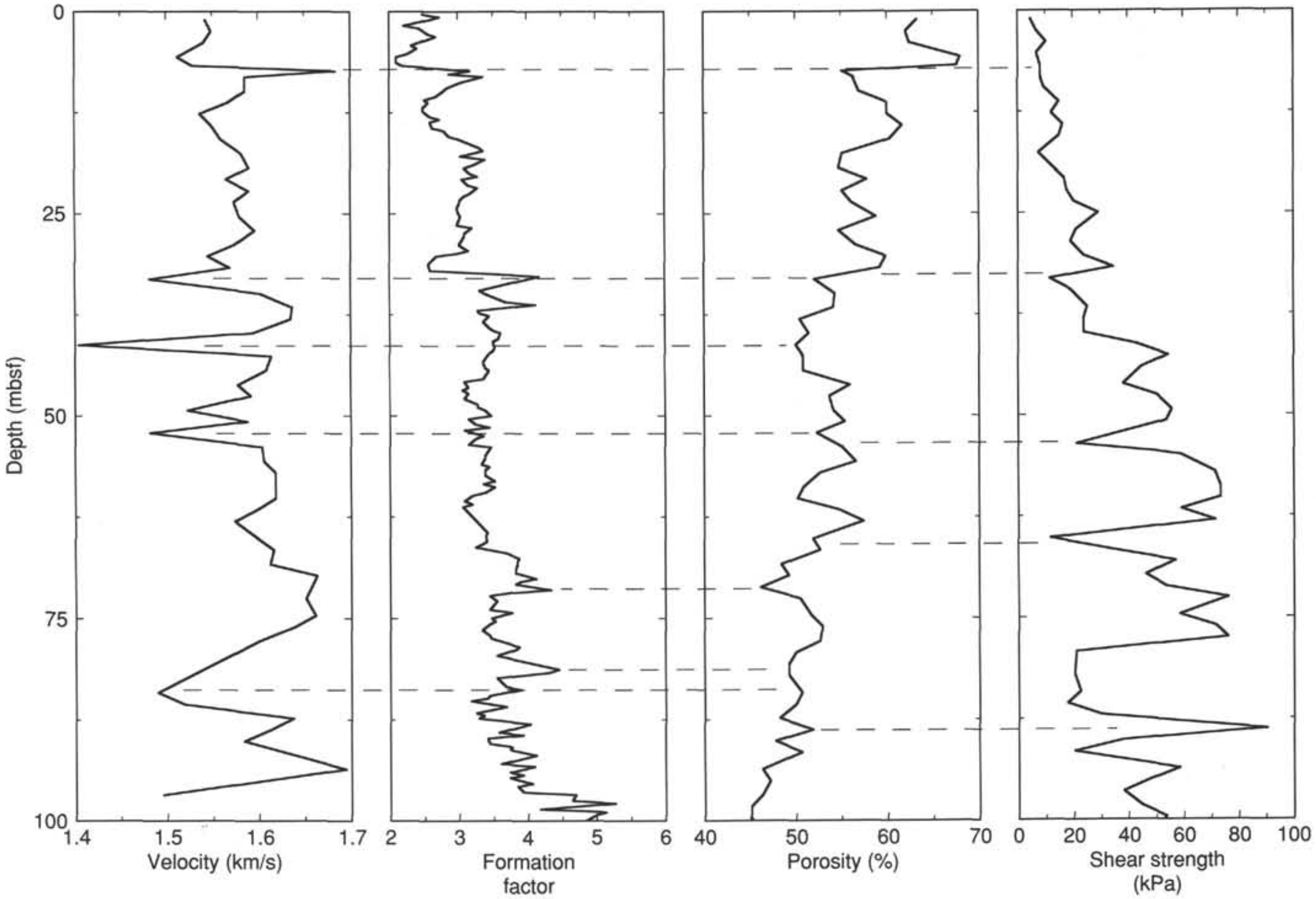

Figure 27. Sonic velocity, formation factor, porosity, and shear strength measured for split cores. Dashed lines indicate correlations between measurement series.

clogging can occur when the temperature tool, which is the last tool on the tool string, hits the bottom of a hole containing sticky clay. The effect on the log is a higher temperature for the upcoming log than for the downgoing log, and a maximum temperature recording not at the deepest point in the hole, but somewhat shallower than the deepest point on the upcoming log. When rigged down after logging, the temperature tool did have a mud-clogged end sub.

Downgoing logs probably were minimally affected by mud clogging. Their pattern exhibits approximately linear increasing temperature between the base of the pipe and the bottom of the hole. The first downgoing log indicates that through-pipe data are significantly cooler than those from the adjacent open hole. This effect decreases during subsequent passes (Run 1 up log, Run 2 down log, and Run 2 up log), until through-pipe data for Run 2 up log are approximately in equilibrium with the adjacent formation. The extrapolated bottom-water temperature (based on observed sub-bottom thermal gradients) is substantially warmer than the observed bottom-water temperature (Fig. 38). This discrepancy might be caused by either upward flux of pore fluids out of the formation or by bottom waters that are currently cooler than average; the latter seems more likely in these shallow waters.

Hole Deviation

At Hole 820B, the hole deviation measured by the FMS increases gradually from 1.8° at 100 mbsf to 2.2° at 300 to 360 mbsf (Fig. 39). Somewhat surprisingly, this deviation is to the south; we had expected more of a structural control on hole deviation.

REFERENCES

Archie, G. E., 1942. The electrical resistivity log as an aid in determining some reservoir characteristics. *J. Pet. Tech.*, 5:1–8.

Gieskes, J. M. 1981. Deep-Sea Drilling Project interstitial water studies: implications for chemical alteration of the oceanic crust, layers I and II. *Soc. Econ. Paleontol. Mineral. Spec. Publ.*, 32:149–167.

Hamilton, E. L., 1976. Variation of density and porosity with depth in deep-sea sediments. *J. Sediment. Pet.*, 46:280–300.

———, 1979. Sound velocity gradients in marine sediments. *J. Acoust. Soc. Am.*, 65:909–922.

Serra, O., 1986. *Fundamentals of Well-Log Interpretation 2. The Interpretation of Logging Data*: Amsterdam (Elsevier).

Symonds, P. A., Davies, P. J., and Parisi, A., 1983. Structure and stratigraphy of the central Great Barrier Reef. *BMR J. Aust. Geol. Geophys.*, 8:277–291.

van Morkhoven, F.P.C.M., Berggren, W. A., Edwards. A. S., et al., 1986. Cenozoic cosmopolitan deep-water benthic foraminifera. *Mem. Centre Rech. Explor. Prod. Elf. Aquitaine*, 11.

Ms 133-113

NOTE: All core description forms ("barrel sheets") and core photographs have been printed on coated paper and bound separately as Part 2 of this volume, beginning on page 813.

Formation microscanner images for this site are presented on microfiche in the back of Part 2.

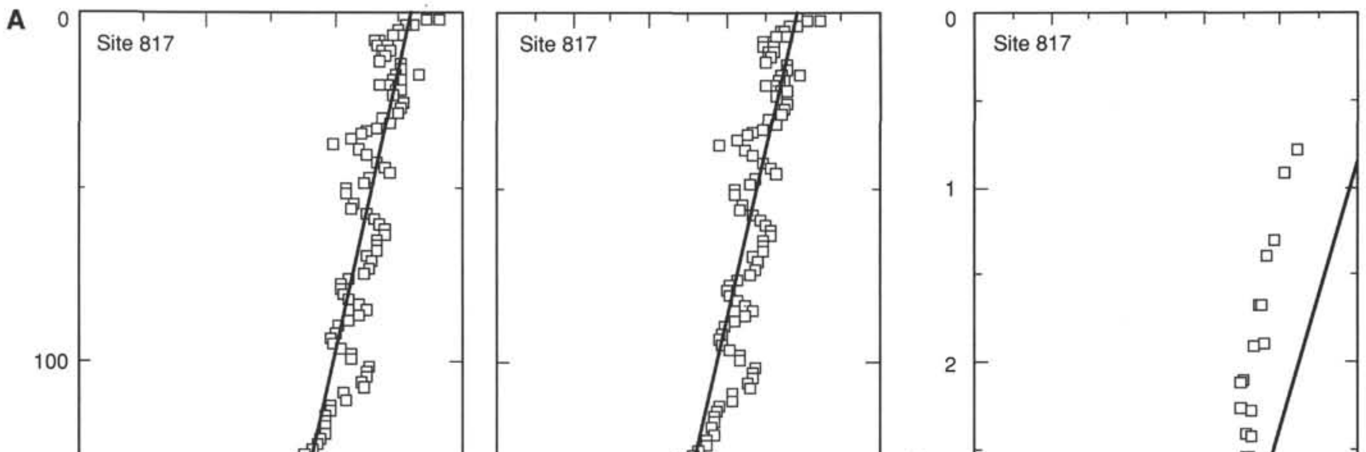

Figure 28. **A.** Plots of porosity-depth, ln porosity-depth, and ln porosity-ln depth data from Site 817. Linear regressions are shown for each plot along with R^2, where R is the regression coefficient. For Site 817, a linear regression of porosity vs. depth describes the actual data about as well as a linear regression of ln depth vs. depth. Both regressions describe actual data better than the regression of ln porosity vs. ln depth. **B.** Plots of porosity-depth, ln porosity-depth, and ln porosity-ln depth data from Site 819. Linear regressions are shown for each plot along with R^2, where R is the regression coefficient. For Site 819, a linear regression of ln porosity vs. ln depth describes actual data better than the other regressions. **C.** Plots of porosity-depth, ln porosity-depth, and ln porosity-ln depth data from Site 820. Linear regressions are shown for each plot along with R^2, where R = regression coefficient. For Site 820, the linear regression of ln porosity vs. ln depth is marginally better than the other two regressions for describing actual data.

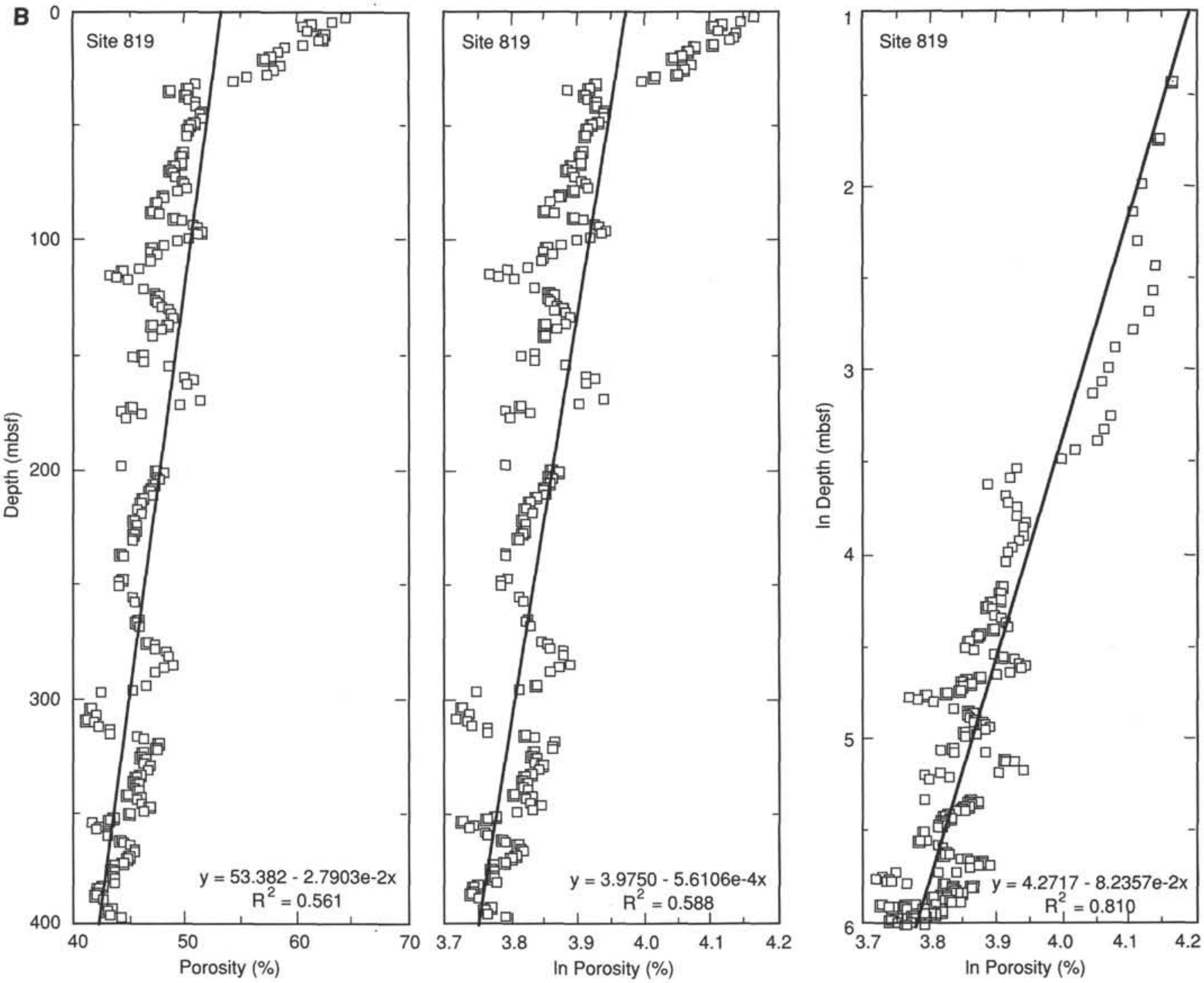

Figure 28 (continued).

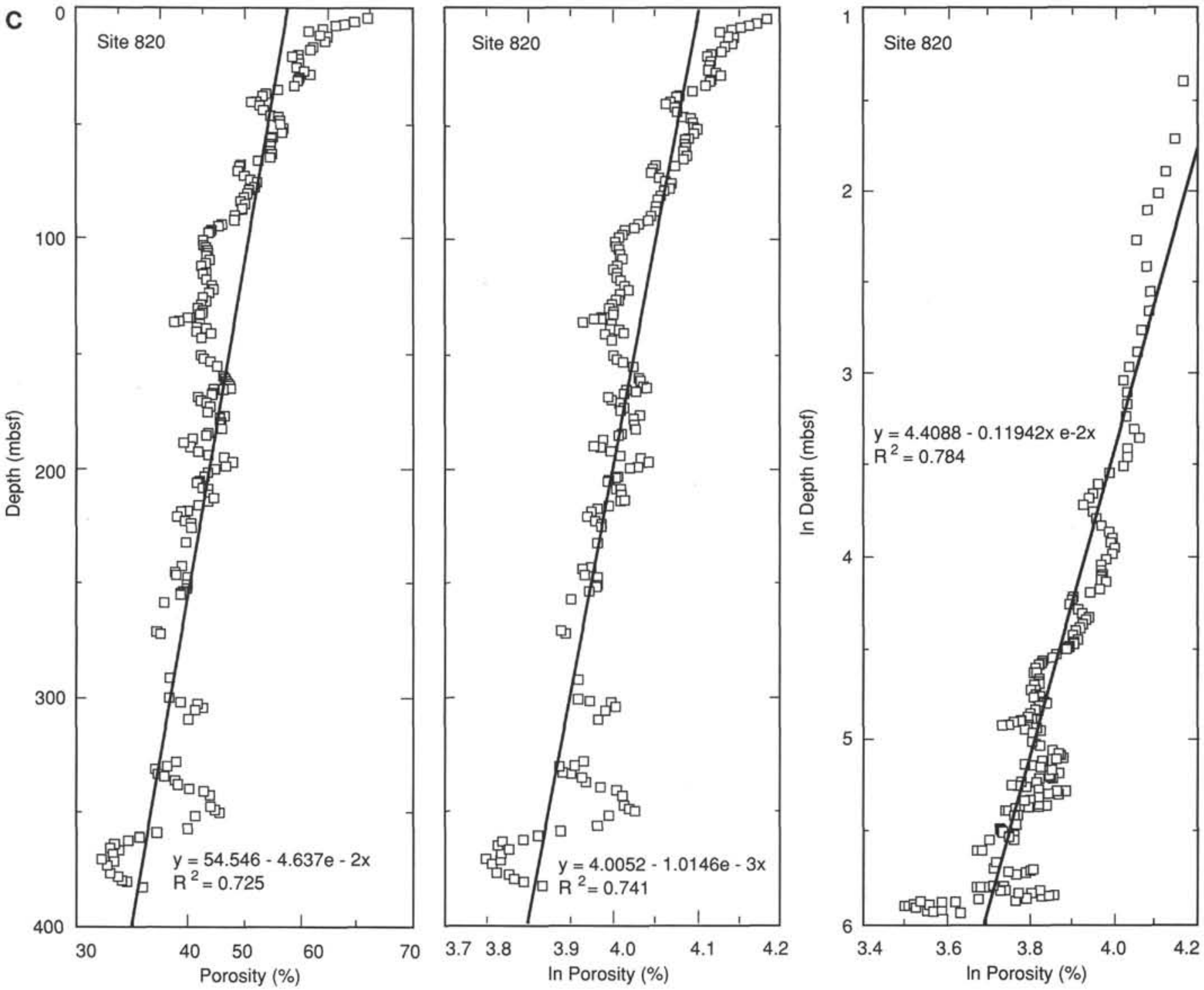

Figure 28 (continued).

Table 9. Electrical resistivity formation factor data, Site 820.

Core, section, interval (cm)	Depth (mbsf)	Seawater (ohms)	Sample (ohms)	Formation factor
133-820A-				
1H-1, 20–20	0.20	3.0	7.5	2.50
1H-1, 70–70	0.70	3.0	8.2	2.73
1H-1, 120–120	1.20	3.0	7.8	2.60
1H-2, 20–20	1.70	3.0	6.7	2.23
1H-2, 70–70	2.20	3.0	7.3	2.43
1H-2, 120–120	2.70	3.0	7.7	2.57
1H-3, 20–20	3.20	3.0	8.0	2.67
1H-3, 70–70	3.70	3.0	7.3	2.43
1H-3, 120–120	4.20	3.0	7.0	2.33
1H-4, 20–20	4.70	3.0	7.2	2.40
1H-4, 70–70	5.20	3.0	6.8	2.27
1H-4, 120–120	5.70	3.0	6.3	2.10
1H-5, 20–20	6.20	3.0	6.3	2.10
1H-5, 70–70	6.70	3.0	6.6	2.20
2H-1, 20–20	7.40	3.0	9.5	3.17
2H-1, 70–70	7.90	3.0	8.6	2.87
2H-1, 100–100	8.20	3.0	10.1	3.37
2H-2, 20–20	8.90	3.0	9.1	3.03
2H-2, 70–70	9.40	3.0	8.5	2.83
2H-2, 120–120	9.90	3.0	8.4	2.80
2H-3, 20–20	10.40	3.0	8.0	2.67
2H-3, 70–70	10.90	3.0	7.6	2.53
2H-3, 120–120	11.40	3.0	7.7	2.57
2H-4, 20–20	11.90	3.0	7.5	2.50
2H-4, 70–70	12.40	3.0	7.5	2.50
2H-4, 120–120	12.90	3.0	7.8	2.60
2H-5, 20–20	13.40	3.0	8.2	2.73
2H-5, 70–70	13.90	3.0	7.8	2.60
2H-5, 120–120	14.40	3.0	7.9	2.63
2H-6, 20–20	14.90	3.0	8.4	2.80
2H-6, 70–70	15.40	3.0	8.6	2.87
2H-6, 120–120	15.90	3.0	9.0	3.00
3H-1, 30–30	17.00	3.0	9.9	3.30
3H-1, 70–70	17.40	3.0	10.1	3.37
3H-1, 120–120	17.90	3.0	9.1	3.03
3H-2, 20–20	18.40	3.0	10.2	3.40
3H-2, 70–70	18.90	3.0	9.7	3.23
3H-2, 120–120	19.40	3.0	9.3	3.10
3H-3, 20–20	19.90	3.0	9.5	3.17
3H-3, 70–70	20.40	3.0	9.8	3.27
3H-3, 120–120	20.90	3.0	9.2	3.07
3H-4, 25–25	21.45	3.0	9.4	3.13
3H-4, 70–70	21.90	3.0	9.8	3.27
3H-4, 120–120	22.40	3.1	9.8	3.16
3H-5, 20–20	22.90	3.1	9.6	3.10
3H-5, 70–70	23.40	3.1	9.4	3.03
3H-5, 120–120	23.90	3.1	9.3	3.00
3H-6, 25–25	24.45	3.1	9.2	2.97
3H-6, 65–65	24.85	3.1	9.3	3.00
3H-6, 125–125	25.45	3.1	9.4	3.03
4H-1, 25–25	26.45	3.1	9.2	2.97
4H-1, 65–65	26.85	3.1	9.9	3.19
4H-1, 125–125	27.45	3.1	9.6	3.10
4H-2, 25–25	27.95	3.1	9.6	3.10
4H-2, 65–65	28.35	3.1	9.4	3.03
4H-2, 125–125	28.95	3.1	9.3	3.00
4H-3, 25–25	29.45	3.1	9.7	3.13
4H-3, 65–65	29.85	3.1	9.2	2.97
4H-3, 125–125	30.45	3.1	8.3	2.68
4H-4, 25–25	30.95	3.1	8.1	2.61
4H-4, 65–65	31.35	3.1	8.0	2.58
4H-4, 125–125	31.95	3.1	8.1	2.61
4H-5, 25–25	32.45	3.0	10.0	3.33
4H-5, 65–65	32.85	3.0	12.5	4.17
4H-6, 65–65	34.35	3.0	9.9	3.30
4H-6, 125–125	34.95	3.0	10.2	3.40
5H-1, 25–25	35.95	3.0	11.1	3.70
5H-1, 65–65	36.35	3.0	12.4	4.13
5H-1, 125–125	36.95	3.0	9.8	3.27
5H-2, 25–25	37.45	3.0	9.9	3.30
5H-2, 65–65	37.85	3.0	10.3	3.43
5H-2, 125–125	38.45	3.0	10.1	3.37
5H-3, 25–25	38.95	3.0	10.3	3.43
5H-3, 65–65	39.35	3.0	10.5	3.50
5H-3, 125–125	39.95	3.0	10.8	3.60
5H-4, 25–25	40.45	3.0	10.7	3.57
5H-4, 65–65	40.85	3.0	10.5	3.50
5H-4, 125–125	41.45	3.0	10.6	3.53
5H-5, 25–25	41.95	3.0	10.5	3.50
5H-5, 65–65	42.35	3.0	10.3	3.43
5H-5, 125–125	42.95	3.0	10.2	3.40
5H-6, 25–25	43.45	3.0	10.1	3.37
5H-6, 65–65	43.85	3.0	10.2	3.40
5H-6, 125–125	44.45	3.0	10.3	3.43
6H-1, 25–25	45.45	3.1	10.4	3.35
6H-1, 65–65	45.85	3.1	9.6	3.10
6H-1, 125–125	46.45	3.1	9.7	3.13
6H-2, 25–25	46.95	3.1	9.5	3.06
6H-2, 65–65	47.35	3.1	9.7	3.13
6H-2, 125–125	47.95	3.1	9.6	3.10
6H-3, 25–25	48.45	3.1	10.2	3.29
6H-3, 65–65	48.85	3.1	10.2	3.29
6H-3, 125–125	49.45	3.1	10.5	3.39
6H-4, 25–25	49.95	3.1	10.8	3.48
6H-4, 65–65	50.35	3.1	9.7	3.13
6H-4, 125–125	50.95	3.1	10.1	3.26
6H-5, 25–25	51.45	3.1	10.7	3.45
6H-5, 65–65	51.85	3.1	9.6	3.10
6H-5, 125–125	52.45	3.1	10.4	3.35
6H-6, 25–25	52.95	3.1	10.1	3.26
6H-6, 65–65	53.35	3.1	9.7	3.13
6H-6, 125–125	53.95	3.1	10.8	3.48
7H-1, 25–25	54.95	3.1	10.5	3.39
7H-1, 65–65	55.35	3.1	10.5	3.39
7H-1, 125–125	55.95	3.1	10.3	3.32
7H-2, 25–25	56.45	3.1	10.7	3.45
7H-2, 65–65	56.85	3.1	10.5	3.39
7H-2, 125–125	57.45	3.1	10.5	3.39
7H-3, 25–25	57.95	3.1	10.9	3.52
7H-3, 65–65	58.35	3.1	10.4	3.35
7H-3, 125–125	58.95	3.1	10.9	3.52
7H-4, 25–25	59.45	3.1	10.5	3.39
7H-4, 65–65	59.85	3.1	9.9	3.19
7H-4, 125–125	60.45	3.1	9.6	3.10
7H-5, 25–25	60.95	3.1	9.9	3.19
7H-5, 65–65	61.35	3.1	9.5	3.06
8H-1, 25–25	64.45	3.1	10.6	3.42
8H-1, 65–65	64.85	3.1	10.5	3.39
8H-1, 125–125	65.45	3.1	10.6	3.42
8H-2, 25–25	65.95	3.1	10.3	3.32
8H-2, 65–65	66.35	3.1	10.1	3.26
8H-2, 125–125	66.95	3.1	11.4	3.68
8H-3, 25–25	67.45	3.1	12.0	3.87
8H-3, 65–65	67.85	3.1	11.9	3.84
8H-3, 125–125	68.45	3.1	11.9	3.84
8H-4, 25–25	68.95	3.1	11.8	3.81
8H-4, 65–65	69.35	3.1	11.8	3.81
8H-4, 125–125	69.95	3.1	12.8	4.13
8H-5, 25–25	70.45	3.1	12.1	3.90
8H-5, 65–65	70.85	3.1	11.8	3.81
8H-5, 125–125	71.45	3.1	13.5	4.35
8H-6, 25–25	71.95	3.1	11.7	3.77
8H-6, 65–65	72.35	3.1	10.7	3.45
8H-6, 125–125	72.95	3.1	11.0	3.55
9H-1, 25–25	73.95	3.1	10.7	3.45
9H-1, 65–65	74.35	3.1	11.7	3.77
9H-1, 125–125	74.95	3.1	10.8	3.48
9H-2, 25–25	75.45	3.1	10.9	3.52
9H-2, 65–65	75.85	3.1	10.7	3.45
9H-2, 125–125	76.45	3.1	10.3	3.32
9H-3, 25–25	76.95	3.1	10.7	3.45
9H-3, 65–65	77.35	3.1	10.8	3.48
9H-4, 25–25	78.45	3.1	12.0	3.87
9H-4, 65–65	78.85	3.1	11.8	3.81
9H-4, 125–125	79.45	3.1	11.0	3.55
9H-6, 25–25	81.45	3.1	13.8	4.45
9H-6, 65–65	81.85	3.1	13.4	4.32
9H-6, 120–120	82.40	3.1	11.0	3.55
10H-1, 25–25	83.45	3.1	11.4	3.68
10H-1, 65–65	83.85	3.1	12.1	3.90
10H-1, 125–125	84.45	3.1	10.7	3.45
10H-2, 25–25	84.95	3.1	10.6	3.42
10H-2, 65–65	85.35	3.1	9.8	3.16
10H-2, 125–125	85.95	3.1	11.4	3.68
10H-3, 25–25	86.45	3.1	10.1	3.26
10H-3, 65–65	86.85	3.1	10.4	3.35
10H-3, 125–125	87.45	3.1	10.2	3.29
10H-4, 25–25	87.95	3.1	12.5	4.03
10H-4, 65–65	88.35	3.1	12.1	3.90
10H-4, 125–125	88.95	3.1	11.1	3.58
10H-5, 25–25	89.45	3.1	12.2	3.94
10H-5, 65–65	89.85	3.1	10.6	3.42
10H-5, 125–125	90.45	3.1	10.7	3.45
10H-6, 25–25	90.95	3.1	11.7	3.77

Table 9 (continued).

Core, section, interval (cm)	Depth (mbsf)	Seawater (ohms)	Sample (ohms)	Formation factor
10H-6, 65–65	91.35	3.1	11.6	3.74
10H-6, 125–125	91.95	3.1	12.8	4.13
11H-1, 25–25	92.95	3.1	11.2	3.61
11H-1, 65–65	93.35	3.1	12.7	4.10
11H-1, 125–125	93.95	3.1	11.6	3.74
11H-2, 25–25	94.45	3.1	12.2	3.94
11H-2, 65–65	94.85	3.1	11.6	3.74
11H-2, 125–125	95.45	3.1	12.6	4.06
11H-3, 25–25	95.95	3.1	11.9	3.84
11H-3, 65–65	96.35	3.1	12.2	3.94
11H-3, 125–125	96.95	3.0	14.1	4.70
11H-4, 25–25	97.45	3.0	13.9	4.63
11H-4, 65–65	97.85	3.0	15.8	5.27
11H-4, 125–125	98.45	3.0	12.5	4.17
11H-5, 25–25	98.95	3.0	15.4	5.13
11H-5, 65–65	99.35	3.0	15.0	5.00
11H-5, 125–125	99.95	3.0	14.6	4.87
11H-6, 25–25	100.45	3.0	14.9	4.97
11H-6, 65–65	100.85	3.0	14.7	4.90
11H-6, 125–125	101.45	3.0	13.2	4.40
12H-1, 25–25	102.45	3.0	11.6	3.87
12H-1, 65–65	102.85	3.0	14.2	4.73
12H-1, 125–125	103.45	3.0	11.2	3.73
12H-2, 25–25	103.95	3.0	16.4	5.47
12H-2, 65–65	104.35	3.0	12.6	4.20
12H-2, 125–125	104.95	3.4	17.0	5.00
12H-3, 25–25	105.45	3.4	9.8	2.88
12H-3, 65–65	105.85	3.4	11.7	3.44
12H-3, 125–125	106.45	3.4	12.7	3.74
12H-4, 25–25	106.95	3.4	14.2	4.18
12H-4, 65–65	107.35	3.4	11.8	3.47
12H-4, 125–125	107.95	3.4	10.4	3.06
12H-5, 25–25	108.45	3.4	11.8	3.47
12H-5, 65–65	108.85	3.4	11.5	3.38
12H-5, 125–125	109.45	3.4	12.4	3.65
12H-6, 25–25	109.95	3.4	13.7	4.03
12H-6, 65–65	110.35	3.4	11.9	3.50
12H-6, 125–125	110.95	3.4	13.7	4.03
12H-7, 25–25	111.45	3.4	15.5	4.56
12H-7, 65–65	111.85	3.4	12.7	3.74
13H-1, 25–25	111.95	3.4	11.9	3.50
13H-1, 65–65	112.35	3.4	11.9	3.50
13H-1, 125–125	112.95	3.4	15.0	4.41
13H-2, 25–25	113.45	3.4	12.5	3.68
13H-2, 65–65	113.85	3.4	12.3	3.62
13H-2, 125–125	114.45	3.4	13.6	4.00
13H-3, 25–25	114.95	3.4	14.0	4.12
13H-3, 65–65	115.35	3.4	19.0	5.59
13H-3, 125–125	115.95	3.4	14.0	4.12
13H-4, 25–25	116.45	3.4	19.4	5.71
13H-4, 65–65	116.85	3.4	13.9	4.09
13H-4, 125–125	117.45	3.4	11.8	3.47
13H-5, 25–25	117.95	3.4	19.4	5.71
13H-5, 65–65	118.35	3.4	15.1	4.44
13H-5, 125–125	118.95	3.4	13.1	3.85
13H-6, 25–25	119.45	3.4	17.4	5.12
13H-6, 65–65	119.85	3.4	14.2	4.18
13H-6, 125–125	120.45	3.4	15.8	4.65
14H-1, 25–25	121.45	3.4	14.3	4.21
14H-1, 65–65	121.85	3.4	14.2	4.18
14H-1, 125–125	122.45	3.4	15.0	4.41
14H-2, 65–65	123.35	3.4	14.2	4.18
14H-3, 25–25	124.00	3.4	17.5	5.15
14H-3, 65–65	124.40	3.4	16.1	4.74
14H-3, 125–125	125.00	3.4	12.5	3.68
14H-4, 25–25	125.00	3.4	12.7	3.74
14H-4, 65–65	125.90	3.4	13.2	3.88
14H-5, 25–25	126.26	3.4	12.1	3.56
14H-5, 65–65	126.66	3.4	12.5	3.68
14H-5, 125–125	127.26	3.4	15.6	4.59
15H-1, 25–25	130.95	3.4	12.1	3.56
15H-1, 65–65	131.35	3.4	11.3	3.32
15H-1, 125–125	131.95	3.4	11.9	3.50
15H-2, 25–25	132.45	3.3	16.3	4.94
15H-2, 65–65	132.85	3.3	16.2	4.91
15H-2, 125–125	133.45	3.3	14.0	4.24
15H-3, 25–25	133.95	3.3	15.5	4.70
15H-3, 65–65	134.35	3.3	13.6	4.12
15H-3, 125–125	134.95	3.3	12.7	3.85
15H-4, 25–25	135.45	3.3	21.4	6.48
15H-4, 65–65	135.85	3.3	17.7	5.36
15H-4, 125–125	136.45	3.3	15.5	4.70
15H-5, 25–25	136.95	3.3	14.8	4.48

Table 9 (continued).

Core, section, interval (cm)	Depth (mbsf)	Seawater (ohms)	Sample (ohms)	Formation factor
15H-5, 65–65	137.35	3.3	14.3	4.33
15H-5, 125–125	137.95	3.3	12.5	3.79
15H-6, 25–25	138.45	3.3	10.4	3.15
15H-6, 65–65	138.85	3.3	11.6	3.52
15H-6, 125–125	139.45	3.3	12.7	3.85
15H-7, 25–25	139.45	3.3	16.4	4.97
16V-1, 25–25	140.45	3.3	13.2	4.00
16V-1, 65–65	140.85	3.3	13.9	4.21
16V-1, 125–125	141.45	3.3	14.5	4.39
133-820B-				
14H-1, 25–25	122.45	3.1	13.9	4.48
14H-1, 65–65	122.85	3.1	15.2	4.90
14H-1, 125–125	123.45	3.1	12.9	4.16
14H-2, 125–125	124.95	3.1	9.7	3.13
14H-3, 25–25	125.45	3.1	11.1	3.58
14H-3, 65–65	125.85	3.1	12.6	4.06
14H-3, 125–125	126.45	3.1	14.3	4.61
14H-4, 25–25	126.95	3.1	13.6	4.39
14H-4, 65–65	127.35	3.1	18.7	6.03
14H-4, 125–125	127.95	3.1	13.4	4.32
14H-5, 25–25	128.45	3.1	16.5	5.32
14H-5, 65–65	128.85	3.1	16.2	5.23
14H-5, 125–125	129.45	3.1	15.6	5.03
14H-6, 25–25	129.95	3.1	13.5	4.35
14H-6, 65–65	130.35	3.1	12.8	4.13
14H-6, 125–125	130.95	3.1	14.6	4.71
15H-1, 25–25	131.95	3.1	10.8	3.48
15H-1, 65–65	132.35	3.1	13.3	4.29
15H-1, 125–25	132.95	3.1	14.6	4.71
15H-2, 25–25	133.45	3.1	13.9	4.48
15H-2, 65–65	133.85	3.1	16.4	5.29
15H-2, 125–125	134.45	3.1	15.5	5.00
15H-3, 25–25	134.95	3.1	13.1	4.23
15H-3, 65–65	135.35	3.1	16.7	5.39
15H-3, 125–125	135.95	3.1	13.1	4.23
15H-4, 25–25	136.45	3.1	14.8	4.77
15H-4, 65–65	136.85	3.1	14.8	4.77
15H-4, 125–125	137.45	3.1	12.1	3.90
15H-5, 25–25	137.95	3.1	17.3	5.58
15H-5, 65–65	138.35	3.1	17.6	5.68
15H-5, 125–125	138.95	3.1	21.0	6.77
15H-6, 25–25	139.45	3.1	14.6	4.71
15H-6, 65–65	139.85	3.1	15.0	4.84
15H-6, 125–125	140.45	3.1	13.8	4.45
16H-1, 25–25	141.45	3.1	15.7	5.06
16H-1, 65–65	141.85	3.1	12.4	4.00
16H-1, 125–125	142.45	3.1	14.5	4.68
16H-2, 25–25	142.95	3.1	13.8	4.45
16H-2, 65–65	143.35	3.1	12.8	4.13
16H-2, 125–125	143.95	3.1	14.4	4.65
17H-1, 25–25	150.95	3.1	13.2	4.26
17H-1, 125–125	151.95	3.1	14.0	4.52
17H-2, 25–25	152.45	3.1	13.0	4.19
17H-2, 65–65	152.85	3.1	12.4	4.00
17H-2, 125–125	153.45	3.1	20.0	6.45
17H-3, 25–25	153.95	3.1	17.7	5.71
17H-3, 65–65	154.35	3.1	12.3	3.97
17H-4, 25–25	155.45	3.1	21.5	6.94
17H-4, 65–65	155.85	3.1	16.7	5.39
17H-4, 125–125	156.45	3.1	16.8	5.42
18X-1, 25–25	160.45	3.1	10.9	3.52
18X-1, 65–65	160.85	3.1	11.9	3.84
18X-1, 125–125	161.45	3.1	12.3	3.97
18X-2, 25–25	161.95	3.1	13.5	4.35
18X-2, 65–65	162.35	3.1	12.3	3.97
18X-2, 125–125	162.95	3.1	12.3	3.97
18X-3, 25–25	163.45	3.1	12.4	4.00
18X-3, 65–65	163.85	3.1	13.2	4.26
18X-3, 125–125	164.45	3.1	12.6	4.06
18X-4, 25–25	164.95	3.1	14.1	4.55
18X-4, 65–65	165.35	3.1	13.5	4.35
18X-4, 125–125	165.95	3.1	13.5	4.35
19X-1, 115–115	166.35	3.0	13.5	4.50
18X-5, 25–25	166.45	3.1	12.7	4.10
18X-5, 65–65	166.85	3.1	10.7	3.45
18X-5, 125–125	167.45	3.1	12.9	4.16
19X-2, 115–115	167.85	3.0	14.7	4.90
18X-6, 25–25	167.95	3.1	14.7	4.74
18X-6, 65–65	168.35	3.1	14.9	4.81
18X-6, 125–125	168.95	3.1	15.1	4.87
19X-3, 90–90	169.10	3.0	13.6	4.53
19X-4, 100–100	170.70	3.0	13.8	4.60

Table 9 (continued).

Core, section, interval (cm)	Depth (mbsf)	Seawater (ohms)	Sample (ohms)	Formation factor
19X-5, 100–100	172.20	3.0	14.1	4.70
19X-6, 65–65	173.35	3.0	14.2	4.73
19X-6, 130–130	174.00	3.0	16.5	5.50
20X-1, 25–25	175.05	3.0	12.7	4.23
20X-1, 65–65	175.45	3.0	14.2	4.73
20X-1, 125–125	176.05	3.0	12.9	4.30
20X-2, 25–25	176.55	3.0	14.0	4.67
20X-2, 65–65	176.95	3.0	14.9	4.97
20X-2, 125–125	177.55	3.0	15.1	5.03
20X-3, 25–25	178.05	3.0	14.6	4.87
20X-3, 65–65	178.45	3.0	14.8	4.93
20X-3, 125–125	179.05	3.0	12.2	4.07
20X-4, 25–25	179.55	3.0	15.1	5.03
20X-4, 65–65	179.95	3.0	10.7	3.57
20X-4, 125–125	180.55	3.0	13.6	4.53
20X-5, 85–85	181.65	3.0	11.2	3.73
20X-6, 48–48	182.78	3.0	13.2	4.40
20X-6, 120–120	183.50	3.0	13.5	4.50
21X-3, 25–25	187.35	3.2	13.5	4.22
21X-3, 65–65	187.75	3.2	13.8	4.31
21X-3, 125–125	188.35	3.2	14.3	4.47
21X-4, 25–25	188.85	3.2	15.6	4.88
21X-4, 65–65	189.25	3.2	15.8	4.94
21X-4, 125–125	189.85	3.2	14.2	4.44
21X-5, 25–25	190.35	3.2	14.9	4.66
21X-5, 65–65	190.75	3.2	16.1	5.03
21X-5, 125–125	191.35	3.2	18.3	5.72
21X-6, 25–25	191.85	3.2	15.0	4.69
21X-6, 65–65	192.25	3.2	15.3	4.78
21X-6, 125–125	192.85	3.2	15.3	4.78
22X-1, 25–25	193.95	3.1	11.2	3.61
22X-1, 65–65	194.35	3.1	11.6	3.74
22X-1, 125–125	194.95	3.1	11.4	3.68
22X-2, 25–25	195.45	3.1	12.2	3.94
22X-2, 65–65	195.85	3.1	12.7	4.10
22X-2, 125–125	196.45	3.1	12.6	4.06
22X-3, 25–25	196.95	3.1	12.6	4.06
22X-3, 65–65	197.35	3.1	12.8	4.13
22X-3, 125–125	197.95	3.1	13.4	4.32
22X-4, 25–25	198.45	3.1	12.0	3.87
22X-4, 65–65	198.85	3.1	12.2	3.94
22X-4, 125–125	199.45	3.1	11.8	3.81
22X-5, 25–25	199.95	3.1	12.7	4.10
22X-5, 65–65	200.35	3.1	12.4	4.00
22X-5, 125–125	200.95	3.1	14.2	4.58
22X-6, 25–25	201.45	3.1	17.2	5.55
22X-6, 65–65	201.85	3.1	13.9	4.48
22X-6, 125–125	202.45	3.1	13.7	4.42
23X-1, 25–25	203.65	3.1	13.9	4.48
23X-1, 65–65	204.05	3.1	15.9	5.13
23X-1, 125–125	204.65	3.1	12.8	4.13
23X-2, 25–25	205.15	3.1	13.3	4.29
23X-2, 65–65	205.55	3.1	13.8	4.45
23X-2, 125–125	206.15	3.1	15.3	4.94
23X-3, 25–25	206.65	3.1	15.0	4.84
23X-3, 65–65	207.05	3.1	15.6	5.03
23X-3, 125–125	207.65	3.1	13.2	4.26
23X-4, 25–25	208.15	3.1	13.8	4.45
23X-4, 75–75	208.65	3.1	12.2	3.94
23X-4, 130–130	209.20	3.1	15.7	5.06
23X-5, 25–25	209.65	3.1	14.0	4.52
23X-5, 65–65	210.05	3.1	12.6	4.06
23X-6, 25–25	211.05	3.1	15.9	5.13
23X-6, 65–65	211.45	3.1	14.3	4.61
23X-6, 120–120	212.00	3.1	14.3	4.61
24X-1, 20–20	213.00	3.1	14.1	4.55
24X-1, 70–70	213.50	3.1	12.9	4.16
24X-1, 120–120	214.00	3.1	14.1	4.55
24X-2, 20–20	214.50	3.1	13.9	4.48
24X-2, 70–70	215.00	3.1	14.5	4.68
24X-3, 70–70	216.50	3.1	14.5	4.68
24X-3, 120–120	217.00	3.1	14.5	4.68
24X-4, 20–20	217.50	3.1	16.5	5.32
24X-4, 70–70	218.00	3.1	16.8	5.42
24X-4, 120–120	218.50	3.1	13.8	4.45
24X-5, 20–20	219.00	3.1	12.8	4.13
24X-5, 70–70	219.50	3.1	17.2	5.55
24X-5, 120–120	220.00	3.1	14.2	4.58
24X-6, 20–20	220.50	3.1	14.4	4.65
24X-6, 70–70	221.00	3.1	15.5	5.00
24X-6, 120–120	221.50	3.1	16.4	5.29
25X-1, 60–60	223.10	3.0	13.9	4.63

Table 9 (continued).

Core, section, interval (cm)	Depth (mbsf)	Seawater (ohms)	Sample (ohms)	Formation factor
25X-1, 128–128	223.78	3.0	16.8	5.60
25X-2, 20–20	224.20	3.0	13.7	4.57
25X-2, 80–80	224.80	3.0	12.7	4.23
25X-3, 20–20	225.70	3.0	17.3	5.77
25X-3, 70–70	226.20	3.0	14.0	4.67
25X-3, 140–140	226.90	3.0	14.7	4.90
26X-1, 70–70	232.80	3.0	15.6	5.20
26X-1, 120–120	233.30	3.0	14.2	4.73
27X-1, 120–120	243.00	3.0	11.1	3.70
27X-2, 20–20	243.50	3.0	14.8	4.93
27X-2, 70–70	244.00	3.0	13.8	4.60
27X-2, 120–120	244.50	3.0	14.3	4.77
27X-3, 20–20	245.00	3.0	16.0	5.33
27X-3, 70–70	245.50	3.0	13.3	4.43
27X-3, 120–120	246.00	3.0	14.7	4.90
27X-4, 20–20	246.50	3.0	15.2	5.07
27X-4, 70–70	247.00	3.0	16.8	5.60
27X-4, 120–120	247.50	3.0	18.3	6.10
27X-5, 28–28	248.08	3.0	13.5	4.50
27X-5, 120–120	249.00	3.0	14.0	4.67
28X-1, 20–20	251.30	3.0	13.7	4.57
28X-1, 70–70	251.80	3.0	13.7	4.57
28X-1, 120–120	252.30	3.0	17.9	5.97
28X-2, 20–20	252.80	3.0	14.2	4.73
28X-2, 70–70	253.80	3.0	13.7	4.57
28X-2, 120–120	253.80	3.0	14.9	4.97
28X-3, 20–20	254.30	3.0	14.9	4.97
28X-3, 70–70	254.80	3.0	19.3	6.43
28X-3, 120–120	255.30	3.0	15.0	5.00
28X-4, 20–20	255.80	3.0	15.2	5.07
28X-4, 120–120	256.80	3.0	16.7	5.57
28X-5, 20–20	257.30	3.0	15.3	5.10
28X-5, 70–70	257.80	3.0	16.6	5.53
28X-6, 20–20	258.80	3.0	14.1	4.70
28X-6, 70–70	259.30	3.0	13.3	4.43
28X-6, 120–120	259.80	3.0	11.2	3.73
30X-1, 20–20	270.60	3.0	16.0	5.33
30X-1, 70–70	271.10	3.0	19.9	6.63
30X-1, 120–120	271.60	3.0	18.5	6.17
31X-1, 20–20	280.30	3.0	17.9	5.93
33X-1, 20–20	299.60	3.0	15.3	5.10
33X-1, 70–70	300.10	3.0	17.8	5.93
33X-1, 120–120	300.60	3.0	19.5	6.50
33X-2, 20–20	301.10	3.0	16.0	5.33
33X-2, 70–70	301.60	3.0	15.4	5.13
33X-2, 120–120	302.10	3.0	16.1	5.37
33X-3, 20–20	302.60	3.0	13.7	4.57
33X-3, 70–70	303.10	3.0	15.2	5.07
33X-3, 120–120	303.60	3.0	15.0	5.00
33X-4, 20–20	304.10	3.0	14.2	4.73
33X-4, 70–70	304.60	3.0	14.2	4.73
33X-4, 120–120	305.10	3.0	14.1	4.70
33X-5, 20–20	305.60	3.0	13.6	4.53
33X-5, 70–70	306.10	3.0	14.5	4.83
33X-5, 120–120	306.60	3.0	15.5	5.17
36X-1, 40–40	328.90	2.9	23.1	7.97
36X-1, 70–70	329.20	2.9	15.8	5.45
36X-1, 120–120	329.70	2.9	19.7	6.79
36X-2, 70–70	330.70	3.0	16.7	5.57
36X-2, 120–120	331.20	3.0	18.2	6.07
36X-3, 20–20	331.70	2.9	18.5	6.38
36X-3, 70–70	332.20	2.9	17.6	6.07
36X-3, 120–120	332.70	2.9	18.2	6.28
36X-4, 10–10	333.10	2.9	18.9	6.52
36X-4, 90–90	333.90	2.9	18.7	6.45
36X-5, 9–9	334.59	2.9	19.1	6.59
36X-5, 120–120	335.70	2.9	16.8	5.79
36X-6, 42–42	336.42	2.9	16.8	5.79
36X-6, 90–90	336.90	2.9	15.4	5.31
37X-1, 20–20	338.40	2.9	16.7	5.76
37X-1, 70–70	338.90	2.9	17.7	6.10
37X-1, 120–120	339.40	2.9	17.0	5.86
37X-2, 20–20	339.90	2.9	17.4	6.00
37X-2, 70–70	340.40	2.9	16.8	5.79
37X-2, 120–120	340.90	2.9	17.3	5.97
37X-3, 20–20	341.40	2.9	17.6	6.07
37X-3, 70–70	341.90	2.9	16.9	5.83
37X-3, 120–120	342.40	2.9	18.6	6.41
37X-4, 20–20	342.90	2.9	17.3	5.97
37X-4, 70–70	343.40	2.9	16.3	5.62
37X-4, 134–134	344.04	2.9	16.4	5.66

Table 10. Vane shear strength data, Hole 820A.

Core, section, interval (cm)	Depth (mbsf)	Spring number	Torque (degrees)	Strain (degrees)	Shear strength (kPa)
133-820A-					
1H-1, 92–93	0.92	1	23	18	4.9
1H-2, 92–93	2.42	1	33	21	7.0
1H-3, 92–93	3.92	1	47	22	10.0
1H-4, 92–93	5.42	1	31	15	6.6
1H-5, 52–53	6.52	1	37	13	7.9
2H-1, 92–93	8.12	1	28	24	8.1
2H-2, 92–93	9.62	1	46	17	9.8
2H-3, 92–93	11.12	1	70	14	14.9
2H-4, 92–93	12.62	1	58	17	12.3
2H-5, 92–93	14.12	1	76	18	16.1
2H-6, 92–93	15.62	1	72	22	15.3
3H-1, 92–93	17.62	1	35	22	7.4
3H-2, 92–93	19.12	1	54	23	11.5
3H-3, 92–93	20.62	1	81	20	17.2
3H-4, 92–93	22.12	1	85	20	18.0
3H-5, 92–93	22.12	1	85	20	20.2
3H-6, 92–93	25.12	1	137	20	29.1
4H-1, 92–93	27.12	4	18	8	21.4
4H-2, 92–93	28.62	4	16	11	19.0
4H-3, 92–93	30.12	4	20	11	23.8
4H-4, 92–93	31.62	4	29	9	34.5
4H-5, 92–93	33.12	4	10	14	11.9
4H-6, 92–93	34.62	4	16	15	19.0
5H-1, 92–93	36.62	4	21	13	25.0
5H-2, 92–93	38.12	4	20	19	23.8
5H-3, 92–93	39.62	4	20	15	23.8
5H-4, 92–93	41.12	4	36	19	42.8
5H-5, 92–93	42.62	4	46	20	54.7
5H-6, 92–93	44.12	4	38	15	45.2
6H-1, 92–93	46.12	4	32	12	38.1
6H-2, 92–93	47.62	4	42	11	50.0
6H-3, 92–93	49.12	4	47	12	55.9
6H-4, 92–93	50.62	4	45	14	53.5
6H-6, 92–93	53.62	4	18	17	21.4
6H-7, 38–39	54.58	4	44	14	52.3
7H-1, 38–39	55.08	4	50	12	59.5
7H-2, 93–94	57.13	4	60	11	71.4
7H-3, 93–94	58.63	4	62	13	73.7
7H-4, 93–94	60.13	4	62	12	73.7
7H-5, 93–94	61.63	4	50	9	59.5
7H-6, 93–94	63.13	4	60	8	71.4
8H-1, 93–94	65.13	4	10	10	11.9
8H-2, 93–94	66.63	4	28	20	33.3
8H-3, 93–94	68.13	4	48	17	57.1
8H-4, 93–94	69.63	4	39	16	46.4
8H-5, 93–94	71.13	4	45	17	53.5
8H-6, 93–94	72.63	4	64	17	76.1
9H-1, 93–94	74.63	4	49	19	58.3
9H-2, 93–94	76.13	4	60	18	71.4
9H-3, 93–94	77.63	4	64	13	76.1
9H-4, 93–94	79.13	4	18	16	21.4
9H-6, 93–94	82.13	4	17	13	20.2
10H-1, 93–94	84.13	4	19	8	22.6
10H-2, 93–94	85.63	4	15	11	17.8
10H-3, 93–94	87.13	4	25	10	29.7
10H-4, 93–94	88.63	4	76	13	90.4
10H-5, 93–94	90.13	4	32	13	38.1
10H-6, 93–94	91.63	4	17	10	20.2
11H-1, 93–94	93.63	4	49	13	58.3
11H-2, 93–94	95.13	4	40	14	47.6
11H-3, 93–94	96.63	4	32	12	38.1
11H-4, 93–94	98.13	4	38	20	45.2
11H-5, 93–94	99.63	4	45	15	53.5
11H-6, 93–94	101.13	4	43	18	51.1

Table 11. Thermal conductivity at Site 820.

Core, section, interval (cm)	Depth (mbsf)	Probe number	Thermal conductivity (W/m·K)	Standard error (W/m·K)	Calculated drift (W/m·K)
133-820B-					
1H-2, 60–60	2.10	2	0.6635	0.00727	−0.10578
1H-2, 60–60	2.10	32	0.9539	0.00524	−0.01324
1H-3, 60–60	3.60	3	1.0077	0.00523	−0.00592
1H-3, 60–60	3.60	3	0.9790	0.00553	−0.00996
1H-5, 60–60	6.60	14	0.9940	0.00474	0.00867
1H-5, 60–60	6.60	14	1.0550	0.00636	0.02339
1H-6, 30–30	7.80	150	0.7750	0.00558	−0.07772
1H-6, 30–30	7.80	150	0.7741	0.00250	−0.07550
2H-2, 70–70	10.40	32	0.9791	0.00777	−0.02944
2H-3, 70–70	11.90	3	1.0820	0.00808	0.00641
2H-5, 70–70	14.90	14	1.1244	0.00541	0.03722
2H-6, 70–70	16.40	150	1.0645	0.00558	0.00172
3H-2, 70–70	19.90	32	1.0635	0.00750	−0.00537
3H-3, 70–70	21.40	3	0.9696	0.00636	−0.00823
3H-5, 70–70	24.40	14	1.1239	0.00687	0.03300
3H-6, 70–70	25.90	150	1.0602	0.00674	0.00797
4H-2, 70–70	29.40	32	1.0533	0.00726	0.00023
4H-3, 70–70	30.90	3	1.0824	0.00907	0.01818
4H-5, 70–70	33.90	14	1.1298	0.00614	0.02648
4H-6, 70–70	35.40	150	1.0807	0.00609	−0.00340
5H-2, 70–70	38.90	32	1.0566	0.00656	−0.03682
5H-3, 70–70	40.40	3	1.1629	0.00794	0.00399
5H-5, 70–70	43.40	14	1.2039	0.00648	0.02796
5H-6, 70–70	44.90	150	1.1223	0.00610	−0.00008
6H-2, 70–70	48.40	32	1.0511	0.00448	−0.02126
6H-3, 70–70	49.90	3	1.1257	0.00758	−0.01048
6H-5, 70–70	52.90	14	1.1696	0.00587	0.02699
6H-6, 70–70	54.40	150	1.0647	0.00440	−0.01899
7H-2, 70–70	57.90	32	1.1645	0.00737	−0.00430
7H-3, 70–70	59.40	3	1.1330	0.00561	−0.00251
7H-5, 70–70	62.40	14	1.2943	0.00398	0.05552
7H-6, 70–70	63.90	150	1.0954	0.00531	0.00006
8H-2, 70–70	67.40	32	1.0821	0.00923	−0.03162
8H-3, 70–70	68.90	3	1.1797	0.00909	−0.01065
8H-5, 70–70	71.90	14	1.2515	0.00552	0.04157
8H-6, 70–70	73.40	150	1.0896	0.00773	−0.00695
9H-2, 84–84	77.04	32	1.1219	0.00754	0.00110
9H-3, 84–84	78.54	3	1.1979	0.00690	0.00800
9H-5, 84–84	81.54	14	1.2853	0.00855	0.05272
9H-6, 84–84	83.04	150	1.2502	0.00662	0.01050
10H-2, 38–38	86.08	32	1.1645	0.00330	−0.00072
10H-3, 38–38	87.58	3	1.2746	0.00476	0.00955
10H-5, 38–38	90.58	14	1.1854	0.00424	0.04063
10H-6, 38–38	92.08	150	1.2171	0.00547	0.00695
11H-2, 81–81	96.01	32	1.1697	0.00487	−0.00715
11H-3, 76–76	97.46	3	1.1348	0.00482	−0.00006
11H-5, 53–53	100.23	14	1.2384	0.00574	0.04553
11H-6, 60–60	101.80	150	1.1852	0.00422	−0.01552
12H-2, 82–82	105.52	32	1.1444	0.00662	−0.00497
12H-3, 95–95	107.15	3	1.2183	0.00649	−0.02129
12H-5, 56–56	109.76	14	1.0697	0.00777	−0.00423
12H-6, 54–54	111.24	150	1.2602	0.00643	0.01468
13H-2, 85–85	115.05	32	1.1858	0.00570	0.00579
13H-3, 90–90	116.60	3	1.0971	0.00614	−0.00366
13H-5, 65–65	119.35	14	1.3029	0.00545	0.04057
13H-6, 65–65	120.85	150	1.2302	0.00617	0.02437
14H-2, 100–100	124.70	32	1.1700	0.00735	−0.02158
14H-3, 100–100	126.20	3	1.3141	0.00569	0.02148
14H-5, 100–100	129.20	14	1.3285	0.00679	0.02626
14H-6, 106–106	130.76	150	1.1495	0.00726	0.00760
15H-3, 101–101	135.71	32	1.1439	0.00397	−0.01725
15H-4, 99–99	137.19	3	1.1527	0.01001	−0.02469
15H-6, 80–80	140.00	14	1.2106	0.00559	0.02596
15H-6, 101–101	140.21	150	1.4148	0.00647	0.03476
16H-3, 64–64	144.84	32	0.9884	0.00446	0.01298
16H-4, 64–64	146.34	3	1.0628	0.01156	0.04351
28X-2, 60–60	253.20	32	1.2249	0.00490	−0.,01869
28X-3, 128–128	255.38	3	1.2364	0.00784	0.00276
28X-5, 43–43	257.53	14	1.3486	0.00651	0.02862
28X-6, 60–60	259.20	150	1.2975	0.00660	−0.00717
29X-1, 60–60	261.40	32	0.9530	0.00532	−0.07808
29X-2, 60–60	262.90	3	1.2252	0.00309	−0.00846
29X-3, 60–60	264.40	14	1.1832	0.00524	−0.00209
29X-4, 60–60	265.90	150	1.2485	0.00826	0.00890
30X-1, 50–50	270.90	32	1.3201	0.00415	0.01277
30X-2, 50–50	272.40	3	1.5283	0.00621	−0.00018
31X-1, 25–25	280.35	32	1.4088	0.00392	−0.00020
32X-1, 50–50	290.20	3	1.1771	0.00305	−0.02153
32X-2, 50–50	291.70	14	1.5448	0.00602	0.02946
33X-1, 47–47	299.87	150	1.5575	0.00448	0.01175
33X-2, 94–94	301.84	32	1.2026	0.00293	−0.01585
33X-3, 90–90	303.30	3	1.3040	0.00802	0.00803
33X-4, 90–90	304.80	14	1.2662	0.00489	0.02500
33X-5, 50–50	305.90	150	1.2320	0.00744	−0.00721
34X-CC, 27–27	309.71	32	1.1803	0.00273	−0.02834
35X-2, 29–29	320.59	3	1.3787	0.00658	−0.00162
36X-1, 29–29	328.79	14	1.2810	0.00548	0.04207
36X-2, 29–29	330.29	150	1.4102	0.00465	0.01245
36X-5, 96–96	333.96	32	1.2611	0.00414	0.02963
36X-6, 46–46	336.46	3	1.3209	0.00819	−0.00591
37X-2, 33–33	340.03	14	1.4143	0.00493	0.02718
37X-4, 130–130	344.00	150	1.2112	0.00408	−0.00352
38X-1, 44–44	348.34	32	1.2142	0.00641	−0.00080
38X-2, 44–44	349.84	3	1.2427	0.00558	0.01212
38X-3, 44–44	351.34	14	1.2285	0.00775	0.02141
38X-4, 44–44	352.84	150	1.1946	0.00452	−0.01601

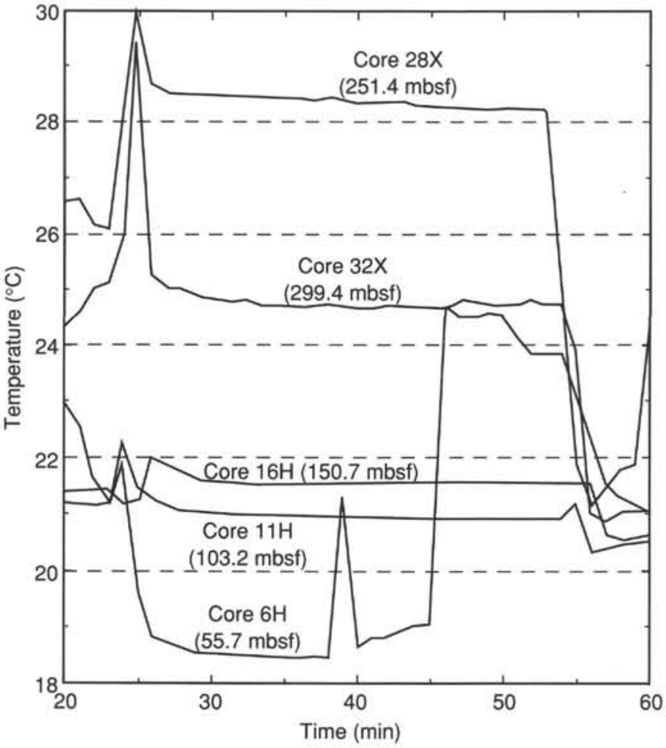

Figure 29. Temperature measured at the bottom of Hole 820A prior to recovering Cores 133-820B-6H, -11H, -16H, -28X, and -32X of Hole 820B. Horizontal axis is time after turning on temperature probe on deck before sending it down the hole. The sharp heat pulse at approximately 24 min for each deployment marks insertion of the temperature probe into sediments at the bottom of the hole. The sharp decrease in temperature at approximately 55 min marks withdrawal of the probe from the sediment for each deployment, except for Core 133-820B-6H, where withdrawal is marked by a sharp increase in temperature at 45 min. Depth (mbsf) is indicated after each core number.

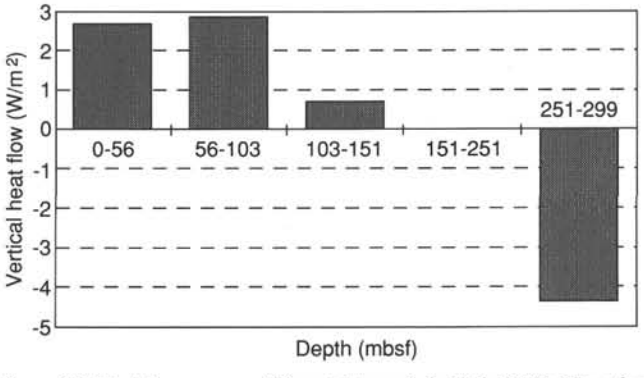

Figure 30. Heat flow across different intervals in Hole 820B. Negative flux of heat between 251 and 269 mbsf indicates that heat flow is downward, in contrast to the shallower measurements. This together with the small positive heat flow between 103 and 151 mbsf might indicate lateral advection of heat in the interval from 103 to 251 mbsf.

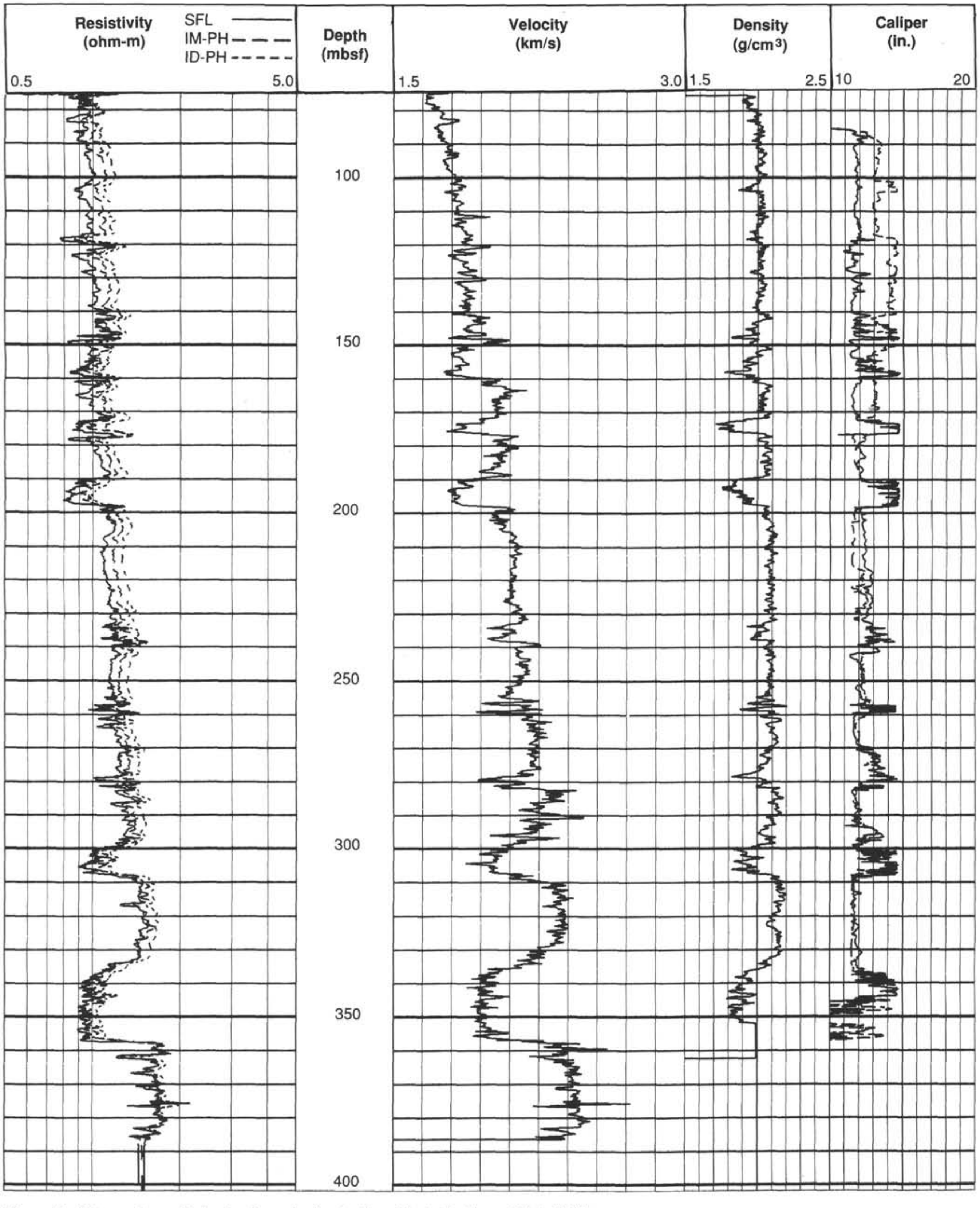

Figure 31. Primary logs obtained using seismic-stratigraphic tool string at Hole 820B.

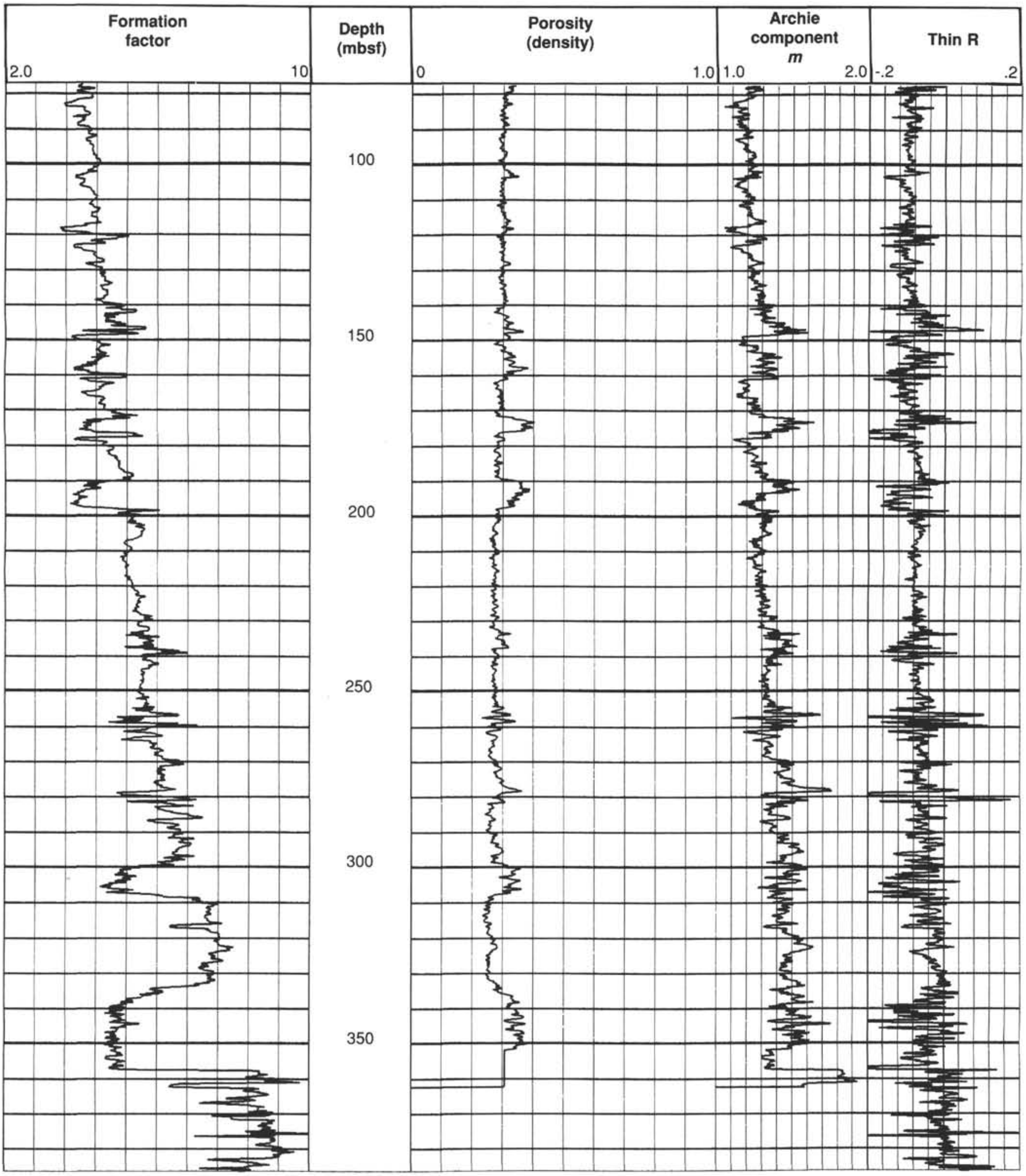

Figure 32. Site 820 logs of electrical resistivity formation factor (from ratio of formation resistivity to fluid resistivity), porosity (from neutron and density logs), the Archie component *m*, relating formation factor to porosity, and the parameter "Thin R," which responds to thin-bed effects.

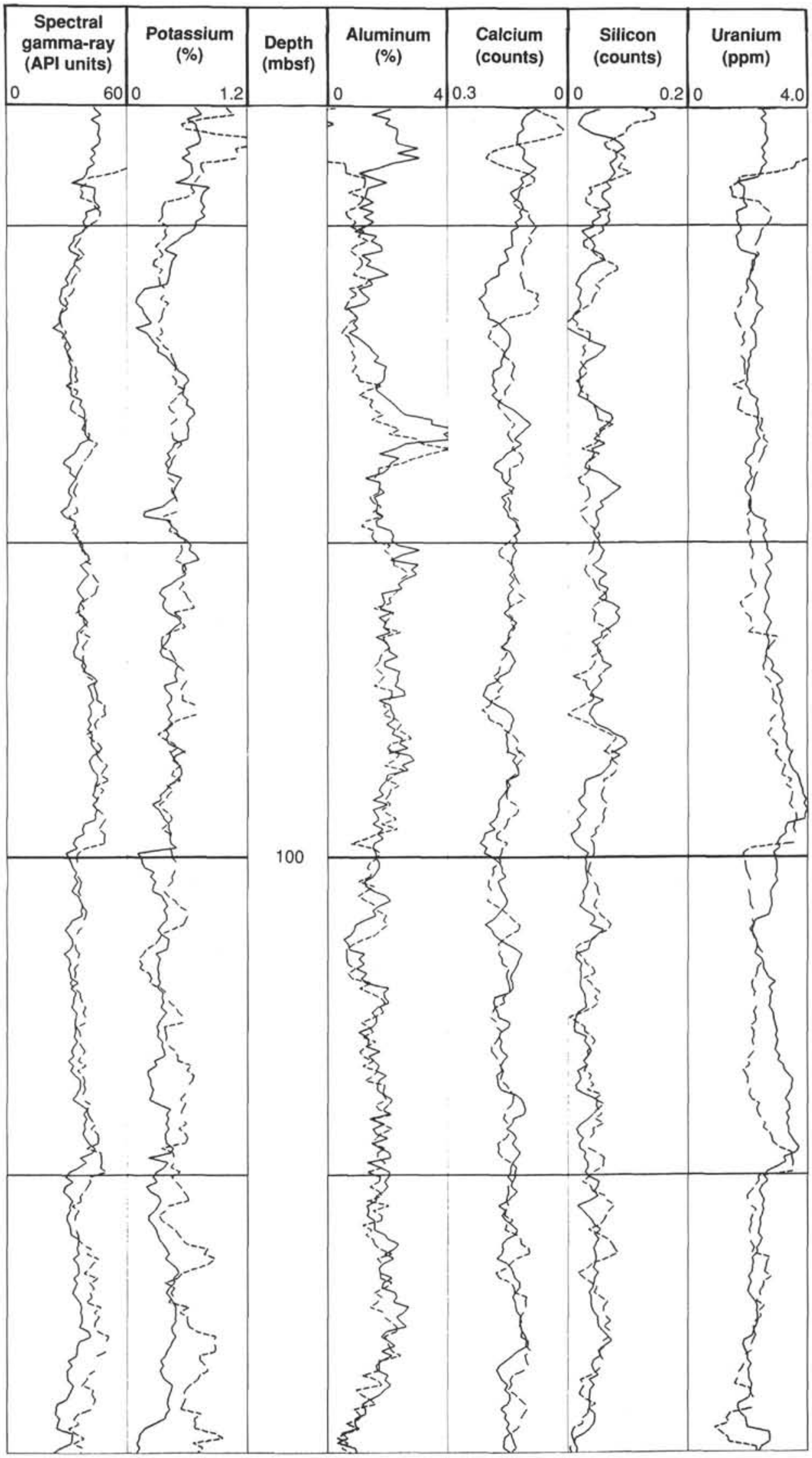

Figure 33. Geochemical logs for the interval from 76.1 to 118.7 mbsf at Site 820, showing the replicability of two logging passes over this interval.

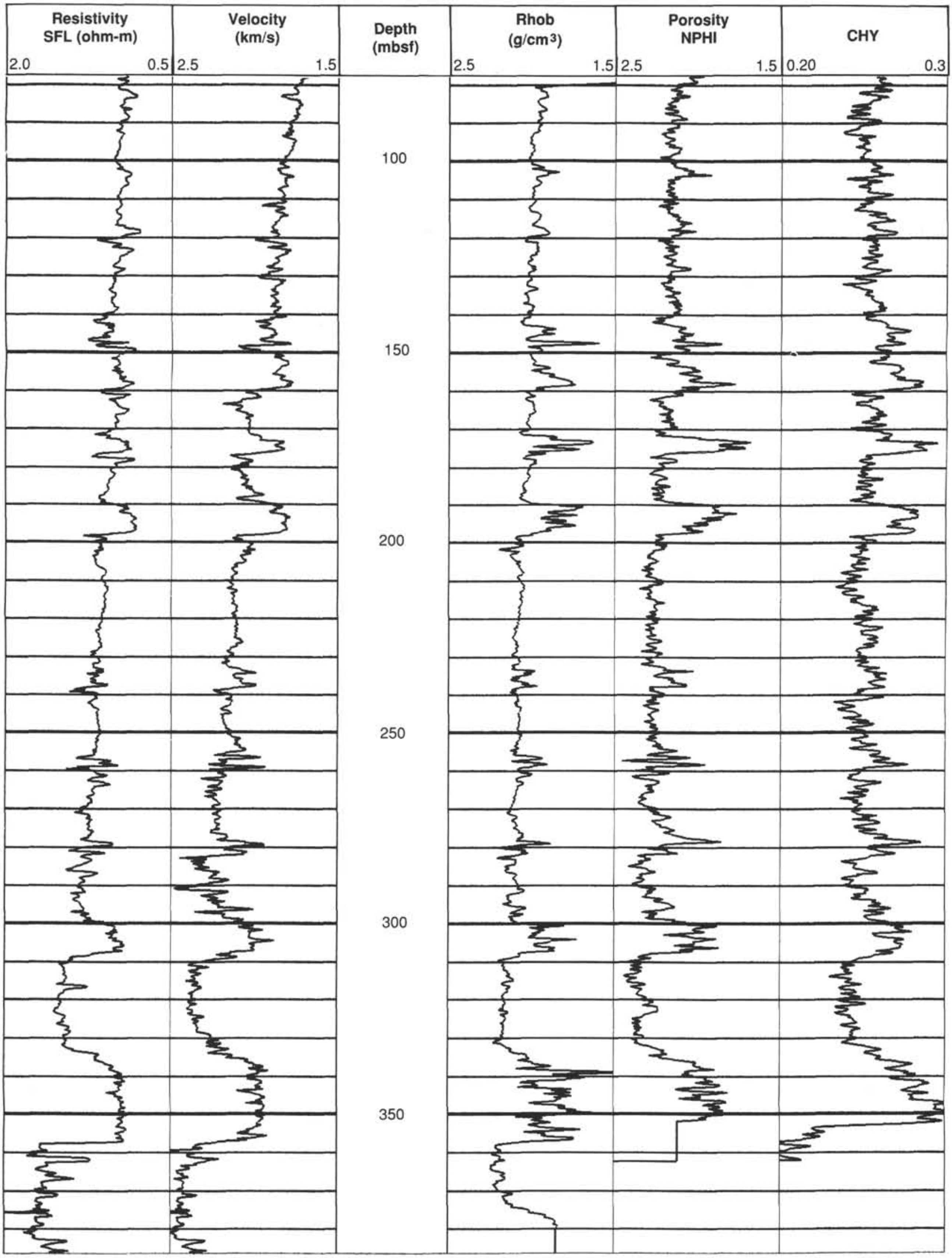

Figure 34. Porosity-sensitive logs for Site 820. Note the strong character match among these logs, indicating that all five logs are good indicators of variations in relative porosity.

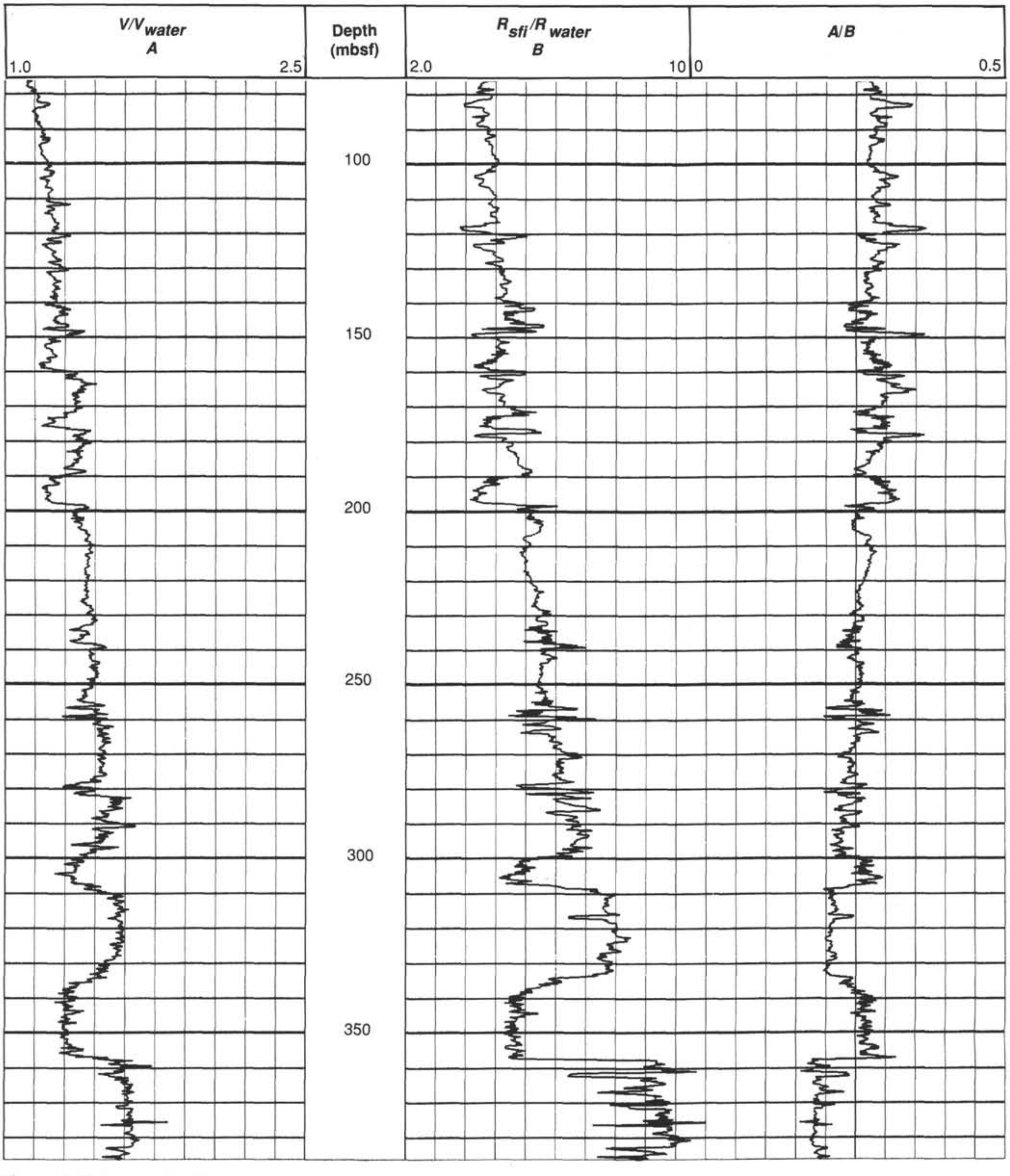

Figure 35. Velocity and resistivity logs for Site 820, plotted as ratios to each other and to water to highlight changes in pore geometry.

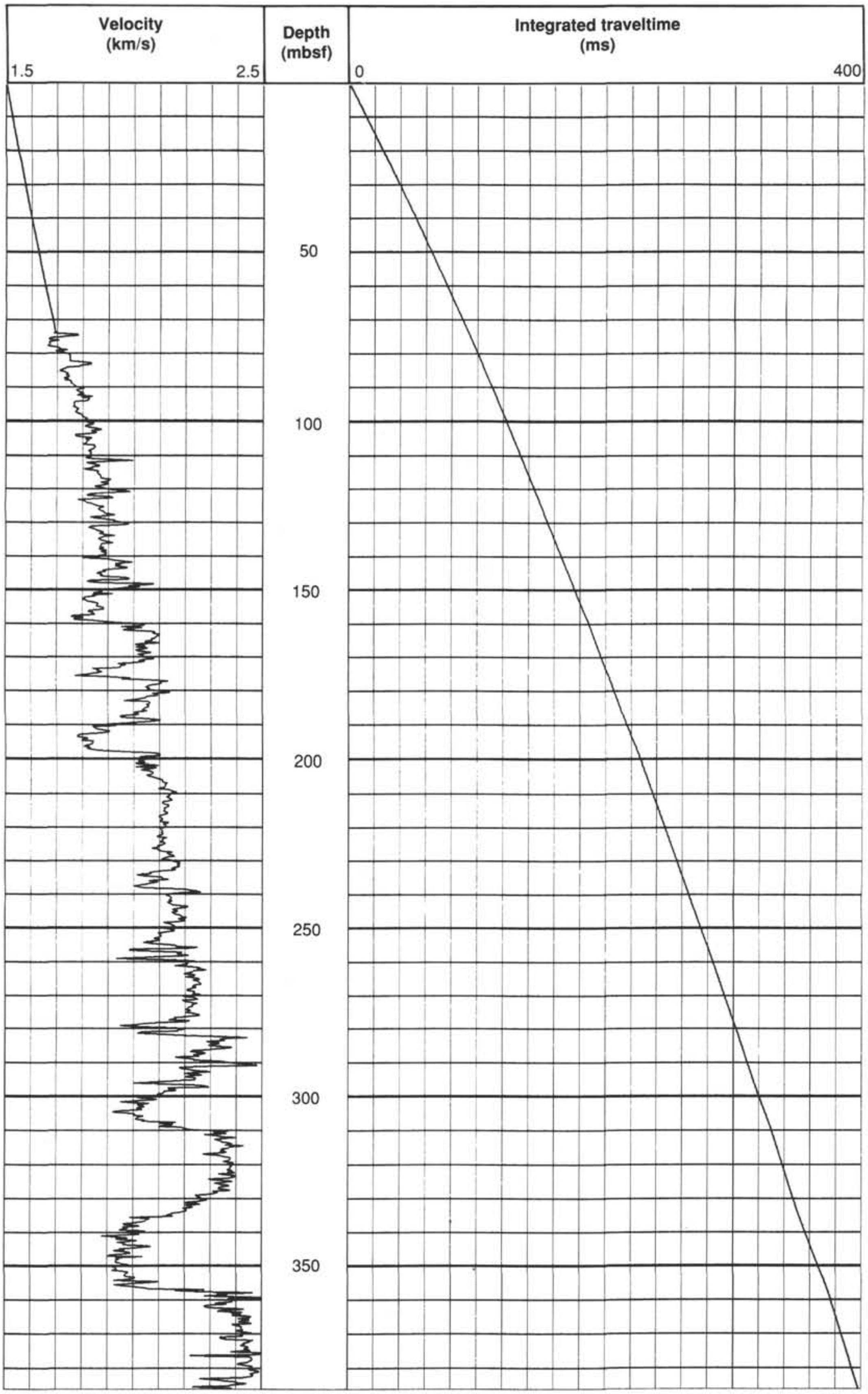

Figure 36. Velocity log, and the integrated two-way traveltime function that it implies, for matching core-based information from Site 820 with seismic sections across the site.

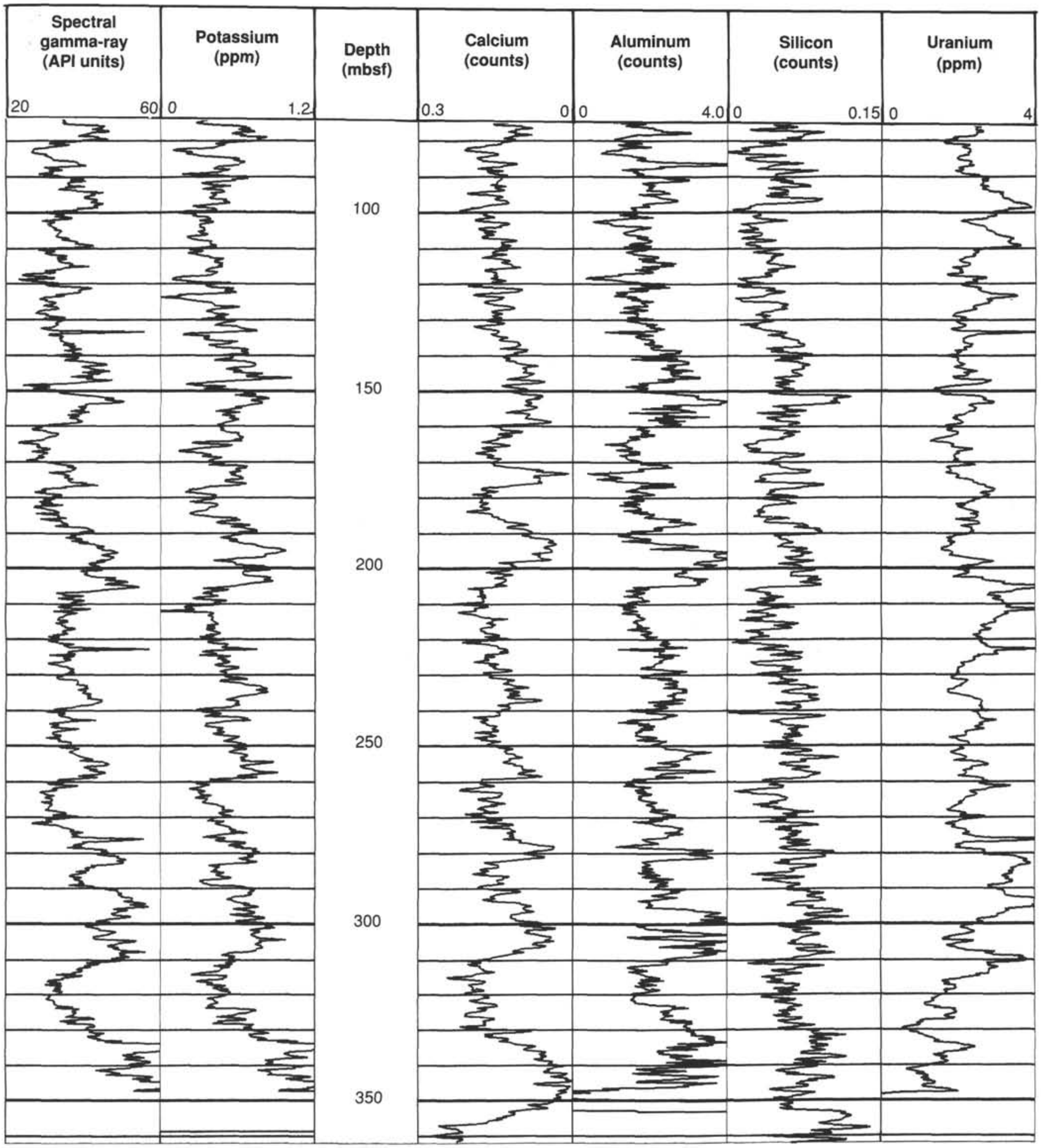

Figure 37. Geochemical logs from the portion of Site 820 where openhole logs were obtained. Note that elements abundant in clay minerals (potassium, aluminum, and silicon) correlate with each other, but are inversely correlated with calcium (predominantly in calcite).

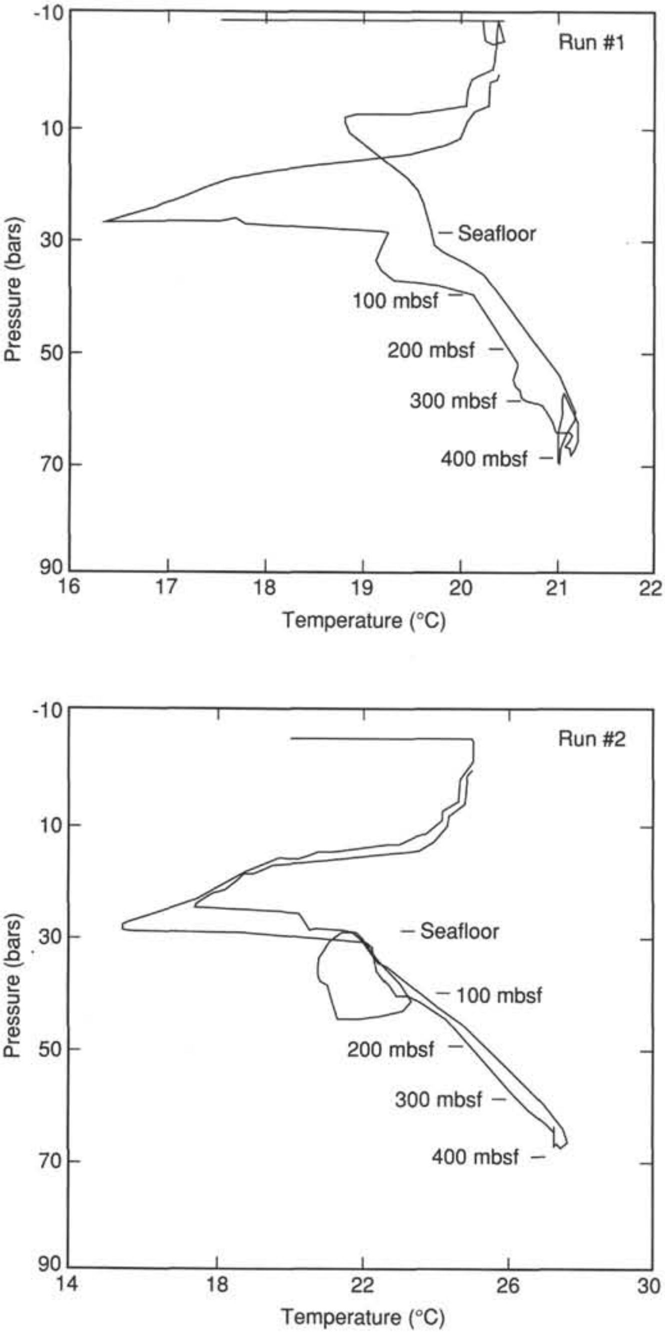

Figure 38. Temperature log as a function of pressure (or depth) for Site 820.

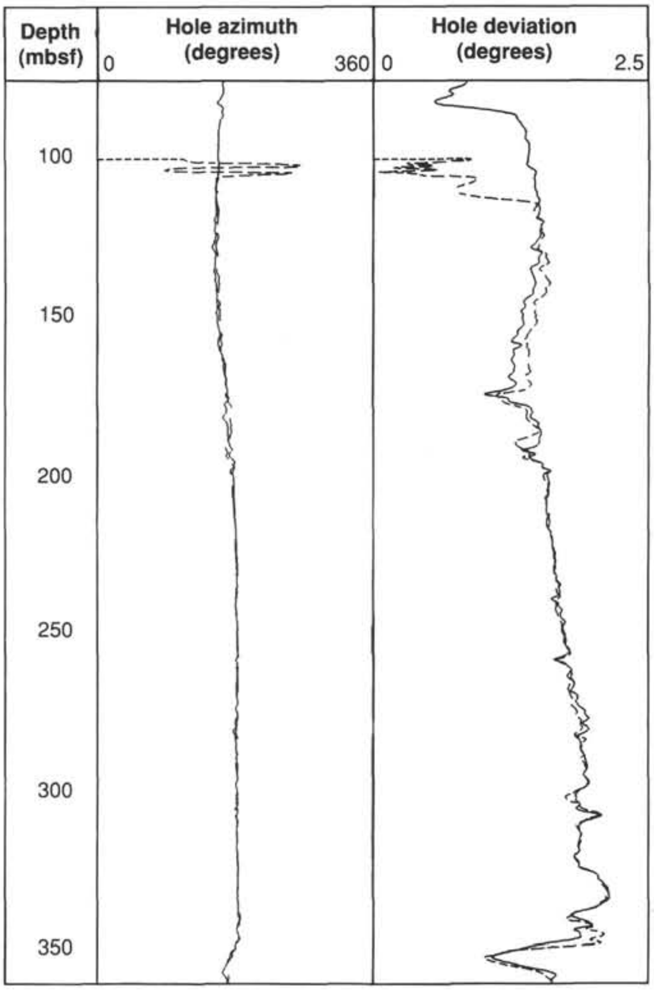

Figure 39. Hole deviation and its azimuth at Hole 820B. High variability at 100 to 115 mbsf in the logging run indicated by the dashed line is an artifact of proximity to pipe; pipe was 30 m shallower during the run indicated by the solid line.

Table 12. Check-shot survey at Hole 820B.

Depth (m below sea surface)	Measured time (ms)	Corrected time (ms)	No. shots (averaged)
373.4	238	239	5
391.7	246	247	5
416.1	260	261	5
446.5	278	280	5
461.8	283	284	5
480.1	292	294	5
492.3	300	302	7
507.5	306	308	3
528.8	319	320	7
544.1	323	325	5
565.4	332	333	5
592.8	346	348	7
614.2	355	356	5

Hole 820B: Resistivity-Sonic-Natural Gamma Ray Log Summary

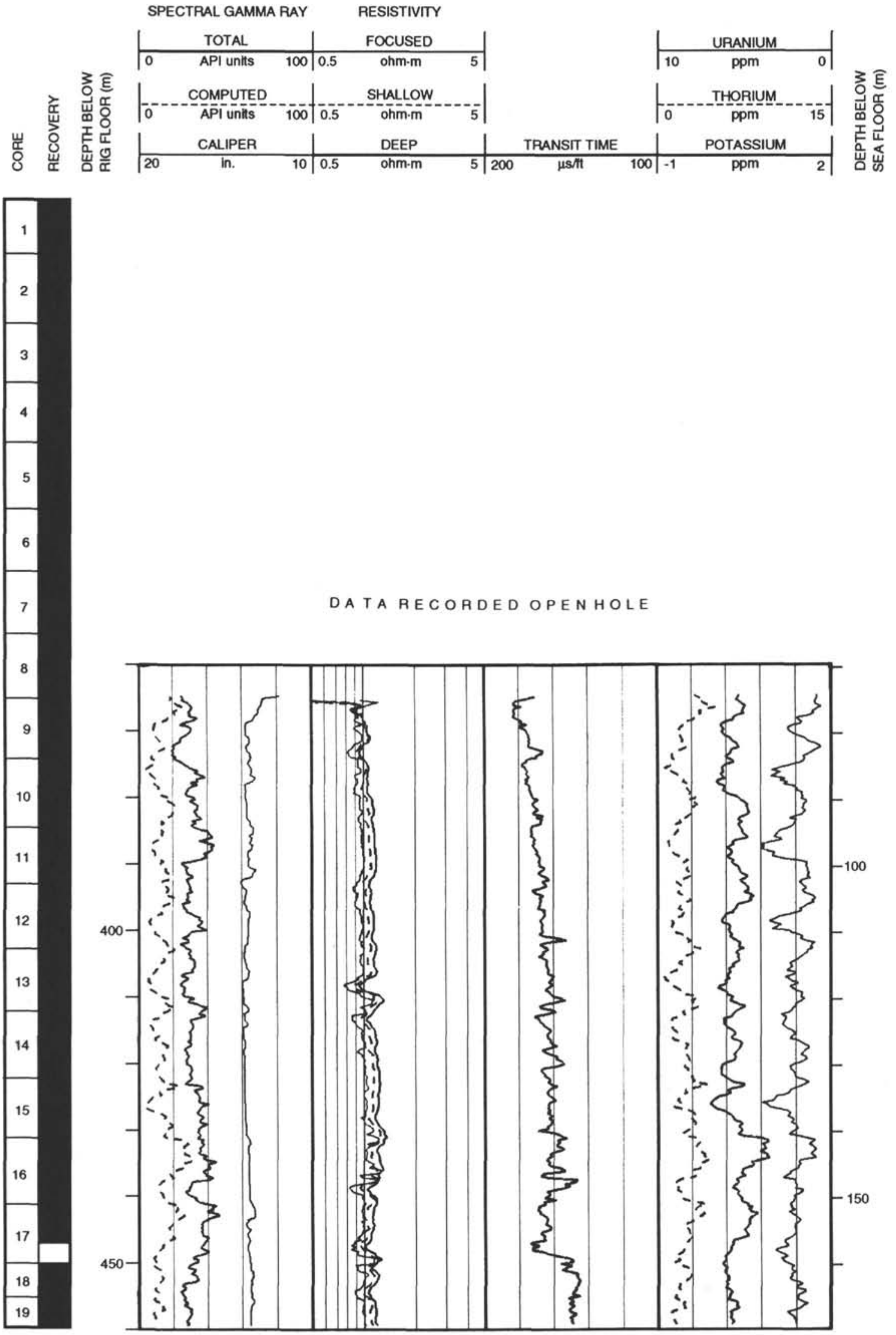

Hole 820B: Resistivity-Sonic-Natural Gamma Ray Log Summary (continued)

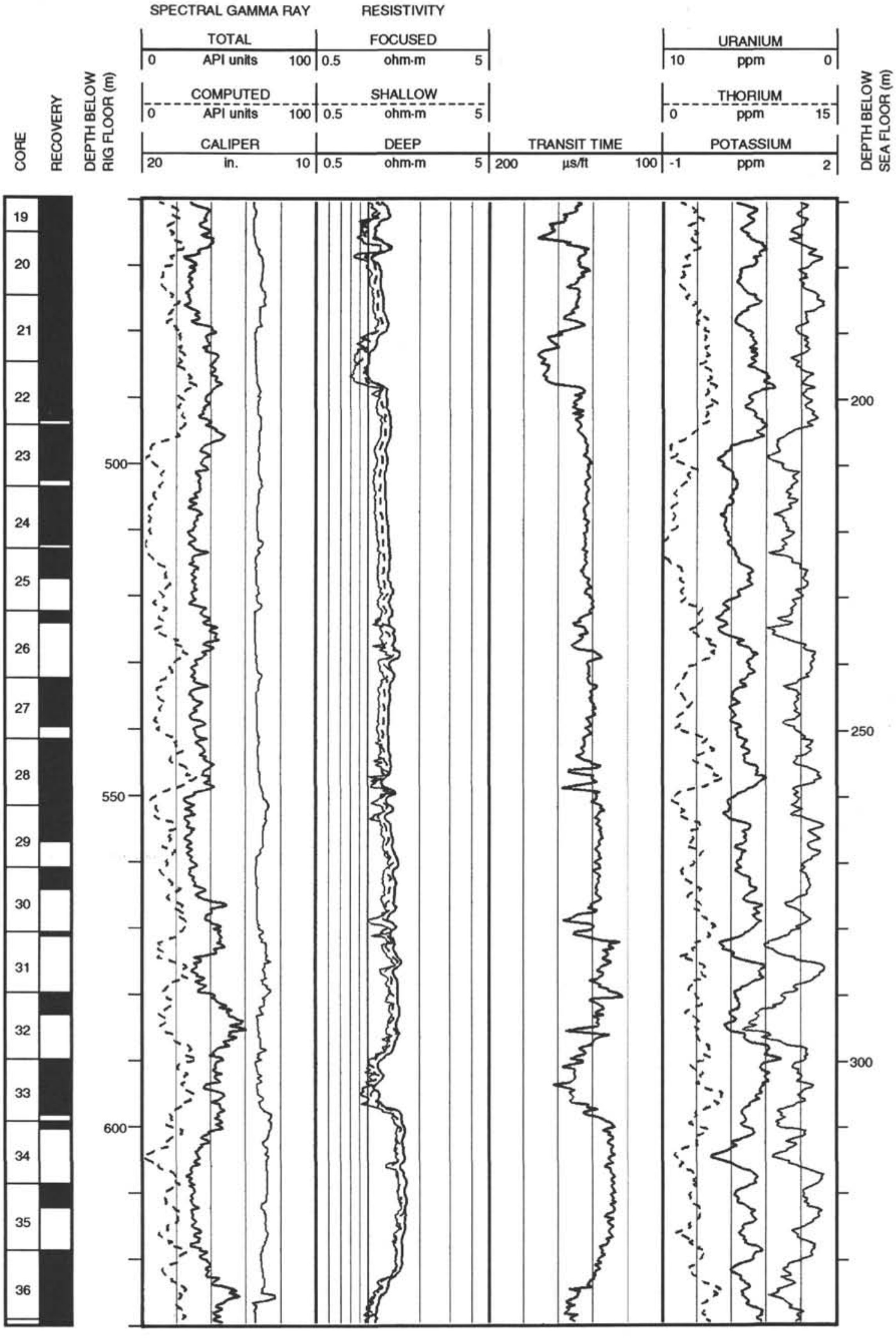

Hole 820B: Resistivity-Sonic-Natural Gamma Ray Log Summary (continued)

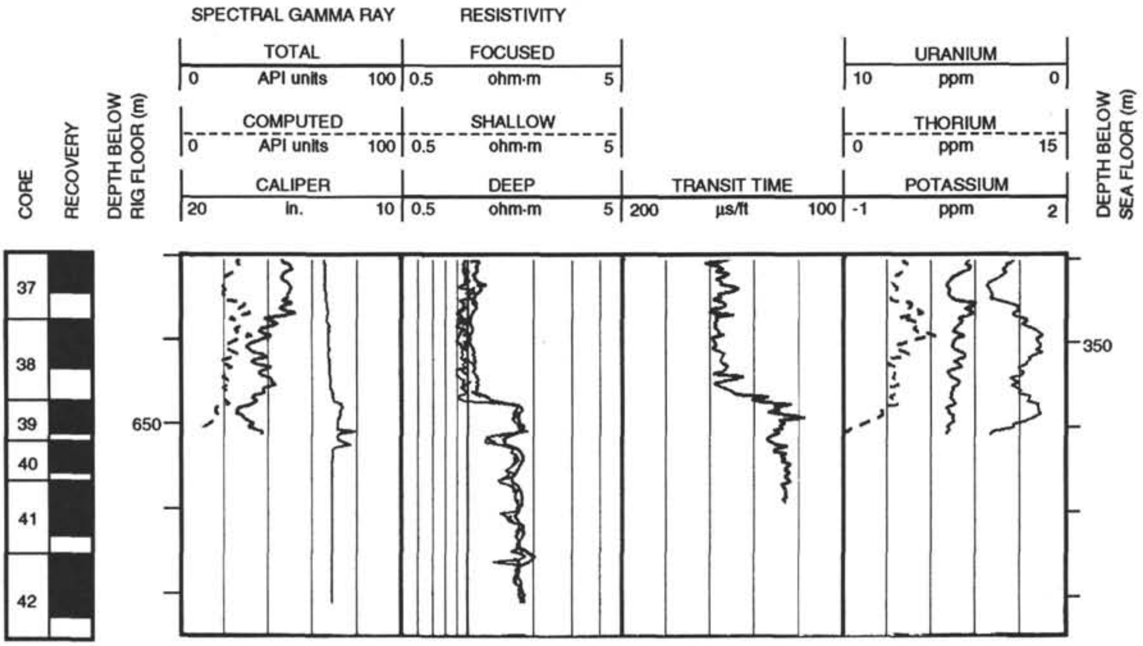

Hole 820B: Density-Natural Gamma Ray Log Summary

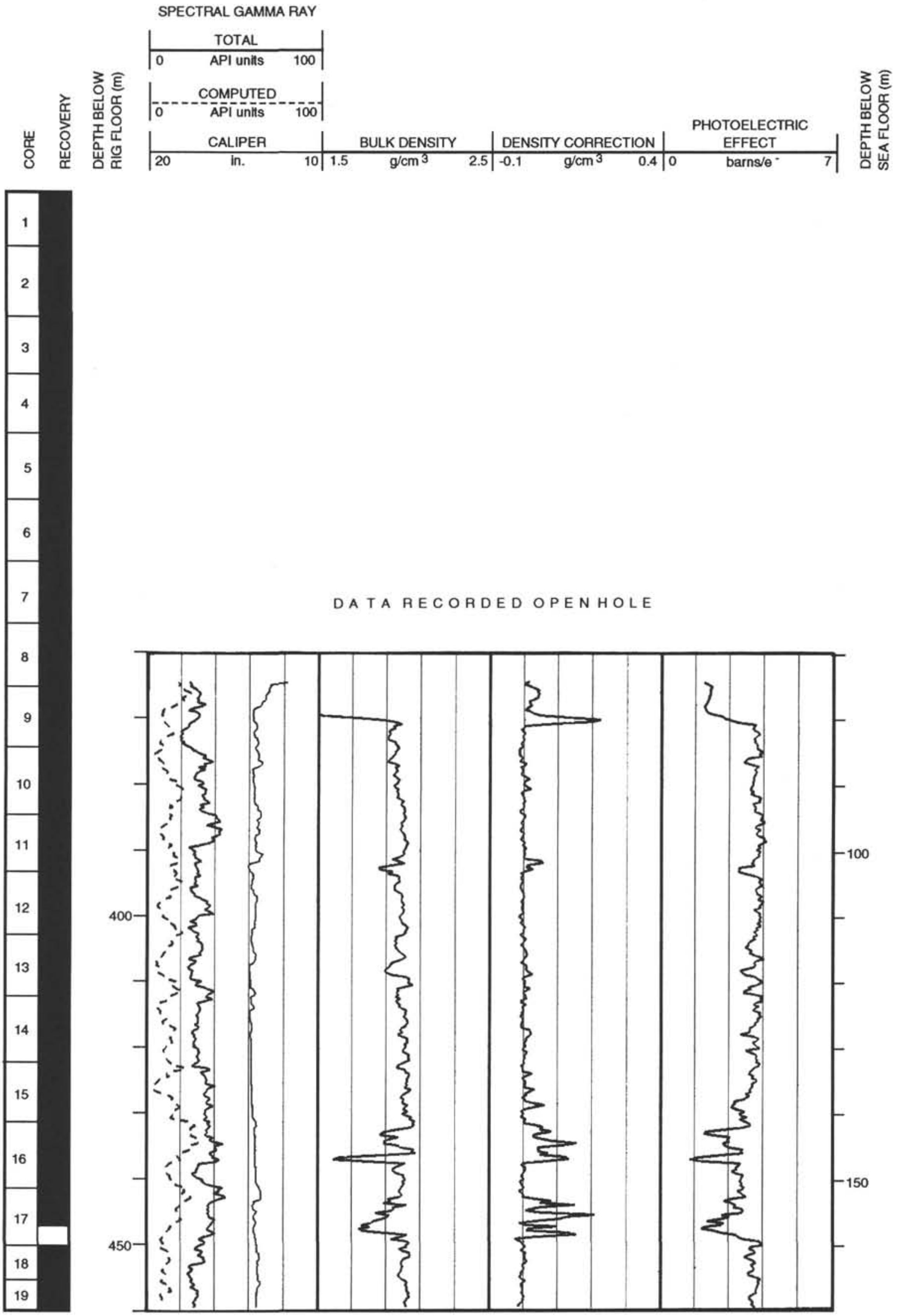

Hole 820B: Density-Natural Gamma Ray Log Summary (continued)

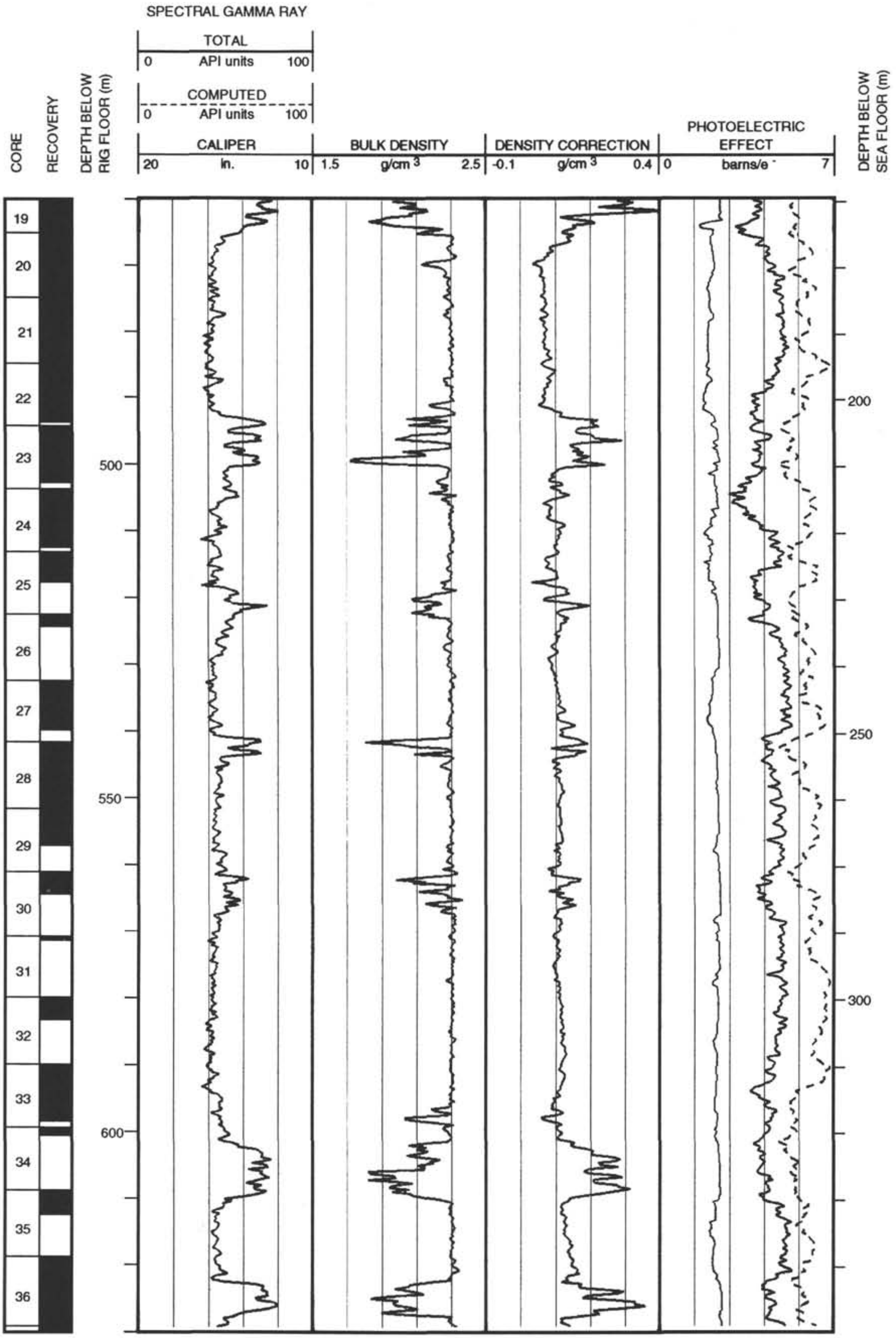

Hole 820B: Density-Natural Gamma Ray Log Summary (continued)

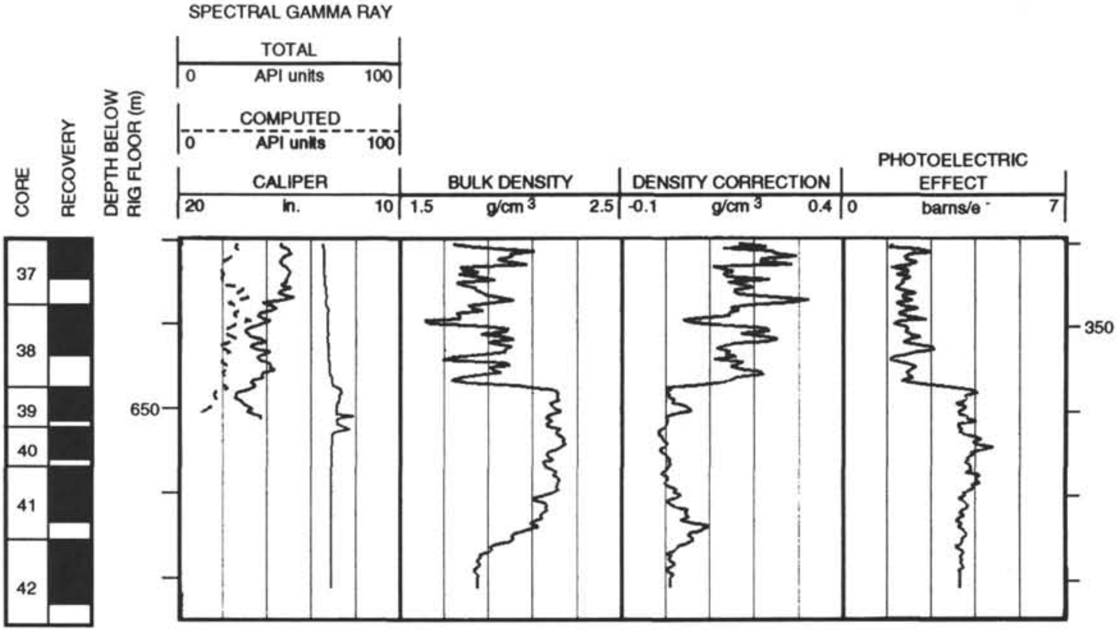

Hole 820B: Geochemical Log Summary

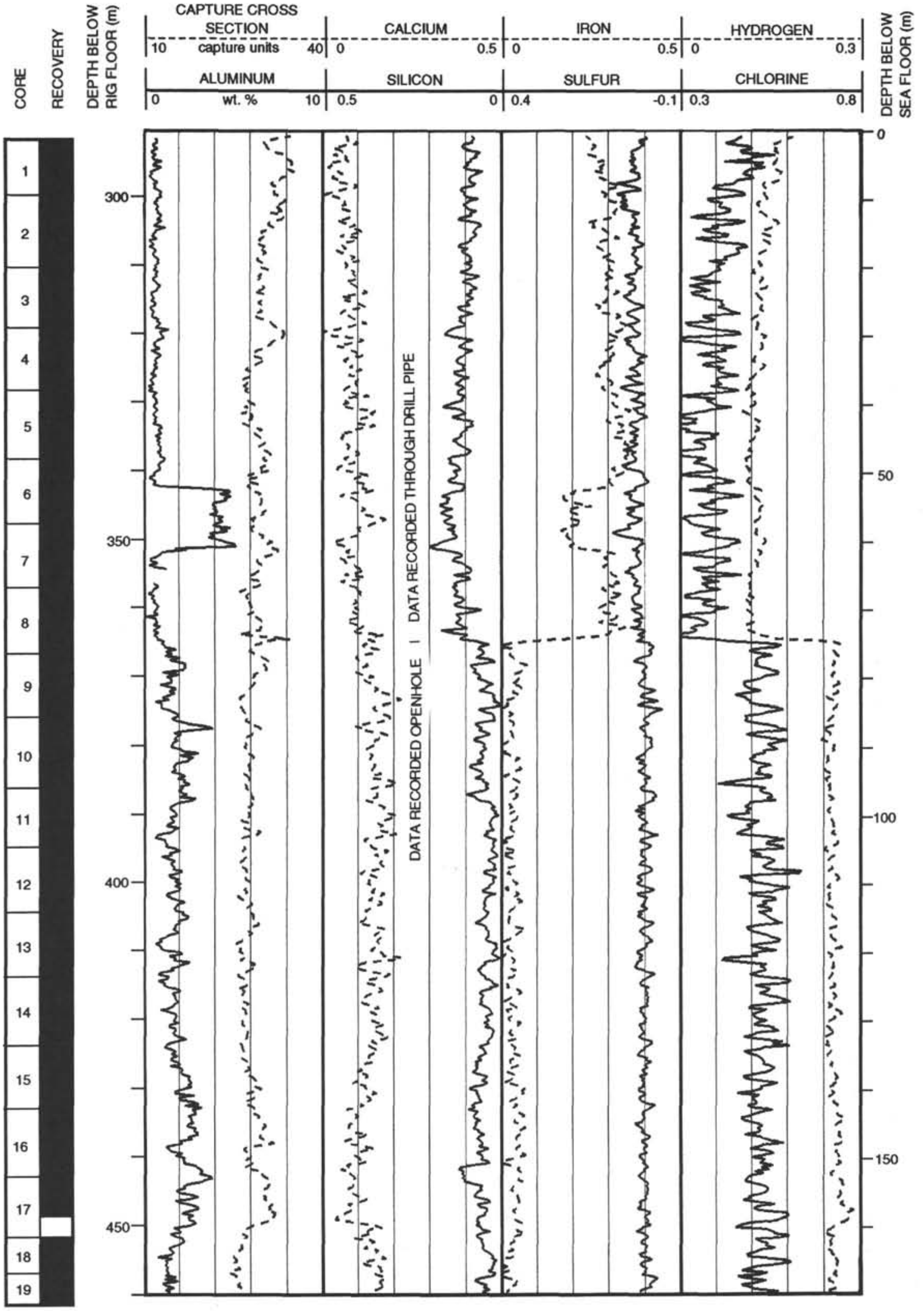

Hole 820B: Geochemical Log Summary (continued)

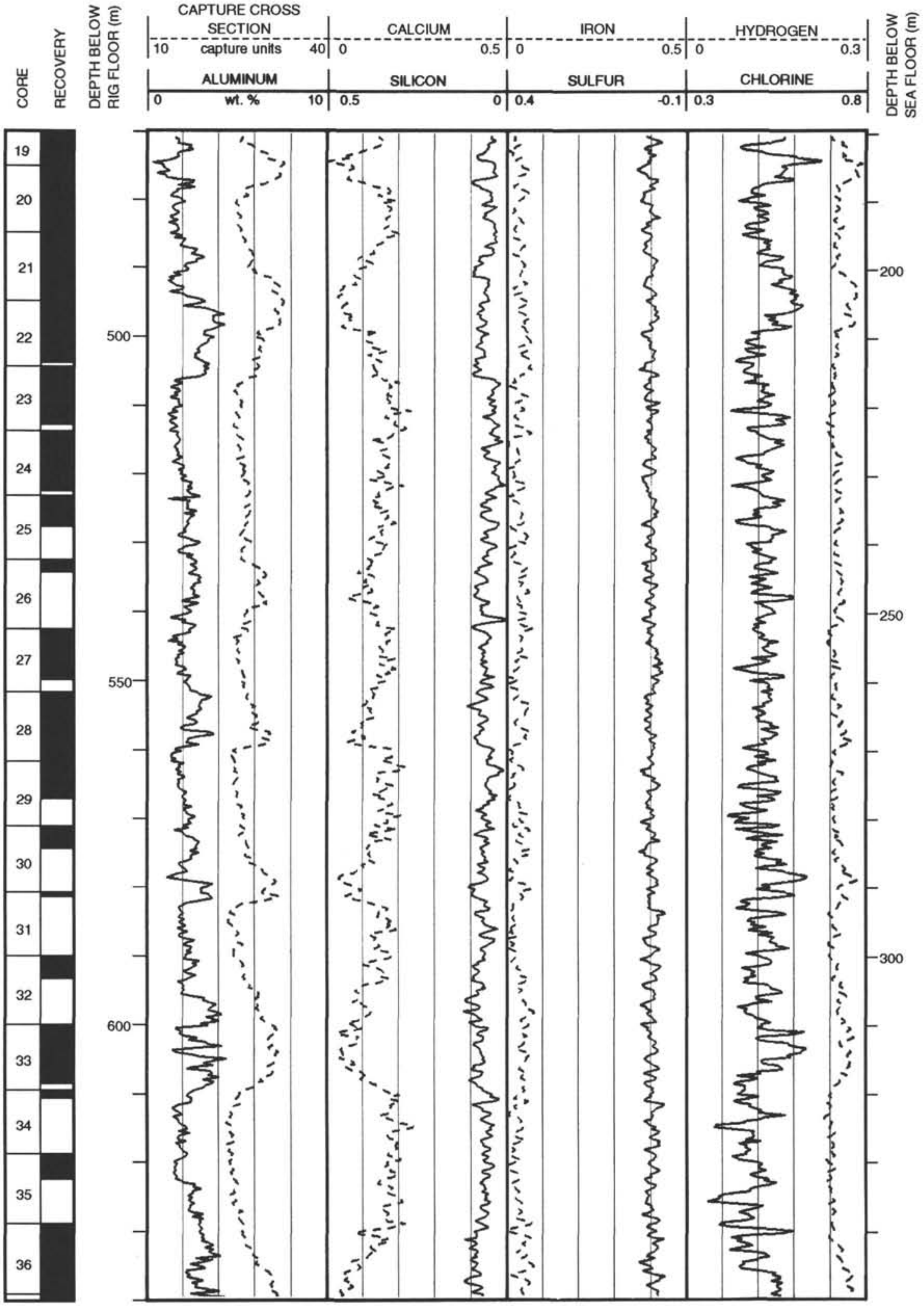

Hole 820B: Geochemical Log Summary (continued)